PROGRESS IN MEDICAL DEVICES

Editor-in-Chief: Haipo Cui

Volume 3, Number 1; Mar. 31, 2025

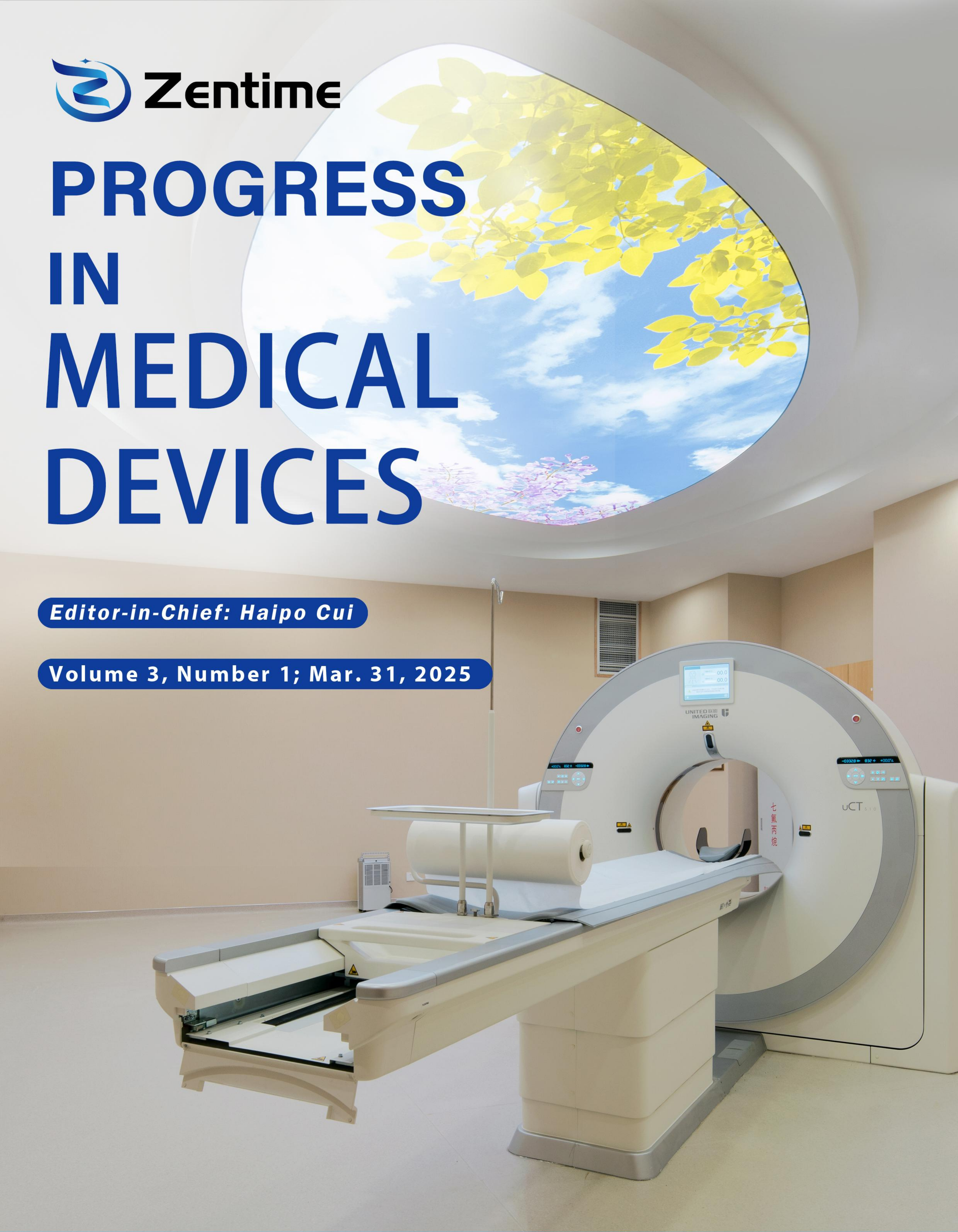

ISSN: 2957-5478

Published by ZENTIME PUBLISHING CORPORATION

Progress in Medical Devices
ISSN: 2957-5478

Zentime

Research Article https://doi.org/10.61189/621538dunoyl

Design and simulation of lower limb exoskeleton based on online gait generation algorithm

Jiaqing Wang[1], Renling Zou[1], Hongwei Tan[1], Jianchao Sun[1], Shi Gu[1], Xuezhi Yin[2]

[1]Department of Health Science and Engineering, University of Shanghai for Science and Technology, Shanghai 200082, China. [2]Shanghai Berry Electronic Technology Co., Ltd., Shanghai 200233, China.

Corresponding author: Renling Zou.

Acknowledgement: This work was supported by the Science and Technology Commission of Shanghai Municipality (21S31906000); the National Natural Science Foundation of China (61803265) and Medical-industrial cross-project of USST (1022308524).

Declaration of conflict of interest: None.

Received August 19, 2024; Accepted January 20, 2025; Published March 31, 2025

Highlights

- A novel lower limb exoskeleton was designed based on human biomechanics.
- The positive and inverse kinematic solutions of the exoskeleton were determined using the D-H method and geometric method, respectively.
- Geometrical relationships of the exoskeleton linkage members were utilized to derive workspace expressions for different gait stages.
- The efficacy of the online gait generation algorithm was assessed by providing initial conditions.
- Simulation experiments were conducted to analyse the dynamic self-balancing capabilities of the exoskeleton during flat walking.

Abstract

Objective: This study presents the design of an innovative lower limb exoskeleton featuring dynamic self-balancing capabilities. It employs Zero Moment Point and Model Predictive Control online gait algorithms to plan stable walking patterns, thereby facilitating precise gait training for individuals with lower limb motor impairments and enhancing the overall training effectiveness. **Methods:** The positive and negative kinematic solutions of the lower limb exoskeleton were determined using the Denavit-Hartenberg method and the geometric method, respectively. The geometric relationships of the exoskeleton's linkage components were employed to derive workspace expressions for various gait phases. By utilizing Zero Moment Point and Model Predictive Control online gait algorithms, simulation experiments were conducted to validate the dynamic self-balancing capability of the exoskeleton while walking on flat terrain. **Results:** In the evaluation of the online gait generation algorithm's validity, the generated gait trajectory aligned with the planned trajectory. When examining dynamic self-balancing walking capability, the trajectories from initial simulation experiments on flat terrain closely matched the intended trajectories. **Conclusion:** The online gait generation algorithm presented in this study is capable of producing a stable walking pattern for continuous bipedal gait. This newly designed lower limb exoskeleton can achieve stable dynamic self-balancing walking.

Keywords: Lower limb exoskeleton, online gait generation algorithm, dynamic self-balancing, rehabilitation training

Introduction

In recent years, the incidence of lower extremity motor disabilities has increased significantly. As per the 2023 National Spinal Cord Injury Statistical Centre report, there are around 302,000 Spinal Cord Injury patients in the United States, with approximately 180,000 new cases annually [1]. Among these patients, about 59.6% are tetraplegic and 39.9% are paraplegic. Clinical research indicates that scientific and rational exercise rehabilitation can help prevent and alleviate complications and long-term impacts of motor disabilities, enhancing limb function

Address correspondence to: Renling Zou, Department of Health Science and Engineering, University of Shanghai for Science and Technology, Shanghai 200082, China. E-mail: zourenling@163.com.

recovery [2]. Nevertheless, conventional manual gait rehabilitation heavily relies on the expertise of therapists, resulting in low efficiency and high labor costs [3]. To address the challenges associated with manual gait rehabilitation training, robotic gait rehabilitation, which offers repetitive and progressive training methods, are gaining more attention [4].

In recent decades, lower extremity exoskeletons have emerged as a widely utilized mechanism in gait rehabilitation. The Japanese Hybrid Assistive Limb exoskeleton system is specifically designed to aid elderly individuals with lower limb impairments or patients with lower limb paralysis [5]. This system enables extension/flexion movements at the hip, knee, and ankle joints, facilitating activities such as walking, standing, and stair climbing. Alongside Hybrid Assistive Limb, there has been a rise in underdriven exoskeletons, such as the Hank exoskeleton, which features rotary motors powering all six active joints with equal power distribution [6]. Other examples include the Chinese Fourier X2 and BEAR-H1 exoskeletons, which share a similar design but with varying drive power among joints [7, 8]. Hip-knee-ankle exoskeletons, like the Ekso, ReWalk, and ExoAtlet models, typically consist of four active joints in hip and knee flexion/extension directions, along with two passive joints in ankle flexion/extension directions, each driven by a motor and reducer [9-11]. For further simplicity, the Indego exoskeleton features only 4 active joints in the hip and knee flexion/extension directions, excluding ankle and foot devices [12]. In contrast, the H-MEX exoskeleton is equipped with 6 active joints in the hip and knee flexion/extension directions as well as hip adduction/abduction directions, along with 4 passive degrees of freedom in the ankle configuration [13, 14]. Knee-ankle exoskeletons, although less common, are typically designed to enhance human knee and ankle flexion/extension movements. Chen et al. developed a knee-ankle exoskeleton with 2 active degrees of freedom, utilizing linear elastic actuators to actuate both joints [15]. Similarly, Sawicki et al. designed a knee-ankle exoskeleton with 2 active degrees of freedom, powered by artificial pneumatic muscles [16].

The aforementioned underdriven lower limb exoskeleton primarily provides actuation in the flexion and extension degrees of freedom for the hip and knee joints. This actuation configuration enables the exoskeleton robot to assist the human body in performing intra-sagittal plane activities, thereby accommodating most daily tasks. However, due to a limited number of active degrees of freedom, the robot remains in an underdriven state, which precludes the realization of self-balancing capabilities. Consequently, it necessitates the use of external support devices, such as crutches, to maintain the balance and stability of the human-machine system. Therefore, the development of a self-balancing lower limb exoskeleton is crucial for ensuring the stability of rehabilitation gait training.

Self-balancing gait generation algorithms are primarily categorized into two types: offline gait generation algorithms and online gait generation algorithms [17-19]. Historically, robotic systems have relied on offline gait generation algorithms due to their limited capabilities in sensor information acquisition. These systems lack real-time feedback, are heavily dependent on the accuracy of the system model, and necessitate significant computational time. However, with advancements in information acquisition technology, online gait generation algorithms have emerged as the dominant approach in contemporary practical applications. This algorithm dynamically adapts to the environment and adjusts the robot's posture using real-time sensor data to maintain balance and stability. As a specific implementation method, the online gait algorithm employs state feedback control and incremental adjustments to accurately manage the gait, dividing the gait cycle into support phase and the swing phase. It dynamically modifies gait parameters during different phases to respond effectively to external disturbances. Additionally, the intermediate values of the gait trajectory are generated using linear interpolation methods to enhance the smoothness and stability of the gait, thereby achieving self-balancing. The online gait algorithm offers high adaptability with low computational overhead, making it particularly suitable for systems operating in diverse environments with limited hardware resources. Consequently, we propose the development of a self-balancing lower limb exoskeleton (Auto Balance Wang, ABW) based on the online gait algorithm.

Methods and equipment

Lower limb exoskeleton

To investigate the exoskeleton's anthropomorphic design, a comprehensive analysis was conducted utilizing principles of human anatomy and statistical data. Human movement, as outlined in human anatomy, can be categorized into three planes: sagittal, frontal, and horizontal, delineated by the sagittal, coronal, and vertical axes, respectively [20]. This division is illustrated in **Figure 1A**. The human hip func-

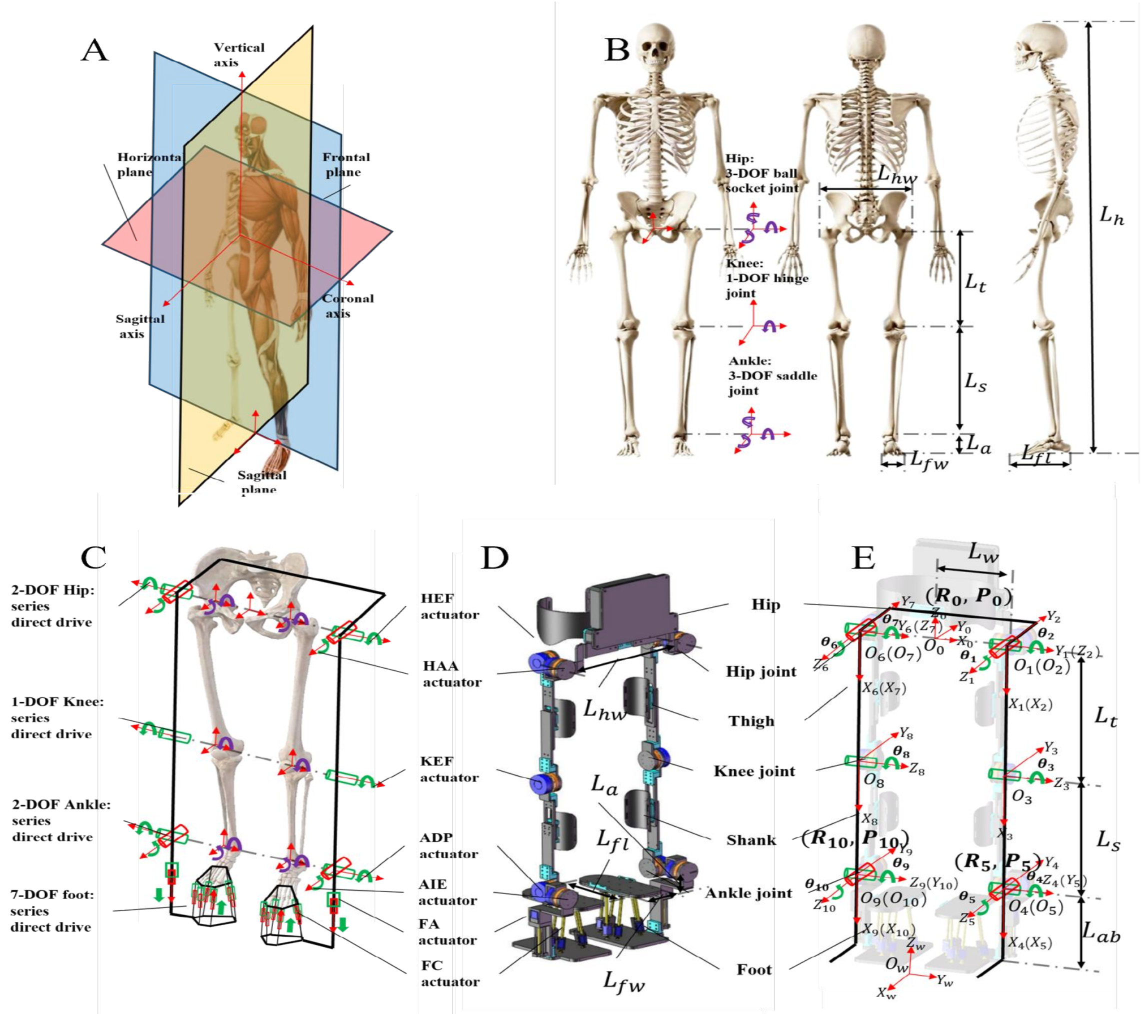

Figure 1. Design and analysis of lower limb exoskeleton. (A) Motion planes and basic axes; (B) Key dimensions; (C) Overall mechanism configuration; (D) Overall mechanical structure; (E) Kinematic model of the exoskeleton leg mechanism. DOF, degree of freedom; HEF, Hip extension/flexion; KEF, Knee extension/flexion; ADP, Ankle dorsiflexion/plantarflexion; AIE, Ankle extension/flexion; FA, Foot adaptation; FC, Foot regulation.

tions as a 3-degree of freedom (DOF) ball-and-socket joint, enabling hip adduction/abduction, hip flexion/extension, and hip endo-rotation/exo-rotation, as depicted in **Figure 1B**. Conversely, the human knee operates as a 1-DOF hinge joint facilitating knee flexion/extension. Likewise, the human ankle acts as a 3-DOF saddle joint, allowing ankle inversion/eversion, ankle dorsiflexion/plantarflexion, and ankle endo-rotation/exo-rotation. The body dimensions, as shown in **Figure 1B**, adhere to the Chinese standard 'GB/T 10000-1988 Chinese adult human body dimensions' for both male and female users [21]. The initial parameters are based on a male wearer with a height of 1.75 meters, as detailed in **Table 1**.

Gao et al. proposed that the range of movement (ROM) of each joint in an exoskeleton should be slightly less than the ROM of the corresponding human joint [22]. This precautionary measure aims to prioritize the safety of the human body within the exoskeleton's operational range, as illustrated in **Table 2**.

In this study, the ABW overall mechanism is illustrated in **Figure 1C**. The ABW features a left-right symmetrical series-parallel mechanism configuration. Each leg of the ABW possesses 12 active DOFs, comprising 2 at the hip, 1 at the knee, 2 at the ankle, and 7 at the foot. The foot mechanism employs a simplified 7-DOF parallel direct-drive mechanism to accurately simulate flat ground, stairway terrain, and sloping terrain, while also mimicking the posture and positional changes of the foot during multi-movement rehabilitation training to maintain a constant ankle height. The mechanism configurations are interconnected through series direct-drive connections, which eliminate the necessity for additional passive joints for motion transfer. However, since neither the hip nor the ankle joints allow for rotation around the vertical axis, the ABW can only facilitate unidirectional motion and cannot turn. These characteristics not only contribute to a com-

Table 1. Parameters of Chineses adult body and key ABW dimensions

Type	Body height L_h/mm	Thigh length L_t/mm	Shank length L_s/mm	Ankle height L_a/mm	Hip width L_{hw}/mm	Foot length L_{fl}/mm	Foot width L_{fw}/mm
Male	1528~1860	403~537	320~434	73~79	291~382	224~278	85~110
Female	1440~1725	375~508	297~401	66~69	281~375	208~256	77~102
ABW	N/A	375~540	295~435	75	280~385	270	110

Note: ABW, Auto Balance Wang.

Table 2. ROM joints of the human lower limb and the ABW

Joint	DOF	Human physiological limits/ °	ABW moveable range/ °
Hip joint	Flexion (-)/Extension (+)	-25~+125	-30~+120
	Adduction (-)/Abduction (+)	-30~+60	-30~+35
Knee joint	Flexion (-)/Extension (+)	0~+130	0~+95
Ankle joint	Plantarflexion (-)/Dorsiflexion (+)	-50~+30	-50~+45
	Eversion (-)/Inversion (+)	-35~+15	-35~+20

Note: ROM, range of movement; ABW, Auto Balance Wang; DOF, degree of freedom.

pact design but also ensure the self-balancing capability of human lower limbs on flat terrain. Based on **Figure 1C**, a prototype ABW mechanical structure was developed, as depicted in **Figure 1D**. This prototype operates in parallel with the human lower limbs, providing full support for the human body without the use of crutches.

Among the 24 actuators, the hip adduction/abduction and ankle inversion/eversion actuators are positioned behind the hip flexion/extension and ankle dorsiflexion/plantarflexion actuators, respectively, to prevent structural interference. The hip flexion/extension and knee flexion/extension actuators offer a wide range of motion for the sit-to-stand process. Additionally, the foot adaptation and regulation actuators are interconnected for multi-terrain simulation. With the assistance of the ABW, patients can engage in various rehabilitation exercises, including walking on level ground, climbing stairs, and ascending slopes, all without the need for crutches or other external support devices.

Kinematic analysis

This study investigates the performance of the exoskeleton in ambulating on flat terrain. The kinematic model of the ABW robot's leg mechanism (**Figure 1E**) was developed using a seven-link framework that incorporates the hip, knee, and ankle joint mechanisms. The designations used are as follows: O_w denotes the world coordinate system, O_0 signifies the base coordinate system located at the waist center, and O_i (where i = 1, 2, ..., 6) designates the base coordinate system situated at the centers of the moving joints.

The kinematic model is segmented into two symmetric branches, the left leg branch and the right leg branch, enabling the solution of kinematics as a non-redundant problem. Therefore, the Denavit-Hartenberg (D-H) method is utilised to obtain a positive kinematic model for each branch as follows.

$$ {}^{0}_{5}\mathbf{T} = {}^{0}_{1}\mathbf{T}(\theta_1){}^{1}_{2}\mathbf{T}(\theta_2){}^{2}_{3}\mathbf{T}(\theta_3){}^{3}_{4}\mathbf{T}(\theta_4){}^{4}_{5}\mathbf{T}(\theta_5) \tag{1} $$

$$ {}^{6}_{10}\mathbf{T} = {}^{0}_{6}\mathbf{T}(\theta_6){}^{6}_{7}\mathbf{T}(\theta_7){}^{7}_{8}\mathbf{T}(\theta_8){}^{8}_{9}\mathbf{T}(\theta_9){}^{9}_{10}\mathbf{T}(\theta_{10}) \tag{2} $$

Based on the D-H method, the transformation matrix ${}^{i-1}_{i}\mathbf{T}$ between two consecutive coordinates can be expressed as Eq. (3) [23]:

$$ {}^{i-1}_{i}\mathbf{T} = \begin{bmatrix} cos\theta_i & -sin\theta_i & 0 & a_{i-1} \\ sin\theta_i cos\alpha_{i-1} & cos\theta_i cos\alpha_{i-1} & -sin\alpha_{i-1} & -sin\alpha_{i-1} d_i \\ sin\theta_i sin\alpha_{i-1} & cos\theta_i sin\alpha_{i-1} & cos\alpha_{i-1} & sin\alpha_{i-1} d_i \\ 0 & 0 & 0 & 1 \end{bmatrix} \tag{3} $$

where θ_i is the rotational angle of the i-th moving joint, a_{i-1} is the link length, α_{i-1} is the link twist, d_i is the link offset.

Conversely, we can use geometric analysis to obtain an inverse kinematic model for both branches as follows:

$$ \begin{cases} (\theta_1, \theta_2, \theta_3, \theta_4, \theta_5) = f_5(\mathbf{R}_5, \mathbf{P}_5, \mathbf{R}_0, \mathbf{P}_0) \\ (\theta_6, \theta_7, \theta_8, \theta_9, \theta_{10}) = f_5(\mathbf{R}_{10}, \mathbf{P}_{10}, \mathbf{R}_0, \mathbf{P}_0) \end{cases} \tag{4} $$

where $\mathbf{R}_5/\mathbf{R}_{10}/\mathbf{R}_0$ is the attitude matrix of the left foot/right foot/waist described in world coordination O_w, and $\mathbf{P}_5/\mathbf{P}_{10}/\mathbf{P}_0$ represents the corresponding position vector.

Workspace analysis

Lower limb exoskeletons exhibit a range of complex movement patterns, including parallel walking, walking up and down stairs, and walking up and down slopes, all of which necessi-

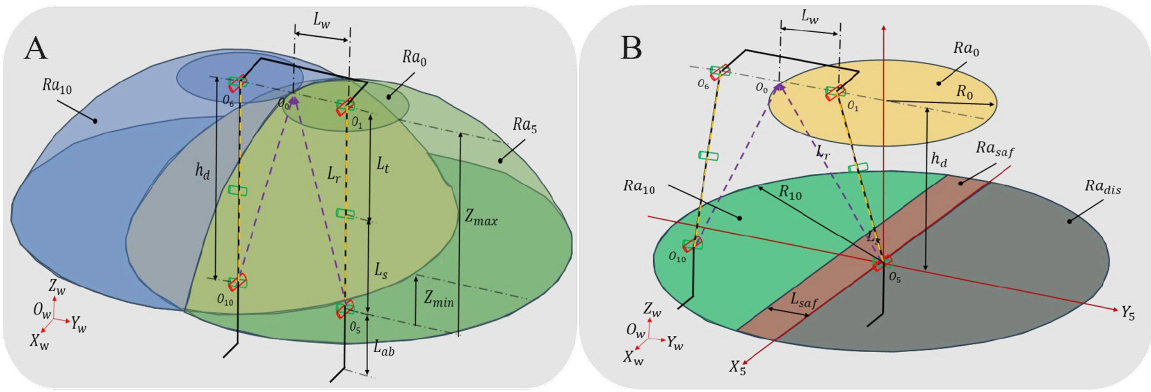

Figure 2. Workspace of the exoskeleton. (A) Workspace of the waist centre in the DFS phase; (B) Workspace of the waist centre and swing foot ankle centre in the SFS phase. DFS, dual-support phase; SFS, single-support phase.

tate a thorough analysis of their workspace. The bipedal locomotion gait cycle of the exoskeleton encompasses a single-support phase (SFS) and a dual-support phase (DFS). During the SFS phase, the supporting foot of the exoskeleton remains grounded while the swinging foot follows a predetermined path, with the lumbar centre moving in space. In the subsequent DFS phase, both feet are grounded as the waist centre moves along the planned trajectory. Given the varying features of the exoskeleton mechanism across different walking phases, we will proceed to analyse the corresponding workspace.

In the DFS phase, the exoskeleton is a closed-loop mechanism consisting of a two-part 5-DOF chain, as shown in **Figure 2A**. The object of analysis is the workspace of the waist centre O_0. It's assumed that the positions of the left foot centre O_5 and the right foot centre O_{10} in the world coordinates O_w are $\mathbf{P}_0=(x_0, y_0, z_0)^T$, $\mathbf{P}_5=(x_5, y_5, z_5)^T$ and $\mathbf{P}_{10}=(x_{10}, y_{10}, z_{10})^T$, respectively. In addition, to increase the wearing safety and comfort of the self-balancing exoskeleton, the posture of the waist and the feet are usually parallel to the ground. Then, the workspace O_0 can be obtained by geometric constraints as follows:

$$\begin{cases} Ra_5 = \left\{ (x_0, y_0, z_0) \middle| \begin{array}{l} (x_0 - x_{10})^2 + (y_0 - y_{10})^2 + (z_0 - z_{10})^2 \\ -2L_w\sqrt{L_{r1} - (z_0 - z_{10})^2} \le L_{r1}^2 + L_w^2, \\ Z_{\min} \le z_0 \le Z_{\max} \end{array} \right\} \\ Ra_{10} = \left\{ (x_0, y_0, z_0) \middle| \begin{array}{l} (x_0 - x_5)^2 + (y_0 - y_5)^2 + (z_0 - z_5)^2 \\ -2L_w\sqrt{L_{r1} - (z_0 - z_5)^2} \le L_{r1}^2 + L_w^2, \\ Z_{\min} \le z_0 \le Z_{\max} \end{array} \right\} \\ Ra_0 = \begin{cases} Ra_5 \cap Ra_{10} \\ \theta_i \in \left[\theta_{\min\_i}, \theta_{\max\_i}\right] (i = 1, 2, \cdots 10) \end{cases} \end{cases} \tag{5}$$

where the waist centre height z_0 is limited to$[Z_{min}, Z_{max}]$. When the position of z_0 in O_0 is given, θ_i can be calculated by the kinematic inverse model. The joint range θ_i is shown in **Table 2**.

In the SFS phase, the exoskeleton is an open-loop tandem mechanism with 10 joints. Since it is difficult to analyse the workspace of a tandem mechanism with high redundant DOF, it can be divided into two tandem branches, each containing 5 DOFs. As shown in **Figure 2B**, the left leg is set as support and the right leg as swing. At this stage, the object of analysis is the workspace of O_{10}. Since the trajectory of the exoskeleton is planned to walk on a flat terrain, the key is to obtain the reachable area of the swinging foot on the ground. Therefore, it does not make much sense to analyse the whole workspace of O_{10}, and we only considered analysing the ground workspace of O_{10}. Given the left foot centre O_5 position $\mathbf{P}_5=(x_5, y_5, z_5)^T$ in O_w, the waist and feet posture are also set parallel to the ground. The Ra_0 region in O_0 is restricted to a circle by the support leg. To avoid interference between the swing leg and the support leg, the Ra_{dis} region is discarded. A safety gap Ra_{saf} is also set to avoid the interference between left and right legs. Finally, considering the ROM of each joint, the working space of O_{10} can be obtained by the following equation:

$$Ra_{10} = \left\{ (x_{10}, y_{10}) \middle| \begin{array}{l} (x_{10} - x_5)^2 + (y_{10} - y_5)^2 \\ \le 4\left(\sqrt{L_r^2 - h_d^2} + L_w\right)^2 \\ x_{10} - x_5 \le -L_{\text{saf}} \\ \theta_i \in \left[\theta_{\min\_i}, \theta_{\max\_i}\right] (i = 1, 2, \cdots 10) \end{array} \right\} \tag{6}$$

Online gait generation algorithm

The online bipedal gait generation algorithm aims to develop a predictive controller for man-

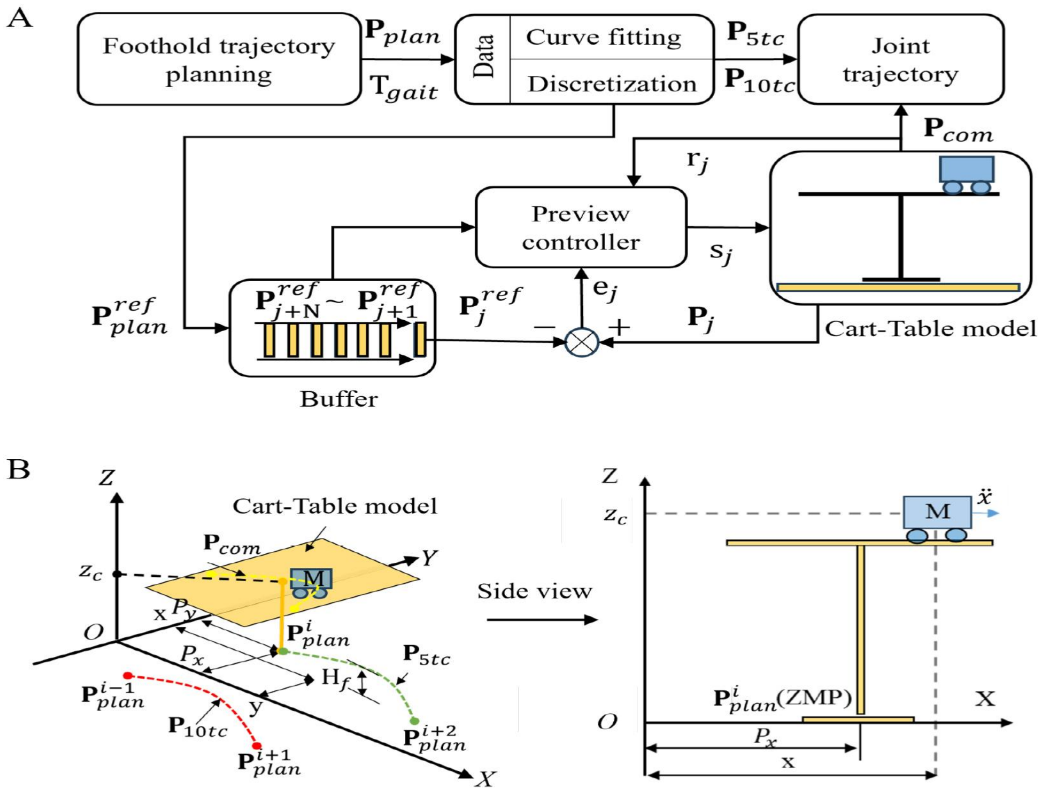

Figure 3. Online bipedal gait generation algorithm. (A) Gait trajectory planner algorithm framework; (B) Exoskeleton dynamics model based on 3D Car-Table. ZMP, zero moment point.

aging the motion of the centre of mass through the feedback function of the servo system, utilising information regarding the future target Zero Moment Point (ZMP). This approach facilitates the tracking of the target ZMP. In this study, the gait trajectory planner is employed as an online bipedal gait generation algorithm based on Model Predictive Control (MPC) and ZMP, which is responsible for generating the trajectories of the robot's centre of mass, as well as the left and right foot trajectories, ensuring that the stability requirements for bipedal walking are met. The block diagram of the algorithm can be seen in **Figure 3A**. The inputs to the algorithm include the sequence of landing points $\mathbf{P}_{plan}$ and the gait period $\mathbf{T}_{gait}$ of the path trajectory, which serve as the ZMP reference values for future gait cycles. The sampling period Δt is determined by the servo period of the control system. The final output of the gait trajectory planner includes the trajectory curve $\mathbf{P}_{com}$ for the exoskeleton robot's center of mass (COM), the left foot trajectory curve $\mathbf{P}_{5tc}$, and the right foot trajectory curve $\mathbf{P}_{10tc}$.

In the context of gait planning, this paper utilises a Car-Table based model to control the trajectory of the COM in accordance with balance requirements and to accurately track the planned landing point's trajectory. When the exoskeleton robot is standing on one leg at the i-th planned landing point $\mathbf{P}^{i}_{plan}$, denoted as the j-th ZMP reference position $\boldsymbol{P}_j^{ref}=(\boldsymbol{P}_{xj}^{ref}, \boldsymbol{P}_{yj}^{ref})$, its dynamic model can be simplified to a spatial 3D Car-Table model [24]. This model assumes that all the weight of the robot is concentrated at the centre of the car, as illustrated in **Figure 3B**. Considering the height of the robot's centre of mass as z_c, achieving walking balance necessitates that the COM position $\mathbf{P}_{comj}=(x_j, y_j)$ and the planned landing point (ZMP position) $\mathbf{P}_j=(\mathbf{P}_{xj}, \mathbf{P}_{yj})$ satisfy a specific equation.

$$\begin{cases} P_x = x - \dfrac{z_c}{g}\ddot{x} \\ P_y = y - \dfrac{z_c}{g}\ddot{y} \end{cases} \tag{7}$$

To achieve online gait trajectory planning, this paper adopts the COM trajectory planning algorithm based on MPC theory [25, 26]. For Eq. (7), a variable $\mathbf{s}=(s_x, s_y)$, is redefined, and the specific meanings of s_x and s_y are given in the following equation.

$$\begin{cases} s_x = \dfrac{\mathrm{d}}{\mathrm{d}t}\ddot{x} \\ s_y = \dfrac{\mathrm{d}}{\mathrm{d}t}\ddot{y} \end{cases} \tag{8}$$

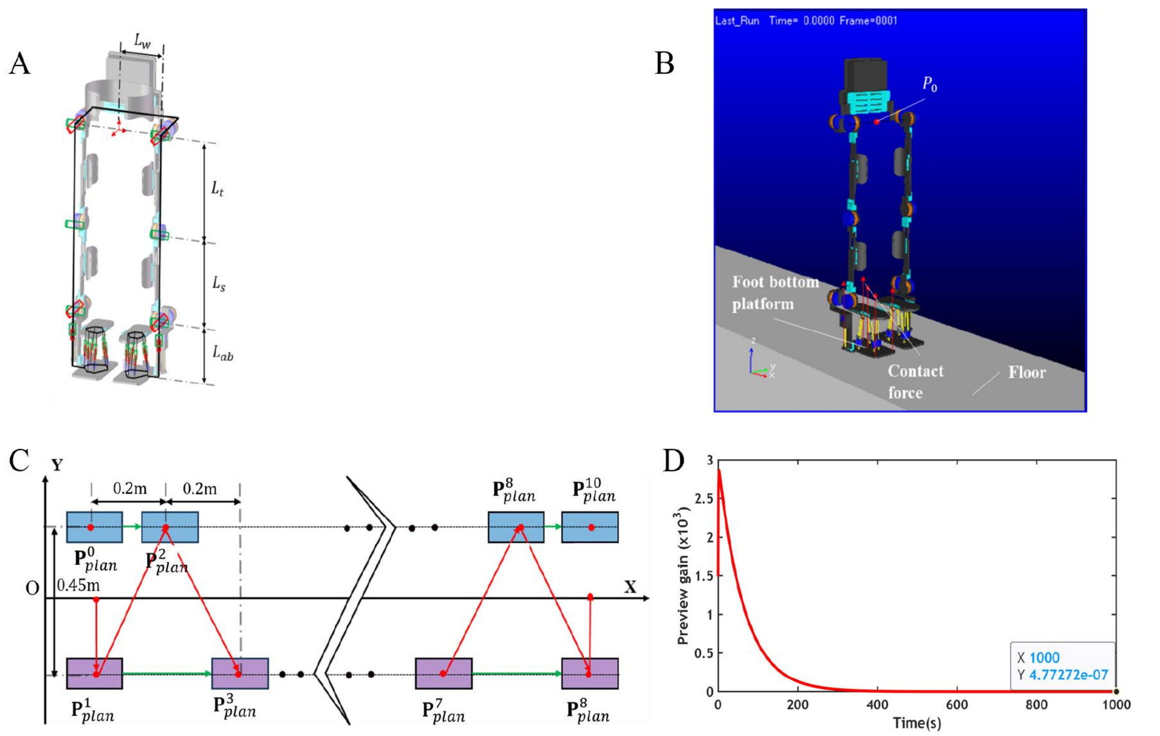

Figure 4. Simulation environment and parameter analysis. (A) ABW leg mechanism model in SOLIDWORKS 2020; (B) Simulation environment of the ABW leg mechanism in ADAMS 2020; (C) Planned foot position; (D) Preview action gain. ABW, Auto Balance Wang.

Since the solution process of gait trajectories in x and y directions is the same, only the specific solution process of trajectories in x direction is described next.

By taking s as an input to Eq. (7), it can be transformed into a control problem, and the state equation of this control system can be expressed as the following equation:

$$\begin{cases} \frac{\mathrm{d}}{\mathrm{d}t}\begin{bmatrix}x\\ \dot{x}\\ \ddot{x}\end{bmatrix} = \begin{bmatrix}0&1&0\\0&0&1\\0&0&0\end{bmatrix}\begin{bmatrix}x\\ \dot{x}\\ \ddot{x}\end{bmatrix}+\begin{bmatrix}0\\0\\1\end{bmatrix}s_x \\ P_x = \begin{bmatrix}1&0&-\frac{z_c}{g}\end{bmatrix}\begin{bmatrix}x\\ \dot{x}\\ \ddot{x}\end{bmatrix}\end{cases} \tag{9}$$

System (9) can be discretised in terms of the sampling time (Δt):

$$\begin{cases} \mathbf{r}_{j+1} = \mathbf{A}\mathbf{r}_j + \mathbf{B}s_{xj} \\ P_{xj} = \mathbf{C}\mathbf{r}_j \end{cases} \tag{10}$$

$$\text{where}\begin{cases} \mathbf{r}_k \equiv [x(j\Delta t), \dot{x}(j\Delta t), \ddot{x}(j\Delta t)]^{\mathrm{T}} \\ \mathbf{A} \equiv \begin{bmatrix}1&\Delta t&\Delta t^2/2\\0&1&\Delta t\\0&0&1\end{bmatrix} \\ \mathbf{B} \equiv \begin{bmatrix}\Delta t^3/6\\ \Delta t^2/2\\ \Delta t\end{bmatrix} \\ \mathbf{C} \equiv \begin{bmatrix}1&0&-z_c/g\end{bmatrix} \end{cases} \tag{11}$$

With the reference ZMP location $\mathbf{P}^{ref}_{xj}$, the performance index J can be defined as:

$$J = \sum_{i=j}^{\infty}\left(Q_e e_i^2 + \Delta\mathbf{r}_i^{\mathrm{T}}\mathbf{Q}_r\Delta\mathbf{r}_i + Q_s\Delta s_{xi}^2\right) \tag{12}$$

where $e_j \equiv \boldsymbol{P}^{ref}_{xj} - \boldsymbol{P}_{xj}$, $\Delta r_j \equiv r_j - r_{j-1}$ and $\Delta S_{xj} \equiv S_{xj} - S_{xj-1}$.$Q_e$, Q_s and $\boldsymbol{Q}_r$ are weighting factors.

With N_L step future reference ZMP locations at every sampling time, the input s_{xj} in Eq. (11) can be obtained as Eq. (13) by minimizing index J, and s_{xj} can be calculated in the same way:

$$s_{xj} = -K_e\sum_{i=0}^{j} e_{xi} - \mathbf{K}_r\mathbf{r}_{xj} + \sum_{k=1}^{N_L} K_{Pk}P^{\mathrm{ref}}_{xj+k} \tag{13}$$

where K_e, $\mathbf{K}_r$ and K_{pk} are the gains. Finally, the COM position $\mathbf{P}_{comj}=(x_j, y_j)$ can be obtained by the above formula.

If the i-th planned landing point $\boldsymbol{P}^{i}_{plan}$ corresponds to the left foot, then both $\boldsymbol{P}^{i}_{plan}$ and $\boldsymbol{P}^{i+2}_{plan}$ serve as the landing points for the left foot, while both $\boldsymbol{P}^{i-1}_{plan}$ and $\boldsymbol{P}^{i+1}_{plan}$ serve as the landing points for the right foot. The trajectory curve $\boldsymbol{P}^{i}_{5tc}$ of the left foot extends between $\boldsymbol{P}^{i}_{plan}$ and $\boldsymbol{P}^{i+2}_{plan}$, while the trajectory curve $\boldsymbol{P}^{i}_{10tc}$ of the right foot extends between $\boldsymbol{P}^{i-1}_{plan}$ and $\boldsymbol{P}^{i+1}_{plan}$, and can be accurately represented by a five times spline curve.

Table 3. Key parameters of the ABW leg mechanism

Parameters	L_w	L_t	L_s	L_{ab}
Values	0.225 m	0.45 m	0.4 m	0.25 m

Note: ABW, Auto Balance Wang.

Table 4. Configuration parameters of the contact force between the floor and foot bottom platform

Parameters	Normal force				Friction force	
	Stiffness	Force exponent	Damping	Penetration depth	Static friction coefficient	Dynamic friction coefficient
	1.0E+08 N/m	1.5	50 Ns/m	1.0E-04 m	0.6	0.2

Table 5. Initial state parameters of the ABW

Parameters	Heights of the COM plane z_0 (m)	Starting position of the waist centre $\mathbf{P}_0$ (m)	Starting position of the left ankle centre $\mathbf{P}_5$ (m)	Starting position of the right ankle centre $\mathbf{P}_{10}$ (m)	Swing foot lifting height H_f (m)	Initial velocity and acceleration
Values	1	$[0,0,1.1]^T$	[0,0.225,0.25]	[0,-0.225,0.25]	0.05	0

Note: ABW, Auto Balance Wang.

Table 6. Planned foot position

Step (n)	1	2	3	4	5	6	7	8	9	10
s_x^n	0 m	0.45 m	0.45 m	0.45 m	0.45 m	0.45 m	0.45 m	0.45 m	0.45 m	0 m
s_y^n	0.2 m	0.2 m	0.2 m	0.2 m	0.2 m	0.2 m	0.2 m	0.2 m	0.2 m	0.2 m

Validity verification

Figure 4A displays the model of the ABW leg mechanism, while **Table 3** outlines the key feature parameters of this model. The primary structure of the mechanism is constructed from aluminium alloy, known for its high load carrying capacity and lightweight nature. The simulation environment within ADAMS can be observed in **Figure 4B**. The initialisation state parameters for the ABW are detailed in **Table 4**.

To simulate the walking process of the ABW on a flat terrain, a flat floor is incorporated, establishing a solid-to-solid contact force between the floor and the foot platform. Based on the material properties of the floor and foot platform, the configuration parameters for this contact force can be found in **Table 5** [27]. The planned foot position setup is depicted in **Figure 4C**. The exoskeleton proceeded to walk along the x-axis on the flat terrain for 10 steps, with step length parameters outlined in **Table 6**.

To investigate the feasibility of the online gait generation algorithm, the initial conditions were established: $\boldsymbol{T}_{gait}$=1s, Q_e=1, $Q_s=1\times10^{-6}$, $\boldsymbol{Q}_r$=0 and N_L=500. To validate the dynamic self-balancing walking capability of the exoskeleton robot, this study conducted a preliminary flat-ground walking experiment specifically for the online gait generation algorithm. In this preliminary experiment, the gait period T_{gait} was set to 2.5 s, with a sampling time of Δt=5 ms. The weighting factors employed were Q_e=1, $Q_s=1\times10^{-6}$ and $\boldsymbol{Q}_r$=0. The preview action gain, K_{pk} , is illustrated in **Figure 4D**, which indicates that the preview gain approaches zero when N_L exceeds 1,000. Consequently, the future parameter factor N_L is set to 1,000.

Results

To assess the feasibility of the online gait generation algorithm under a specific initial condition, the generated gaits are illustrated in **Figure 5A**. The yellow round solid line is the COM trajectory, the green triangular solid line is the right foot trajectory, and the red triangular solid line is the left foot trajectory. **Figures 5B-5C** present the gaits for walking on flat ground corresponding to the specific initial condition.

The COM trajectory is represented by the dashed line, the ZMP trajectory by the solid line, and the planned ZMP trajectory by the dotted line. The maximum tracking error of ZMP in the x-direction (ΔZMP_x) is 0.0372 m, while in the y-direction (ΔZMP_y) it is 0.0838 m.

Through numerical analyses, it was observed that the tracking error is inversely proportional to the factor Q_e. Specifically, when Q_e=1,000 the tracking error reduces to $\Delta ZMP_x=8.0\times10^{-5}$ m and $\Delta ZMP_y=1.7\times10^{-4}$ m. The COM trajectory and bipedal trajectory were recalculated based on the initial conditions, input into the ABW

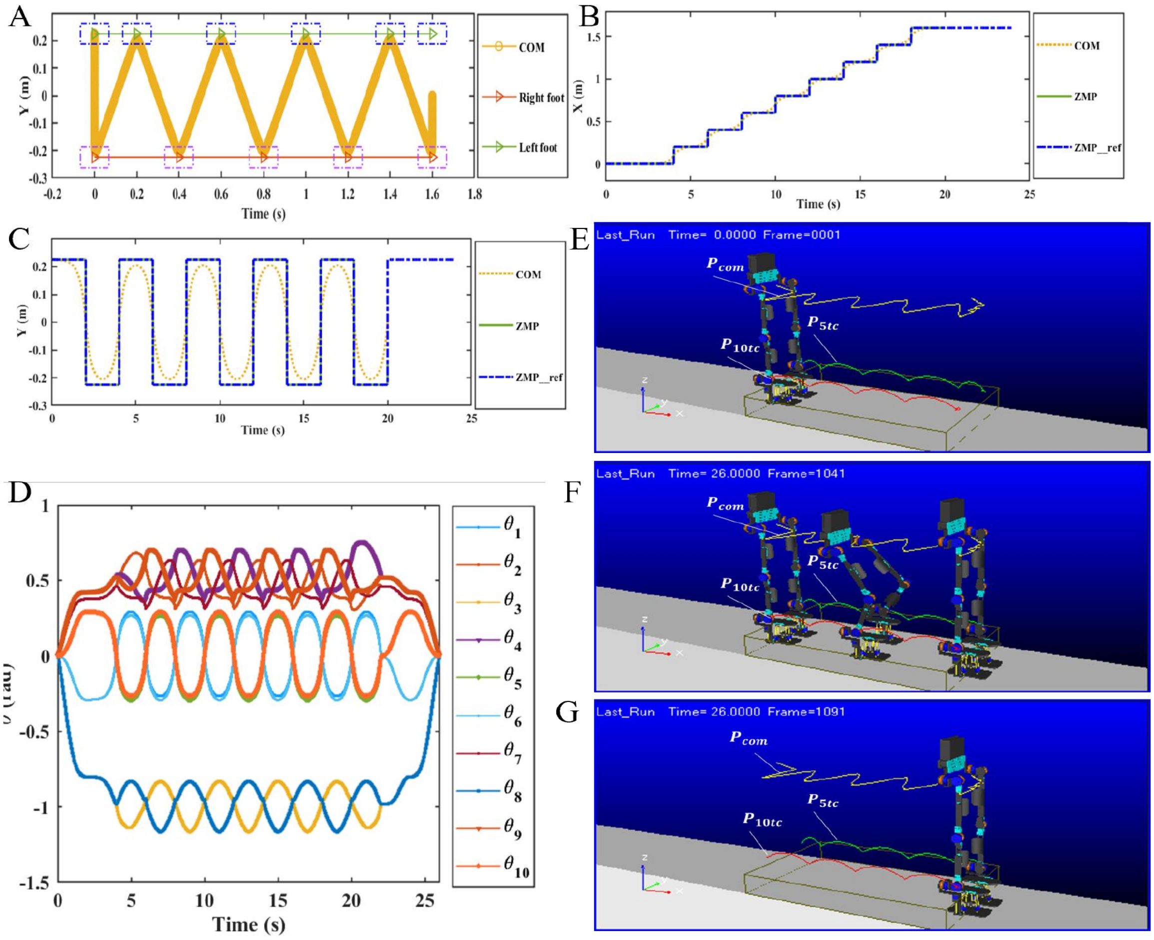

Figure 5. Analysis of results. (A) Generated trajectories based on MPC and ZMP online gait generation algorithms; (B) Generated trajectories in the x-direction; (C) Generated trajectory in the y-direction; (D) Calculated joint angles; (E) Initial state of the self-balancing flat walking experiment; (F) Intermediate state of the self-balancing flat walking experiment; (G) Final state of the self-balancing flat walking experiment. MPC, Model Predictive Control; ZMP, Zero Moment Point.

inverse kinematics model, and used to calculate the 10 joint angles of the exoskeleton as depicted in **Figure 5D**. Considering the offset between the centre of gravity and the waist's centre of gravity, the calculated joint angle data were input into the Adams driver for simulation experiments. The initial, intermediate, and final states of the lower limb exoskeleton in the experiment are illustrated in **Figures 5E, 5F, and 5G**, demonstrating the feasibility and stability of the exoskeleton for flat ground walking. $\mathbf{P}_{com}$ represents the trajectory curve of the waist centre, $\mathbf{P}_{5tc}$ denotes the trajectory curve of the left ankle joint centre, and $\mathbf{P}_{10tc}$ indicates the trajectory curve of the right ankle joint centre.

Preliminary simulation experiments on flat terrain revealed that the numerical simulation trajectory closely aligned with the planned trajectory, confirming the dynamic self-balancing walking ability of the exoskeleton. However, slight deviations were noted in the simulation experiments, which may be attributed to the parameterization of the contact force between the exoskeleton's plantar platform and the ground, potentially leading to occasional slippage.

Conclusion

In this study, we designed a novel self-balancing lower limb exoskeleton for the rehabilitation training of quadriplegic patients on flat ground, eliminating the need for crutches. Initially, we derived the forward and inverse kinematic solutions of the ABW leg mechanism using both the D-H method and a geometric approach. Next, we established the workspace expressions for the SFS and DFS stages based on the geometric constraint relationships among the exoskeleton's link components. Additionally, we analysed an online gait generation algorithm grounded in MPC theory and ZMP theory to create a robotic gait trajectory that satisfies the stability requirements for bipedal walking. We subsequently evaluated the effectiveness of this online gait generation algorithm, with results indicating a high degree of consistency between the generated trajectory and the planned trajectory, thereby confirming the algorithm's effectiveness. However, during the assessment of the dynamic self-balancing walking capability, we observed that the tracking error of the generated trajectory was relatively large, potentially impeding the exoskeleton's ability to achieve dynamic self-balancing walking. Further numerical analysis revealed that the tracking error diminishes as the factor Q_e increases, becoming negligible at a value of 1000. In conclusion, we conducted preliminary simulation experiments on flat terrain to validate the dynamic self-balancing walking ability of the exoskeleton.

Future research will aim to evaluate performance across various environments and enhance the mechanical structure design to reduce weight.

Author contributions: Jiaqing Wang was responsible for conceptualization, methodology, and writing of the original draft. Hongwei Tan handled data curation, formal analysis, and visualization. Shi Gu contributed to investigation, validation, and writing through review and editing. Jianchao Sun was in charge of software development, resources, and data analysis. Xuezhi Yin oversaw supervision and project administration. Renling Zou provided supervision, participated in review and editing of the manuscript, and was responsible for funding acquisition as the corresponding author.All authors have read and agreed to the final version of the manuscript.

References

[1] National Spinal Cord Injury Statistical Center. 2023 SCI Data Sheet: Traumatic Spinal Cord Injury Facts and Figures at a Glance. University of Alabama at Birmingham, 2023.

[2] Zbogar D, Eng JJ, Miller WC, et al. Movement repetitions in physical and occupational therapy during spinal cord injury rehabilitation. Spinal Cord 2017;55(2):172-179.

[3] Hornby TG, Rafferty MR, Pinto D, et al. Cost-Effectiveness of High-intensity Training vs Conventional Therapy for Individuals With Subacute Stroke. Arch Phys Med Rehabil 2022;103(7S):S197-S204.

[4] Zhang B, Liu T, Pecht MG, et al. Recent development of unpowered exoskeletons for lower extremity: A survey. IEEE Access 2021;9:138042-138056.

[5] Watanabe H, Marushima A, Kadone H, et al. Efficacy and Safety Study of Wearable Cyborg HAL (Hybrid Assistive Limb) in Hemiplegic Patients With Acute Stroke (EARLY GAIT Study): Protocols for a Randomized Controlled Trial. Front Neurosci 2021;15:666562.

[6] Megía-García A, del-Ama AJ, Lozano-Berrio V, et al. Safety, Feasibility and Acceptance with HANK Ambulatory Robotic Exoskeleton in Incomplete Spinal Cord Injury Patients. Converging Clinical and Engineering Research on Neurorehabilitation IV 2022;935-939.

[7] Shanghai Fourier Intelligent Technology Co., Ltd. ExoMotusTM lower limb rehabilitation robot series products. Available at: https://exoskeletonreport.com/2019/01/fourier-intelligence-announces-the-fourier-exoskeleton-robotics-open-platform-system-exops/

[8] Li Y, Fan T, Qi Q, et al. Efficacy of a Novel Exoskeletal Robot for Locomotor Rehabilitation in Stroke Patients: A Multi-center, Non-inferiority, Randomized Controlled Trial. Front Aging Neurosci 2021;13:706569.

[9] Høyer E, Opheim A, Jørgensen V. Implementing the exoskeleton Ekso GTTM for gait rehabilitation in a stroke unit - feasibility, functional benefits and patient experiences. Disabil Rehabil Assist Technol 2022;17(4):473-479.

[10] Kwon SH, Lee BS, Lee HJ, et al. Energy Efficiency and Patient Satisfaction of Gait With Knee-Ankle-Foot Orthosis and Robot (ReWalk)-Assisted Gait in Patients With Spinal Cord Injury. Ann Rehabil Med 2020;44(2):131-141.

[11] Pais-Vieira C, Allahdad M, Neves-Amado J, et al. Method for positioning and rehabilitation training with the ExoAtlet ® powered exoskeleton. MethodsX 2020;7:100849.

[12] Juszczak M, Gallo E, Bushnik T. Examining the Effects of a Powered Exoskeleton on Quality of Life and Secondary Impairments in People Living With Spinal Cord Injury. Top Spinal Cord Inj Rehabil 2018;24(4):336-342.

[13] Han J, Hyun D, Jung K, et al. Ergonomic Design Strategy for Crutches of a Lower-limb Exoskeleton for Paraplegic Individuals: An Experimental Study. Proceedings of the Human Factors and Ergonomics Society Annual Meeting 2018;1012-1016.

[14] Hyun DJ, Lim H, Park S, et al. Walking propulsion generation in double stance by powered exoskeleton for paraplegics. Rob Auton Syst 2019;116:24-37.

[15] Chen G, Qi P, Guo Z, et al. Mechanical design and evaluation of a compact portable knee-ankle-foot robot for gait rehabilitation. Mech Mach Theory 2016;103:51-64.

[16] Sawicki GS, Ferris DP. A pneumatically powered knee-ankle-foot orthosis (KAFO) with myoelectric activation and inhibition. J Neuroeng Rehabil 2009;6:23.

[17] Kajita S, Kanehiro F, Kaneko K, et al. The 3D linear inverted pendulum mode: a simple modeling for a biped walking pattern generation. Proceedings 2001 IEEE/RSJ Internation-

al Conference on Intelligent Robots and Systems. Expanding the Societal Role of Robotics in the the Next Millennium 2001;231:239-246.

[18] Kajita S, Kanehiro F, Kaneko K, et al. Biped walking pattern generation by using preview control of zero-moment point. 2003 IEEE International Conference on Robotics and Automation 2003;1622:1620-1626.

[19] Wang H, Yin Y. Online Gait Generation for an Exoskeleton Used in Lower Limb Rehabilitation. Stud Inf Control 2020;29:205-217.

[20] Logan BM, Bowden D, Hutchings RT. McMinn's Color Atlas of Lower Limb Anatomy E-Book. Amsterdam (Netherlands). Elsevier Health Sciences, 2017.

[21] Protection B, Labour M. Human Dimensions of Chinese Adults, GB 10000-1988. National Standards of People's Republic of China 1988.

[22] Gao SL. Practical anatomy atlas. Shanghi (China). Shanghai Science and Technology Press, 2012.

[23] Craig J. Introduction to Robotics: Mechanics and Control, Global Edition. München (Germany) Pearson Deutschland, 2021.

[24] Lopez A, Gutierrez F, Tacué J, et al. Design and construction of a bipedal robot prototype for experimentation in balance tests during the static standing phase. 2021 IEEE 5th Colombian Conference on Automatic Control (CCAC) 2021;7-12.

[25] Katayama T, Ohki T, Inoue T, et al. Design of an optimal controller for a discrete-time system subject to previewable demand. Int J Control 1985;41:677-699.

[26] Shimmyo S, Sato T, Ohnishi K. Biped Walking Pattern Generation by Using Preview Control Based on Three-Mass Model. IEEE Trans Ind Electron 2013;60:5137-5147.

[27] Giesbers J. Contact mechanics in MSC Adams. University of Twente 2012.

Progress in Medical Devices
ISSN: 2957-5478

Zentime

Research Article https://doi.org/10.61189/392182sdzooq

Optimal design and experimental study of Mg alloy electrodes for tissue welding

Juxiao Wang, Lin Mao, Weiwei Fan, Chengli Song

Shanghai Institute for Minimally Invasive Therapy, School of Health Science and Engineering, University of Shanghai for Science and Technology, Shanghai 200093, China.

Corresponding author: Lin Mao.

Declaration of conflict of interest: None.

Received December 31, 2024; Accepted February 19, 2025; Published March 31, 2025

Highlights

- Three types of circular electrodes with varying thicknesses were designed to achieve weight reduction, accompanied by support structures for intestinal tissue on both sides.
- The mechanical properties of the three electrode configurations were systematically compared to determine the optimal thickness for welding.
- In vitro tissue experiments successfully welded the tissue, identifying the optimal welding parameters.

Abstract

Objective: To investigate electrode weight reduction through structural modifications, focusing on variations in the thickness of circular electrodes to meet mechanical requirements. Additionally, optimal welding parameters were identified via experimental methods. **Methods:** Three electrode thicknesses were designed: 0.2 mm (T1), 0.3 mm (T2), and 0.4 mm (T3). The finite element method was used to analyze the stress, strain, and thermal effects on the surrounding tissue. In vitro tissue experiments assessed the mechanical strength of the anastomosis by measuring tear force and rupture pressure. **Results:** Among the three designs, the T3 electrode exhibited the lowest strain (1.2%) and stress (122.26 MPa). Thermal simulations showed maximum tissue damage of 53.3% and minimum damage of 48.6%. The maximum tear force (9.87±0.83 N) and rupture pressure (222.88±13.48 mmHg) were achieved with a compression force of 20 N, welding power of 160 W, and welding time of 8 seconds. **Conclusion:** T3 electrode demonstrated superior mechanical performance in the finite element analysis and successfully completed in vitro welding while minimizing electrode weight. Optimal welding parameters were identified.

Keywords: Radiofrequency tissue welding, electrode structure, finite element simulation, anastomosis strength

Introduction

Colorectal cancer has become the fourth leading cause of cancer-related mortality worldwide, accounting for approximately 900,000 deaths annually. In my country, it ranks as one of the most common malignancies of the digestive tract, with incidence and mortality rates placing third and fifth, respectively, among all cancers [1, 2]. Currently, the standard treatment involves surgical resection of the affected intestinal tissue, followed by anastomosis of the remaining stump [3]. Common methods for anastomosis include manual suturing and stapler anastomosis [4]. However, sutures and staples used in manual methods can remain in the body, potentially causing foreign body reactions. Additionally, complications such as bleeding and anastomotic fistula may arise from the procedure [5-7].

To improve the quality of intestinal tissue anastomosis, radiofrequency-based tissue welding technology has been proposed. This method uses a high-frequency current ranging from 300 to 500 kHz, which, under the combined influence of radiofrequency energy and mechanical pressure, generates heat through bioimpedance. This thermal effect denatures proteins in the intestinal tissue, leading to the formation of adhesions and the rapid creation of a continuous anastomosis [8, 9]. The technology offers several advantages, including a reduced risk of tissue infection, high suturing efficiency, no

Address correspondence to: Lin Mao, Shanghai Institute for Minimally Invasive Therapy, School of Health Science and Engineering, NO.516 Jungong Road, Shanghai 200093, China. Tel: +86-21-55572159. E-mail: linmao@usst.edu.cn.

Table 1. Electrode material properties

Name	Density, ρ (Kg/m^3)	Young's modulus (MPa)	Poisson ratio	YS (MPa)	UTS (MPa)	Thermal conductivity, λ (W/m/K)
WE43 magnesium alloy	1,866	45,270	0.27	162	250	51.3
Copper alloy	8,960	1.25e7	0.345	33.5	152	400

Note: YS, Yield strength; UTS, Ultimate tensile strength.

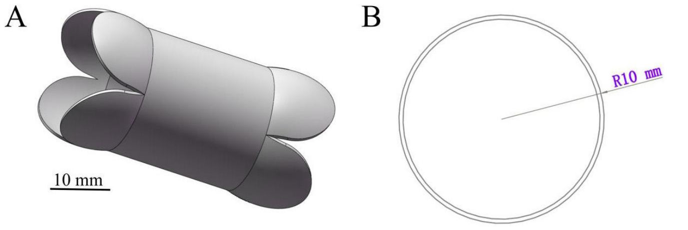

Figure 1. Overall electrode structure and thickness variations. (A) Overall electrode design; (B) Side view of the welding area with three different thicknesses (0.2 mm, 0.3 mm, 0.4 mm).

foreign material residue, and ease of operation [10].

Over the years, tissue welding technology based on radio frequency has seen significant advancements. In the late 1990s, the Ukrainian Paton Institute first proposed the use of radiofrequency currents for tissue welding [11]. Holmer et al. later confirmed that dual-electrode radiofrequency welding is an innovative method for achieving intestinal tissue anastomosis [12]. Zhao et al. used copper as the electrode material, designing two different electrode structures for intestinal tissue anastomosis [13]; however, the need for a second operation to remove the copper electrode impeded recovery. This led to the development of implantable electrodes as a preferred option for welding applications. Zong et al. were the first to use degradable magnesium alloys as welding electrodes for intestinal tissue anastomosis [14]. Mao et al. improved welding strength and reduced thermal damage by optimizing the structure of magnesium alloy electrodes, though they did not address concerns regarding in vivo fixation and electrode weight [15].

As electrodes used in tissue welding remain in the human body for extended periods, excessive electrode weight can negatively impact the subsequent recovery of intestinal tissue [16]. This study aims to investigate methods for reducing electrode weight. Three circular electrode designs with varying thicknesses were developed, incorporating support structures for the intestinal tissue on both sides. These structures were intended to enhance tissue fixation during the welding process and provide support to the anastomotic area during the healing phase. The forces acting on the electrodes were analyzed through a combined force-electrothermal simulation, and temperature variations at the anastomosis, along with the extent of thermal damage to the tissue, were assessed. Furthermore, optimal welding parameters were identified through in vitro tissue welding experiments, and the effects of different output powers on tissue pathological changes were evaluated. These findings lay the groundwork for future in vivo studies.

Materials and methods

Electrode structure design

The electrode structure consists of two main components: the central region, designated for welding intestinal tissue, and two end sections, which support the tissue and generate friction to prevent tissue retraction. The overall design of the electrode is shown in **Figure 1A**. To minimize electrode weight while evaluating their pressure resistance limits, three circular ring electrodes with varying thicknesses-0.2 mm, 0.3 mm, and 0.4 mm-were designed (**Figure 1B**). The thickness of the central region is consistent with that of the end sections across all three electrodes. Each electrode has an outer diameter of 20 mm, a length of 20 mm, and inner diameters of 19.6 mm, 19.4 mm, and 19.2 mm, respectively. The supporting structures at both ends are symmetrical, with a single-side length of 10 mm.

Electrode material characteristics

The outer electrode in the experiment was made of copper, which is known for its excellent electrical conductivity, thermal conductivity, and antibacterial properties [17]. The inner electrode was constructed from a WE43 magnesium alloy, designed to remain in the body following the welding process. The WE43 alloy is commercially available and is recognized for its good biocompatibility and ability to degrade gradually during the recovery of intestinal tissue [18]. The material properties of both electrodes are summarized in **Table 1** [19-21].

Mechanical simulation

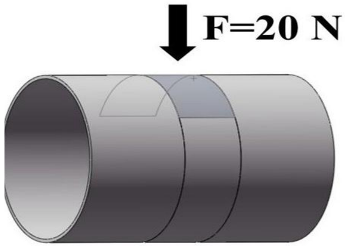

Figure 2. Force loading schematic.

Since the electrode primarily applies force to the central region during the welding process, the simulation model was simplified by excluding the support area. To accurately model the force distribution, the outermost surface of the central section of the electrode was divided into two regions: one-third and two-thirds of the circumference.

The mechanical analysis of the three electrodes was performed using ANSYS 2020 R2 software. After defining the boundary conditions for the finite element model, it was noted that the external copper electrode contacts only the middle third of the inner electrode (indicated by the dark region). Based on the force values from the corresponding experimental study, a 20 N force was applied to the middle third of the electrode, as shown in **Figure 2** [22].

Electrothermal simulation

The welding process was simulated using COMSOL 5.6 software. Since the support area is not involved in the welding region, it was excluded from the simulation model. As biological tissues were involved, the Pennies bioheat transfer model was applied. The governing equation for this model was:

$$\rho c \frac{\partial T}{\partial t} = \nabla \cdot (k \nabla T) + \rho_b c_b \omega (T_b - T) + Q \tag{1}$$

where ρ was the tissue density, c denoted the specific heat, k indicated the thermal conductivity, and T is the temperature. Additionally, ρ_b referred to blood density, c_b was the specific heat of blood, T_b represented arterial temperature, ω was the blood perfusion rate, and Q denoted the power absorption. Tissue thermal damage was calculated using the Arrhenius equation:

$$\Omega(\tau) = \int_0^{\tau} A e^{\frac{-E_a}{RT}} dt \tag{2}$$

where $\Omega(\tau)$ represented the degree of tissue damage, τ was the heating time, A denoted the frequency factor, E_a was the activation energy, R representd the molar gas constant, and T was the absolute temperature.

RF AC voltages of 120 W, 140 W, and 160 W were applied to the outer copper electrode, while zero voltage was applied to the inner magnesium electrode. The total simulation duration was 10 seconds, and the ambient temperature was set to 25 °C at t=0.

In vitro tissue welding experiment

Fresh porcine small intestines were obtained from a local slaughterhouse, rinsed briefly with 0.9% saline, and sectioned into 60-70 mm pieces. These were stored in phosphate buffer to maintain freshness and moisture. The LigaSure vascular sealing system (Valleylab, Covidien, USA) was used to supply radiofrequency power for tissue fusion. The intestinal tissue was placed on the surface of the magnesium alloy electrode (**Figure 3B**) in a mucosal-serosa orientation. The copper electrode applied pressure to the tissue, with pressure monitored using a gauge. A schematic of the welding experiment setup is shown in **Figure 3A**. Nine welding groups were designed with varying welding times and power levels, each replicated five times. Details of the experimental groups are outlined in **Table 2**.

Anastomosis strength test

The strength of the anastomosis was assessed using avulsion force and burst pressure tests. The avulsion force refers to the maximum tensile force applied to the anastomosis until it ruptured during stretching, while burst pressure referred to the maximum pressure at which the anastomosis began to leak during perfusion. For the tensile force test, the ends of the anastomotic tissue were secured in clamps of a universal material testing machine, and the tissue was stretched at a rate of 10 mm/s [15]. The tensile force at rupture was recorded (**Figure 3D**). For the burst pressure test, 0.9% saline was injected into the welded intestinal tissue at a constant rate of 2 ml/min, with the pressure value noted when leakage occurred from the anastomotic area (**Figure 3C**) [23].

Histopathological examination

Intestinal tissue samples, both pre- and post-welding, were collected and preserved in a neutral formalin solution. Histopathological examination was performed using a fluorescence microscope following standard procedures, including dehydration, clarification, paraffin em-

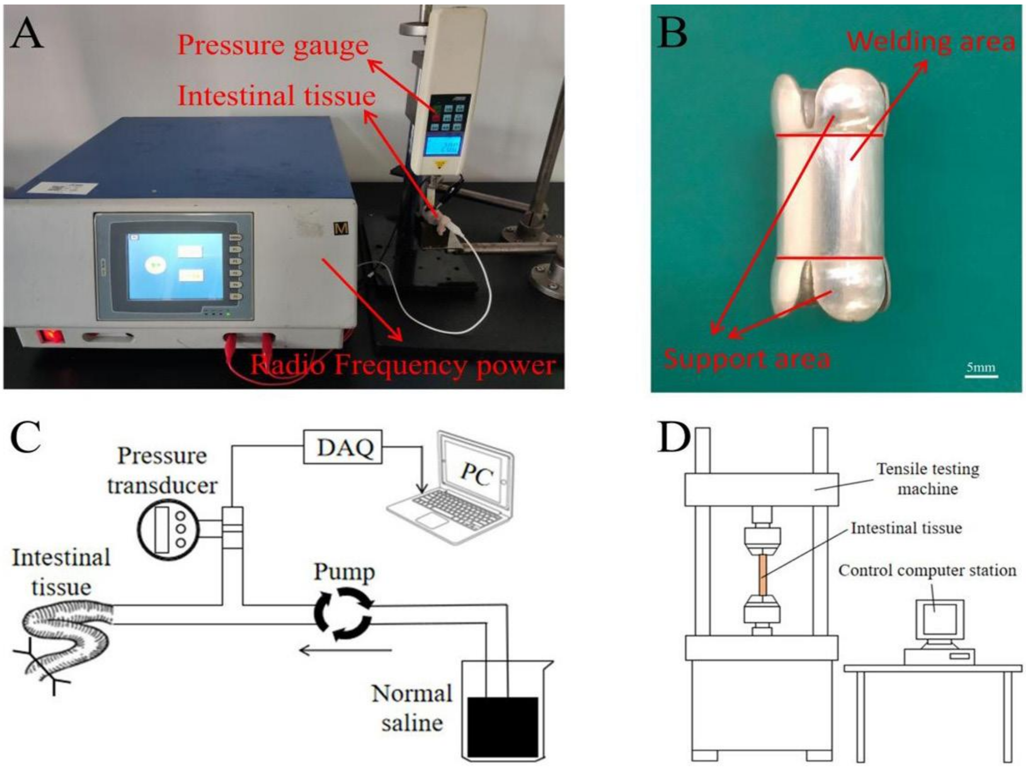

Figure 3. Experimental tissue welding in vitro. (A) Intestinal tissue welding platform; (B) WE43 magnesium alloy electrode; (C) Schematic diagram of burst pressure test; (D) Schematic diagram of avulsion force test. DAQ, Data acquisition card; PC, Personal computer.

Table 2. Welding experiments of each group

Group	Welding time (s)	Energy power (W)
1	6	120
2	8	
3	10	
4	6	140
5	8	
6	10	
7	6	160
8	8	
9	10	

bedding, sectioning, baking, hematoxylin-eosin staining, and neutral resin mounting.

Results

Electrode mechanics simulation results

A pressure of 20 N was applied to the circular electrode, and the strain distribution results are shown in **Figure 4A-C**. Under this pressure, the maximum deformations for the T1, T2, and T3 electrodes were 1.8903 mm, 0.5526 mm, and 0.2319 mm, respectively, with corresponding maximum strains of 9.2%, 2.8%, and 1.2%. The T3 electrode exhibited the smallest deformation, while the T1 electrode showed the largest. The maximum strains for all three electrodes occurred at the pressure application point, and the deformation decreased with increasing electrode thickness. All three electrodes were made of WE43 magnesium alloy, a material with an elongation range of 4% to 8% [24]. The strain in the T1 electrode (9.2%) exceeded the material's elongation limit, suggesting that fracture deformation would occur under the applied 20 N pressure. In contrast, the strains in the T2 (2.8%) and T3 (1.2%) electrodes remained below the material's elongation limit. Therefore, while the T1 electrode did not meet mechanical requirements due to excessive strain, the T2 and T3 electrodes exhibited strains within the allowable range, indicating they would meet the mechanical demands of the welding experiment.

The stress simulation results are presented in **Figure 4D-F**. Under a pressure of 20 N, the maximum stresses for the T1, T2, and T3 electrodes were 321.91 MPa, 181.43 MPa, and 122.26 MPa, respectively. The T3 electrode exhibited the lowest stress, while the T1 electrode experienced the highest. Additionally, stress in the electrode decreased with increasing electrode thickness. The yield strength of WE43 magnesium alloy is approximately 180-260 MPa [24]. The stresses in the T1 (321.91 MPa) and T2 (181.43 MPa) electrodes exceed the yield strength of the WE43 magnesium alloy,

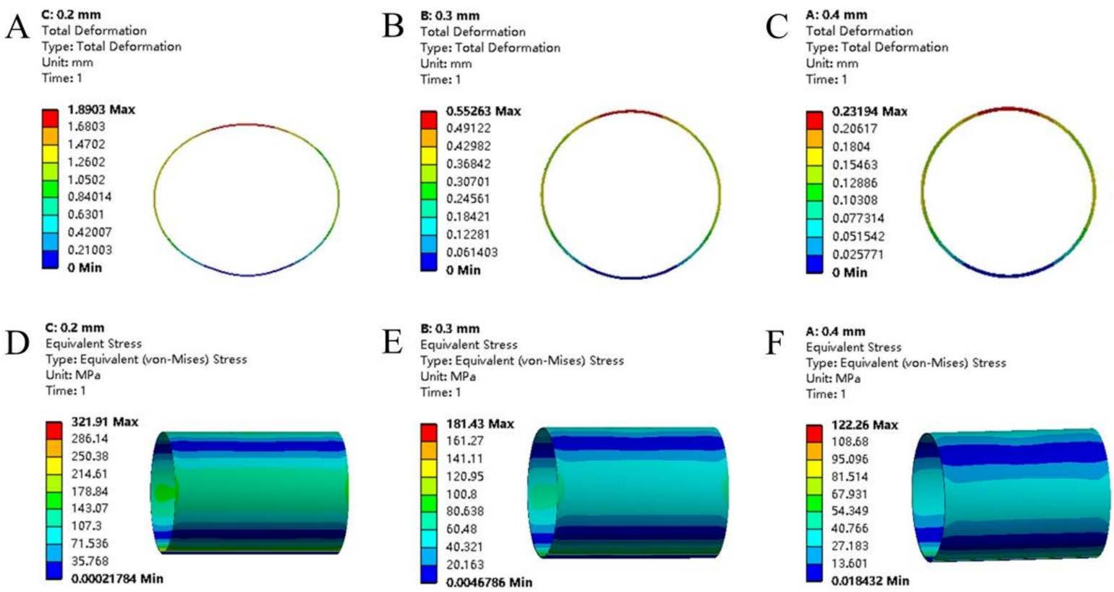

Figure 4. Mechanical simulation results of electrodes with different thicknesses (0.2 mm, 0.3 mm, 0.4 mm). (A-C) Simulation results of three types of electrode strain; (D-F) Simulation results of three types of electrode stress.

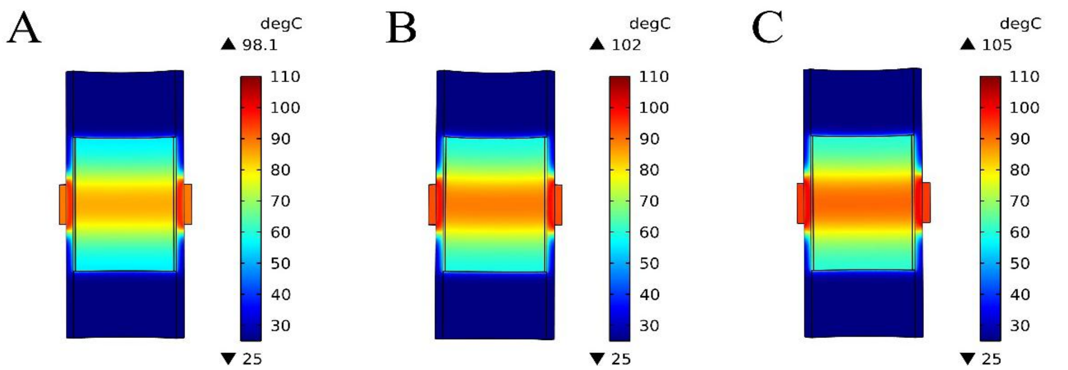

Figure 5. Electrothermal simulation results at different powers. (A) 120 W; (B) 140 W; (C) 160 W.

suggesting both electrodes would undergo plastic deformation, resulting in irreversible shape changes. From a stress perspective, the T1 and T2 electrodes cannot withstand the applied force during the experiment, while the T3 electrode satisfies the mechanical requirements.

Electrothermal simulation results

The temperature distribution of intestinal tissue at different power levels is illustrated in **Figure 5A-C**. As the power increases, the maximum temperature within the model also rises. The figure showed that the high-temperature region was primarily concentrated under the copper electrode, with the extent of the high-temperature area expanding as power increased. As seen in **Figure 6B**, the average maximum tissue temperatures at three different power levels were 65.1 °C, 68.0 °C, and 69.6 °C, respectively. All of these temperatures exceed 60 °C, indicating that successful welding can be achieved. Thermal damage to the tissue, shown in **Figure 6D**, begins to appear three seconds after power is applied and increases rapidly. After four seconds, the thermal damage area starts to expand gradually. At the three power levels, the average maximum thermal damage to the tissue was 48.6%, 51.6%, and 53.3%, respectively.

Additionally, two points, labeled a and b, were marked at the center and edge of the inner electrode (**Figure 6A**) to monitor temperature changes at different tissue sites. As shown in **Figure 6C**, the temperature at point b was significantly lower than at point a. The temperature at point a rose rapidly at first, then increased more slowly, while the temperature at point b increased steadily and gradually.

Biomechanical properties of anastomosis

In this experiment, the T3 electrode was used

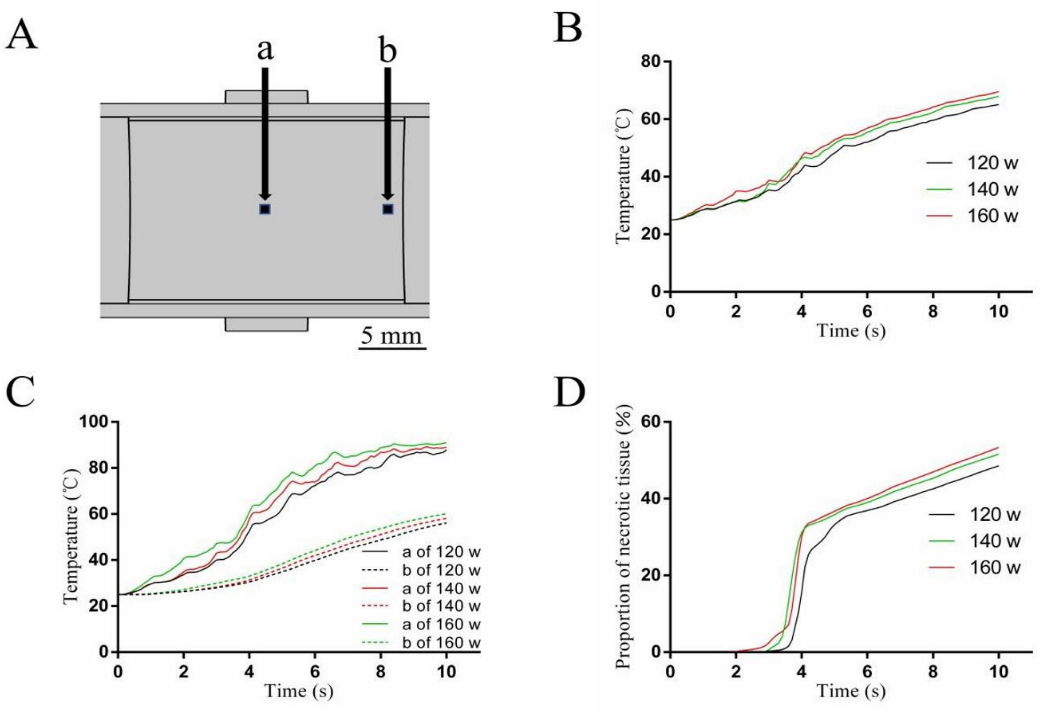

Figure 6. Changes in tissue temperature and proportion of necrotic tissue under three output powers. (A) Domain point location of T3 electrode; (B) Average temperature change of the welding area; (C) Temperature changes at domain points; (D) Proportion of necrotic tissue.

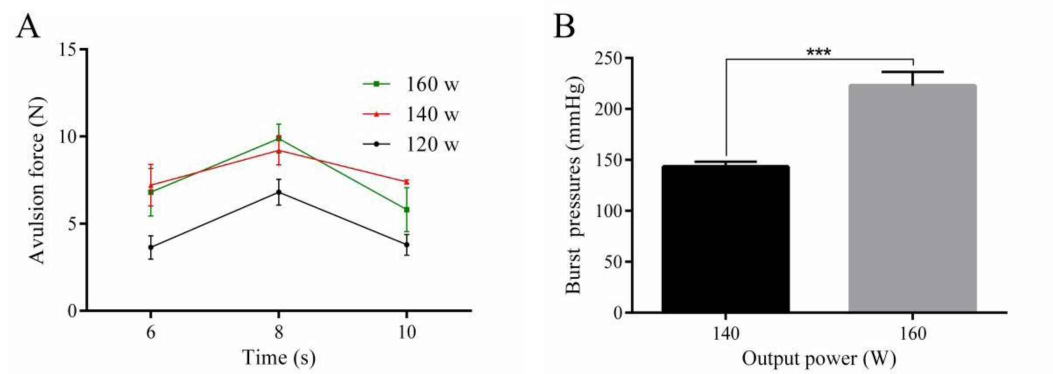

Figure 7. Biomechanical properties of anastomotic tissues under different welding parameters. (A) The avulsion force of the anastomotic tissue under different output powers (120 W, 140 W, 160 W) and different welding times (6 s, 8 s, 10 s); (B) The burst pressure of the anastomotic tissue at two output powers (140 W, 160 W) in 8-second welding time (***indicates a p value less than 0.001, indicating an extremely significant difference between the two sets of data).

as the experimental electrode. The results of the tear-off force are shown in **Figure 7A**. The tear-off force initially increased and then decreased as welding time extends, across all three output power levels. Notably, at an output power of 120 W and a welding time of 6 seconds, the tear-off force reached its minimum value of 3.64±0.67 N, suggesting that the anastomosis may fail under lower output power and shorter welding durations. In contrast, at an output power of 160 W and a welding time of 8 seconds, the tear-off force reached its maximum value of 9.87±0.83 N. The results of the Student's t-test indicated no significant difference in the tear-off force at output powers of 140 W and 160 W after 8 seconds of welding (P=0.38). Therefore, further burst pressure experiments would be conducted to determine the optimal output power for welding parameters.

Intestinal tissue welding experiments were conducted at two output power levels, and the burst pressure results are shown in **Figure 7B**. The welding time was fixed at 8 seconds. At an output power of 140 W, the burstpressure was

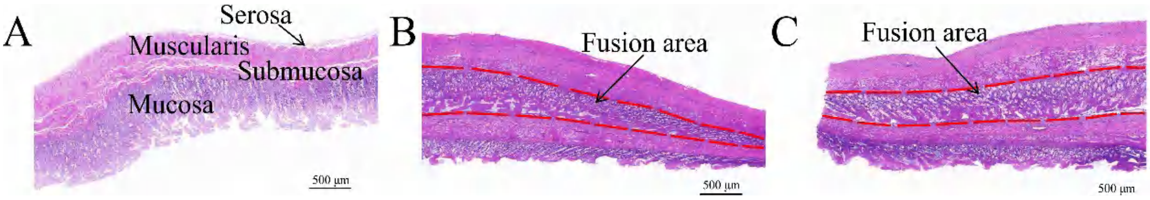

Figure 8. Histopathological examination of the anastomotic area. (A) Normal intestinal tissue; (B) Anastomosis area at 140 W power; (C) Anastomosis area at 160 W power.

143.31±5.02 mmHg, while at 160 W, the burst pressure increased to 222.88±13.48 mmHg. Clinically, the highest intra-abdominal pressure typically ranges from 100 to 150 mmHg [25]. The results indicate that only at an output power of 160 W did the burst pressure exceed the maximum intra-abdominal pressure. Therefore, an output power of 160 W and a welding time of 8 seconds were selected as the optimal welding parameters.

Histopathological examination

Figure 8 presents histopathological images of normal intestinal tissue and the anastomosis site under two magnifications, with a compression force of 20 N and a welding time of 8 seconds. The distinct separation of the serosa, muscular layer, submucosa, and mucosa was clearly visible in normal intestinal tissue. In contrast, the anastomosis area following welding exhibited a reduced thickness of the two intestinal layers, with a tightly fused connection, suggesting enhanced tissue union under the applied welding conditions. At an output power of 140 W, the anastomosis area displayed an uneven structure, with regions ranging from loose to dense, increasing the likelihood of leakage under the peristaltic forces of the intestine. However, at an output power of 160 W, the anastomosis demonstrated a more uniform thickness with a stable and secure connection, indicating more reliable tissue fusion.

Discussion

Colorectal cancer is a common malignancy of the digestive tract. Clinically, after surgical resection, the remaining tissue is typically reconnected using manual suturing or stapler anastomosis. However, both methods are associated with complications such as bleeding and anastomotic fistula formation. To address these challenges, tissue welding technology utilizing radiofrequency energy has been proposed as an innovative approach for tissue anastomosis. This technique leverages the thermal effects on tissue to achieve rapid and secure anastomosis without the need for foreign materials, offering distinct advantages over traditional methods.

Biodegradable magnesium alloys present a novel approach to tissue welding electrode design. Unlike traditional materials, magnesium alloy electrodes do not require removal through secondary surgery after completing tissue anastomosis, minimizing tissue damage. Mao et al. developed welding electrode structures using magnesium alloys, demonstrating improved welding strength while maintaining safety [15]. However, their study did not investigate the effects of electrode weight and mechanical support in depth. Therefore, this study focuses on electrode thickness and explores the potential for weight reduction while preserving mechanical strength.

First, mechanical simulations were conducted on the three types of circular electrodes. The results indicated that, under a force of 20 N, both the stress and strain experienced by the electrodes gradually decreased with increasing thickness. This suggests that a greater thickness reduces the likelihood of plastic deformation and stress concentration. Conversely, if the electrode is too thin, it may fail to provide effective support, potentially leading to anastomosis failure. Therefore, it is essential to identify a thickness that balances mechanical requirements with the need to reduce electrode weight based on material characteristics.

In our study, the maximum deformation of the T3 electrode was measured at 0.23194 mm, with a corresponding maximum strain of 1.2% and maximum stress of 122.26 MPa. These values fell within the elongation and yield strength range of WE43 magnesium alloy, indicating that this electrode meets the mechanical requirements for operational use. In contrast, the other two electrodes exceeded the material's yield strength, posing a risk of plastic deformation. Thus, an optimal thickness of 0.4 mm was selected for the electrodes.

Finite element analysis was conducted to examine the temperature distribution and thermal damage of the anastomotic tissue at three different power levels: 120 W, 140 W, and 160 W. The results showed that the minimum average maximum temperature of the tissue was 65.1 °C, while the maximum was 69.6 °C. The minimum average maximum thermal damage was 48.6%, and the maximum was 53.3%. These findings indicate that, under the same mechanical pressure and welding time, increasing power has a minimal effect on the average thermal damage to the tissue. The temperature differences observed at key points, labeled a and b, may be attributed to their positions relative to the welding area. Point a is located within the welding area, where the welding power directly influences the region, causing a rapid temperature increase. In contrast, point b is situated outside the welding area, where heat is transmitted through the electrode, leading to heat dissipation. As a result, the temperature increase at point b lags behind that at point a, and the temperature remains lower.

Mechanical pressure, output power, and welding time collectively influence the effectiveness of anastomosis. Research indicates that a pressure of 20 N is acceptable for tissue during welding. However, due to variations in electrode structure and materials, it is crucial to determine the optimal welding parameters, including output power and welding time, in this study. During normal intestinal function, peristalsis occurs. If the anastomotic tissue is not adequately adhered, there is a risk of anastomotic leakage. Effective anastomosis can only be achieved if it can withstand intestinal peristalsis.

Common methods for evaluating welding effectiveness include the avulsion force test and burst pressure test. The welding outcome is assessed by comparing the maximum tensile force at which the anastomosis fails during stretching with the maximum pressure at which leakage occurs during perfusion. Generally, an avulsion force exceeding 6 N and a burst pressure greater than 30 mmHg are considered necessary for successful anastomosis [26]. In our study, with an output power of 160 W and a welding time of 8 seconds, the avulsion force reached a maximum of 9.87±0.83 N, and the burst pressure was recorded at 222.88±13.48 mmHg. Additionally, histopathological examination revealed a uniform thickness of the anastomotic area with a stable connection, which adequately met the mechanical requirements for the intestine under normal physiological conditions.

In conclusion, we designed three different thicknesses of circular electrodes to reduce the electrode weight. Finite element analysis revealed that a thickness of 0.4 mm satisfies the mechanical requirements for the welding process. In vitro tissue welding experiments, including tearing force, burst pressure tests, and tissue pathology assessments, were conducted to evaluate the performance of the electrodes. The results demonstrated that the optimal welding parameters were 8 seconds of welding time and 160 W of output power, yielding an average tearing force of 9.87±0.83 N and an average burst pressure of 222.88±13.48 mmHg.

We have investigated the optimal electrode thickness from a mechanical perspective. However, the in vivo corrosion behavior of magnesium alloy-based implanted electrodes requires further experimental investigation. Additional research is needed before these electrodes can be fully considered for clinical application.

Author contributions: Lin Mao and Juxiao Wang conceived this project. Lin Mao and Juxiao Wang were responsible for the structural design and finite element simulation. Lin Mao and Chengli Song designed the intestinal welding experiment and anastomotic strength testing experiment. Juxiao Wang and Weiwei Fan conducted the experiments, collected relevant data, and performed the analysis. All authors contributed to the writing of the manuscript.

References

[1] Dekker E, Tanis PJ, Vleugels JLA, et al. Colorectal cancer. Lancet 2019;394(10207):1467–1480.

[2] Zhou H, Wang W, Luo P, et al. Trend of Colorectal Cancer Burden in China from 1990 to 2019. Cancer Res Prev Treat 2024;51(2):115–120.

[3] Akgül Ö, Çetinkaya E, Ersöz Ş, et al. Role of surgery in colorectal cancer liver metastases. World J Gastroenterol 2014;20(20):6113–6122.

[4] Breitenstein S, Rickenbacher A, Berdajs D, et al. Systematic evaluation of surgical strategies for acute malignant left-sided colonic obstruction. Br J Surg 2007;94(12):1451–1460.

[5] Han S, Cai Z, Ning X, et al. Comparison of a New High-Frequency Electric Welding System for Intestinal Closure with Hand-Sewn In Vivo Pig Model. J Laparoendosc Adv Surg Tech A 2015;25(8):662–667.

[6] Kramer EA, Rentschler ME. Energy-Based Tissue Fusion for Sutureless Closure: Applications, Mechanisms, and Potential for Functional Recovery. Annu Rev Biomed Eng 2018;20:1–20.

[7] Santini M, Fiorelli A, Messina G, et al. Use of the LigaSure device and the Stapler for

closure of the small bowel: a comparative ex vivo study. Surg Today 2013;43(7):787–793.
[8] Tu L, Zhou Y, Song C, et al. Preliminary study of a control algorithm for radio-frequency-induced intestinal tissue fusion. Int J Hyperthermia 2019;36(1):1297–1306.
[9] Wootten S, Zawacki ZE, Rheins L, et al. An evaluation of electrocoagulation and thermal diffusion following radiofrequency microneedling using an in vivo porcine skin model. J Cosmet Dermatol 2021;20(4):1133–1139.
[10] Elzayat S, Elsherif H, Aouf M. Trans-oral endoscopic assisted radio-frequency for adenoid ablation; A randomized prospective comparative clinical study. Auris Nasus Larynx 2021;48(4):710–717.
[11] Hu Z, Zong N, Song C, et al. Intestinal tissue fusion based on radiofrequency energy. J Med Biomech 2021;36:790-796.
[12] Holmer C, Winter H, Kröger M, et al. Bipolar radiofrequency-induced thermofusion of intestinal anastomoses--feasibility of a new anastomosis technique in porcine and rat colon. Langenbecks Arch Surg 2011;396(4):529-533.
[13] Zhao L, Song C, Wang Z, et al. Novel concave-convex electrode for colonic anastomoses by radiofrequency thermo-fusion. Surg Endosc 2015;29(7):1809-1816.
[14] Zong NX, Hu ZX, Xing XP, et al. Innovative Design and Experimental Study of Degradable Radiofrequency Energy Tissue Welding Electrodes. Model Sim 2022;11(2):454-464.
[15] Mao L, Han Z, Xing X, et al. Development of implantable electrode based on bioresorbable Mg alloy for tissue welding application. Sci Rep 2024;14(1):16110.
[16] Petter-Puchner AH, Fortelny RH, Walder N, et al. Small intestine submucosa (SIS) implants in experimental IPOM repair. J Surg Res 2010;161(2):264-271.
[17] Woźniak-Budych MJ, Staszak K, Staszak M. Copper and Copper-Based Nanoparticles in Medicine-Perspectives and Challenges. Molecules 2023;28(18):6687.
[18] Jiang HS, Zheng MY, Qiao XG, et al. Microstructure and mechanical properties of WE43 magnesium alloy fabricated by direct-chill casting. Mater Sci Eng: A 2017;684:158-164.
[19] Li S, Yang X, Hou J, et al. A review on thermal conductivity of magnesium and its alloys. J Magnes Alloys 2020;8(1):78-90.
[20] Eivani AR, Tabatabaei F, Khavandi AR, et al. The effect of addition of hardystonite on the strength, ductility and corrosion resistance of WE43 magnesium alloy. J Mater Res Technol 2021;13:1855-1865.
[21] Byun SH, Lim HK, Cheon KH, et al. Biodegradable magnesium alloy (WE43) in bone-fixation plate and screw. J Biomed Mater Res B Appl Biomater 2020;108(6):2505-2512.
[22] Xing X, Song C. A novel electrode to achieve balance between anastomotic strength and tissue thermal damage for radiofrequency-induced intestinal anastomosis. Acta Bioeng Biomech 2023;25:3-13.
[23] Arya S, Hadjievangelou N, Lei S, et al. Radiofrequency-induced small bowel thermofusion: an ex vivo study of intestinal seal adequacy using mechanical and imaging modalities. Surg Endosc 2013;27(9):3485-3496.
[24] Kubásek J, Dvorskỳ D, Čavojský M, et al. WE43 magnesium alloy – material for challenging applications. Met Mater 2019;57:159-165.
[25] Deprest J, Zheng F, Konstantinovic M, et al. The biology behind fascial defects and the use of implants in pelvic organ prolapse repair. Int Urogynecol J 2006;17(1):16-25.
[26] Xing X, Song C. A novel electrode for reducing tissue thermal damage in radiofrequency-induced intestinal anastomosis. Minim Invasive Ther Allied Technol 2024;33(2):80-89.

Progress in Medical Devices
ISSN: 2957-5478

Zentime

Review Article https://doi.org/10.61189/284918qpvynd

Measurement methods for positioning accuracy of multileaf collimators in radiation therapy: A mini review

Yuxi Fang[1], Rongguo Yan[1], Chunying Jiao[2], Yueling Li[2], Baolin Liu[1]

[1]School of Health Science and Engineering, University of Shanghai for Science and Technology, Shanghai 200093, China. [2]Beijing Institute of Medical Device Testing, Beijing 101111, China.

Corresponding author: Rongguo Yan.

Acknowledgement: This work was supported by the National Key Research and Development Program (2022YFC2409502).

Declaration of conflict of interest: None.

Received July 19, 2024; Accepted August 28, 2024; Published March 31, 2025

Highlights

- A comprehensive review of the structure, 3D and 2D views, operational principles, and major manufacturers of multileaf collimators (MLCs) used in radiation therapy.
- Introduction and comparison of three methods for evaluating the positioning accuracy of MLCs: dose film mea surement system, Matrixx ionization chamber array, and electronic field imaging system.

Abstract

Radiation therapy is a complex and high-precision technique that requires strict performance criteria for linear accelerators. One of the key factors influencing the quality of radiotherapy is the positioning accuracy of each leaf of the multileaf collimator. This mini-review discusses three commonly used dosimetry-based methods for evaluating multileaf collimator positioning accuracy: the dose film method, the Matrixx ionization chamber array method, and the electronic portal imaging device method. The review highlights the differences between these methods, showing that both the electronic portal imaging device and Matrixx methods offer higher measurement repeatability compared to the dose film method. However, the electronic portal imaging device method is more complex to implement than the Matrixx method.

Keywords: Positioning accuracy, multi leaf collimators, radiation therapy

Introduction

Radiation therapy has revolutionized cancer treatment by significantly increasing the radiation dose delivered to tumors while minimizing exposure to organs at risk, thereby improving tumor control rates. Achieving optimal outcomes in radiation therapy requires high-precision irradiation techniques and stringent performance standards for linear accelerators. A critical factor affecting the success of radiation therapy is the positioning accuracy of each leaf in the multileaf collimator (MLC) [1, 2].

An MLC is a beam-limiting device composed of multiple independent "leaves" made from high atomic number materials, typically tungsten. These leaves can move individually to shape and modulate the intensity of the radiation beam. MLCs are used in external beam radiotherapy to deliver conformal radiotherapy and intensity-modulated radiation therapy [3, 4]. Due to the high precision required in shaping the dose, as well as the dynamic changes in gantry speed and dose rate during intensity-modulated radiation therapy and volumetric

Address correspondence to: Rongguo Yan, School of Health Science and Engineering, University of Shanghai for Science and Technology, No.334, Jungong Road, Shanghai 200093, China. E-mail: yanrongguo@usst.edu.cn.

Table 1. Comparisons of the MLC performance across difference companies

Company	Type	Positioning Accuracy (mm)	Number of Leaves	Leaf Thickness (mm)	Field Size (mm×mm)
Varian Corp.	Millennium 120	±1	120	5	400×400
	HD 120	±1	120	2.5	220×400
	Halcyon	±1	114	10	280×280
Elekta Corp.	MLCi/MLCi2	±0.5	80	10	400×400
	Apex mMLC	±0.25	112	2.45	120×140
Siemens Corp.	MLC-82	±0.3	82	10	400×400
OUR United Corp.	TaiChi-120	±0.3	120	5	400×400

Note: MLC, multileaf collimator; HD, high definition.

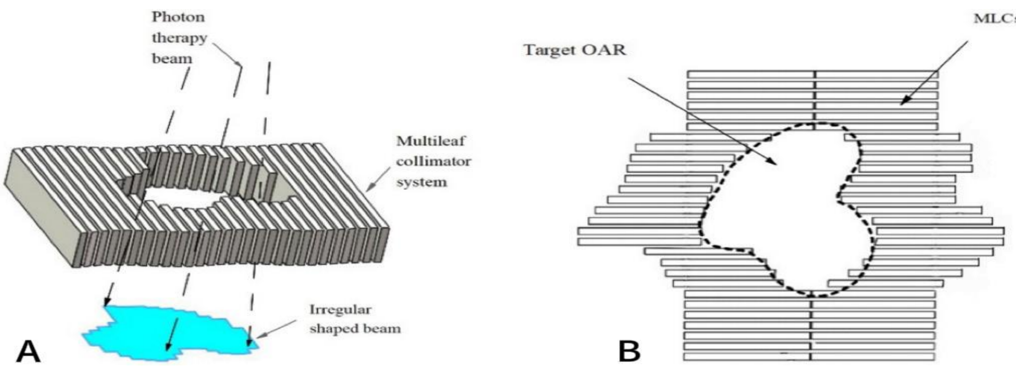

Figure 1. Principle of the MLCs. (A) 3D view of the MLCs; (B) 2D view of the MLCs. MLCs, multileaf collimators; OAR, organs at risk.

modulated arc therapy treatments, patient-specific pretreatment quality assurance is essential. Even minor deviations in MLC leaf positions can lead to significant inaccuracies in dose distribution, affecting the intended doses to the tumor and organs at risk [5-7]. For example, Rangel et al. reported that a 1 mm deviation in MLC leaf positioning could result in dose differences of up to 5.6% in the equivalent uniform dose for clinical target volumes in head and neck cancer treatment plans [7].

The MLC is primarily composed of multiple leaf pairs, as illustrated in **Figure 1**, with a 3D view in **Figure 1A** and a 2D view in **Figure 1B**. The position of the MLC leaves is adjusted based on the target area, allowing the radiation beam to be shaped according to the projection of the target on the irradiation plane. In practical applications, the leaves are driven by micromotors, which convert rotational motion into linear leaf movement through a screw mechanism. To ensure accurate leaf positioning, the speed, acceleration, and number of rotations or steps of the driving motors are precisely controlled, often using an encoder to monitor and regulate each motor's movement [8, 9].

Leading manufacturers of radiation therapy equipment include Varian, known for its advanced radiation therapy solutions [8, 9]; Elekta, which offers versatile linear accelerators with artificial intelligence (AI)-enhanced imaging and adaptive capabilities [10]; and Siemens, which has developed systems to aid in radiation therapy planning. OUR United Corporation, a specialized company based in Xi'an, China, focuses on the research, development, production, and service of innovative technologies and equipment for tumor radiotherapy [11-15]. **Table 1** compares the MLC performance metrics, including positioning accuracy, number of leaves, leaf thickness, and field size, across different manufacturers [11-15].

Currently, there are three primary dosimetry-based methods for detecting MLC positioning accuracy: the dose film measurement system, the MatriXX ionization chamber array, and the electronic portal imaging device (EPID) [16, 17].

Primary dosimetry-based methods

Dose film measurement system

This method utilizes Kodak X-OMAT V film, which is enclosed in an opaque envelope and processed using an automatic film processor. The film is scanned with a VIDAR DosimetryPro Advantage film scanner, and data is analyzed using RIT113 film analysis software. **Figure 2** illustrates the solid water phantom used for radiotherapy validation. Constructed from poly-

Table 2. Coordinates of reference leaves in place (mm)

Measurement method	50×200		100×200		150×200		200×200	
	X1	X2	X1	X2	X1	X2	X1	X2
Dose film	24.6	25.3	49.5	50.3	74.9	75.3	99.5	100.3
MatriXX	24.3	25.4	49.4	50.5	74.6	75.7	99.8	100.6
EPID	24.8	25.3	49.7	50.3	74.7	75.3	99.2	99.9
Maximum difference	0.5	0.1	0.3	0.2	0.3	0.4	0.6	0.7
Mean and standard deviation	0.39±0.20							

Note: EPID, electronic portal imaging device.

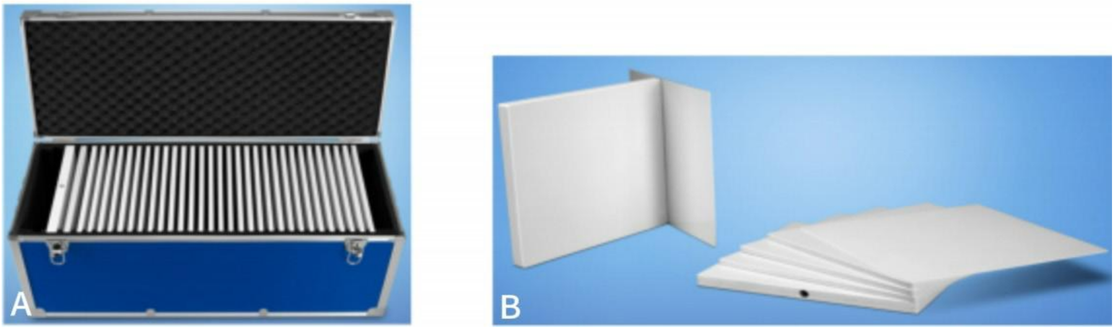

Figure 2. Delta instruments radiotherapy verification solid water phantom SRT-033. (A) Solid water phantom in a test chamber; (B) Layers view with different thickness. This figure is cited from [18].

styrene, the phantom measurs 300 mm × 300 mm, and consists of 29 layers of 10 mm thickness, along with one layer of 5 mm thickness, two layers of 2 mm thickness, and one layer of 1 mm thickness. To perform optical density calibration with this method, follow these steps [18]:

(1) Set the source-to-skin distance to 100 cm and place a 2 cm thick solid water phantom on the film. Set the irradiation field to 4 cm × 4 cm.

(2) Expose the film to 8 different dose fields at various positions. Record the average optical density for each field center.

(3) Use segmented polynomial fitting software to establish a dose-response curve from these recordings. Draw a crosshair at the geometric center of the film before exposure and align it with the light field to determine the field center.

(4) Create leaf position templates for the four fields mentioned above in the RIT113 software. Input the processed validation films into RIT113 using the DosimetryPro Advantage film scanner.

(5) Utilize the established template file to analyze the accuracy of each picket position by measuring the center position of the 51% dose line between each pair of pickets.

MatriXX ionization chamber array

The MatriXX ionization chamber array from IBA, Germany, is used for this method, as shown in **Figure 3**. Each chamber is factory-calibrated to ensure consistent measurement results. IBA's OmniPro I'mRT software is used for data collection and analysis of accelerator field dose data [18]. The procedure for this method involves the following steps [18]:

(1) Position the MatriXX array horizontally under the accelerator and align its effective measurement surface with the isocenter plane using a laser lamp. Place a 2 cm thick solid water phantom on the isocenter plane.

(2) Open the accelerator beam to a 25 cm × 25 cm field size and preheat the MatriXX array with continuous beam output, monitoring for consistent response from each chamber

(3) Once preheated, collect four field shapes using the Movie mode. Use the Multiple Row Analysis function in OmniPro I'mRT software, a user-friendly application for comprehensive plan verification and quality assurance of intensity-modulated radiation therapy, IGRT, and rotational treatments. Analyze the positioning accuracy of each pair of pickets, applying the Fermat interpolation algorithm to accurately detect the edges of the radiation field.

Figure 3. IBA MatriXX 2D Array.

Figure 4. The Elekta Synergy Linear Accelerator.

Figure 5. Graphical user interface of AutoCAL software.

Electronic field imaging system

This method employed the electronic field imaging system, known as IView GT, developed by Elekta — a global Swedish company specializing in radiation therapy and radiosurgery equipment, as well as clinical management for treating cancer and brain disorders [19-21].

The IView GT system consists of an amorphous silicon detector array with an effective imaging area of 26 cm × 26 cm at the isocenter. The measurement range can be extended through electronic translation in the G-T (gantry-tilt) and A-B (anterior-posterior) directions of the accelerator. It supports energy levels from 4 to 20 MV and a dose rate range of 50 to 600 MU/min [19-21]. Data collection and analysis are conducted using IBA's AutoCAL software (Ion Beam Applications) [19-21]. **Figure 4** shows the IView GT amorphous silicon detector panel, and **Figure 5** displays the AutoCAL software interface. The following steps should be performed according to AutoCAL software requirements before measurement:

(1) Align the small machine head of the accelerator parallel to the detection panel.

(2) Calibrate the pixel size of the IView GT detector panel.

(3) Set a radiation center as a reference point for measuring absolute dimensions.

(4) Align the machine center, represented by the crosshairs of the small machine head, with the radiation center.

After completing these steps, the AutoCAL software's Size Test function could be used to collect data from four fields for analysis.

Discussion

Table 1 presents the measurement results for a pair of leaves of the same accelerator at different positions using the three measurement methods. The maximum difference in results among these methods is less than 1 mm. The measurement outcomes for all other leaves are consistent with **Table 2**, and the maximum difference for each group of leaves across different field sizes is also less than 1 mm. This indicates that all three methods can effectively perform quality assurance testing on the MLCs of the same accelerator, with largely consistent results. Generally, the dose film measurement system exhibits lower measurement repeatability, while the MatriXX ionization chamber array and the electronic field imaging system demonstrate higher repeatability.

The positioning accuracy of MLCs is a critical factor influencing the success of radiotherapy. High-performance standards for accelerators are essential for the precise and complex irradiation procedures required in radiation therapy.

Conclusion

This paper provides a brief review of three commonly used dosimetry-based methods for detecting MLC positioning accuracy: the dose film measurement system, the MatriXX ionization chamber array, and the EPID. Among these, the EPID and the MatriXX ionization chamber array offer higher measurement repeatability compared to the dose film measurement system. However, the EPID is more complex to set up and requires more sophisticated software than the MatriXX ionization chamber array.

Author contributions: Yuxi Fang searched related articles, created the figure of the principle of the MLCs, and wrote the mini review. Rongguo Yan provided writing ideas and guided the writing. Chunying Jiao and Yueling Li contributed in giving knowledge of measurement methods for the positioning accuracy of multi leaf collimators in radiation therapy, and providing literatures. Baolin Liu helped in proofreading the paper.

References

[1] Ceylan C, Yondem Inal S, Senol E, et al. Effect of Multileaf Collimator Leaf Position Error Determined by Picket Fence Test on Gamma Index Value in Patient-Specific Quality Assurance of Volumetric-Modulated Arc Therapy Plans. Cureus 2021;13(1):e12684.

[2] Boudet J, Aubignac L, Beneux A, et al. Evaluation of QA software system analysis for the static picket fence test. J Appl Clin Med Phys 2022;23(7):e13618.

[3] Rahmat Y, Pawiro SA, Baihaqi YA, et al. Position accuracy evaluation of multileaf collimator (MLC) static in linear accelerator. IOP Conf Ser: Mater Sci Eng 2018;432(1):012052.

[4] Kasmayanti Sakaria, Nur Shaheera Midi, Hafiz M Zin. Picket fence test of Agility MLCs using linac log data. IOP Conference Series: Journal of Physics: Conference Series 2019;1248:012054.

[5] LoSasso T, Chui CS, Ling CC. Comprehensive quality assurance for the delivery of intensity modulated radiotherapy with a multileaf collimator used in the dynamic mode. Med Phys 2001;28(11):2209-2219.

[6] Cadman P, Bassalow R, Sidhu NP, et al. Dosimetric considerations for validation of a sequential IMRT process with a commercial treatment planning system. Phys Med Biol 2002;47(16):3001-3010.

[7] Rangel A, Dunscombe P. Tolerances on MLC leaf position accuracy for IMRT delivery with a dynamic MLC. Med Phys 2009;36(7):3304-3309.

[8] El-Maraghy KA, Metwaly M, Mahmoud El-Sayed E-S, et al. A quality assurance technique for the static multileaf collimator mode based on intrinsic base lines. J Radiat Res Appl Sci 2014;7(2):230-240.

[9] Morrow A, Trisnadi N, Chung H. Multi-level multi-leaf collimators: Optimization of layer thicknesses and a feasibility study. Med Phys 2022;49(2):792-800.

[10] Sivabhaskar S, Li R, Roy A, et al. Machine learning models to predict the delivered positions of Elekta multileaf collimator leaves for volumetric modulated arc therapy. J Appl Clin Med Phys 2022;23(8):e13667.

[11] Lv J, Chen LL, Wen RL, et al. Structural design and penumbra analysis of dynamic multi-leaf collimator leaf end. Chin J Med Instrum 2023;47(4):377-382.

[12] Guo Z. Technical status and development trend of dynamic multileaf grating collimator, China Med Devices 2021;36(01):154-158.

[13] Zhang MM. Research of multi-leaf collimator. Mod Instrum Med Treat 2023;29(3):66-72.

[14] Gao DD, Wang JZ, Luo J, et al. QA digital analysis system for radiotherapy based on Pylinac library. Comput Syst Appl 2021;30(7):95-101.

[15] Liu SP, Ma YG, Guo YX. Evaluation on the stability of positioning precision of the leaves of accelerator MLC under different gantry angles. China Med Equip 2023;20(12):33-36.

[16] Li Y, Chen L, Zhu J, et al. A quantitative method to the analysis of MLC leaf position and speed based on EPID and EBT3 film for dynamic IMRT treatment with different types of MLC. J Appl Clin Med Phys 2017;18(4):106-115.

[17] Antypas C, Floros I, Rouchota M, et al. MLC positional accuracy evaluation through the Picket Fence test on EBT2 films and a 3D volumetric phantom. J Appl Clin Med Phys 2015;16(2):5185.

[18] Guo F. Application of Matrixx Evolution in Intensity Modulated Dose Verification of Domestic UIH Accelerator. Adv Clin Med 2024;14(3):1710-1716.

[19] Christophides D, Davies A, Fleckney M. Automatic detection of MLC relative position errors for VMAT using the EPID-based picket fence test. Phys Med Biol 2016;61(23):8340-8359.

[20] Kalavagunta C, Xu H, Zhang B, et al. Is a weekly qualitative picket fence test sufficient? A proposed alternate EPID-based weekly MLC QA program. J Appl Clin Med Phys 2022;23(8):e13699.

[21] Zhang X, Liu M. Research on the position precision of the leaves of M LC based on fuzzy-PID. Manuf Autom 2013;35(8):30-32.

Progress in Medical Devices
ISSN: 2957-5478

Zentime

Review Article https://doi.org/10.61189/273582nrnxmc

Research advances of beamforming algorithms in medical ultrasound systems

Fei Liu[1], Haipo Cui[1], Fujia Sun[2], Shuhao Hou[3], Peng Yue[4]

Schools of [1]Health Science and Engineering, [2]Mechanical Engineering, [3]Materials and Chemistry, University of Shanghai for Science and Technology, Shanghai 200093, China. [4]Shanghai Guoyan Medical Device Testing Center Co., Ltd., Shanghai 200000, China.

Corresponding authors: Haipo Cui and Fujia Sun.

Declaration of conflict of interest: None.

Received August 12, 2024; Accepted September 11, 2024; Published March 31, 2025

Highlights

- Algorithms such as adaptive beamforming and synthetic aperture technology have significantly improved the quality of ultrasound images.
- New algorithms, such as deep learning, can adapt to more complex signal environments at the expense of real-time performance.
- Combining different algorithms can overcome the limitations of a single algorithm, thereby improving image resolution, contrast, and noise resistance.

Abstract

Medical ultrasound imaging, as a non-invasive, safe, and reliable technology, plays an important role in clinical diagnosis and treatment. However, traditional ultrasound imaging techniques have limitations such as low resolution, poor penetration depth, and high noise levels. To address these issues, beamforming algorithms have become essential. This paper discusses the development and current research status of beamforming algorithms in the context of medical ultrasound systems, focusing on commonly used beamforming algorithms such as synthetic aperture imaging, adaptive beamforming (especially minimum variance distortionless response), and generalized sidelobe canceller technology. These algorithms optimize the emission and reception of ultrasound waves, overcoming the limitations of traditional techniques and improving image resolution, penetration depth, and noise suppression. They provide support for the advancement of medical ultrasound imaging technology and its clinical applications.

Keywords: Medical ultrasound imaging, beamforming algorithms, synthetic aperture, minimum variance, generalized sidelobe canceller

Introduction

Since its inception in the mid-20th century, medical ultrasound imaging technology has undergone continuous innovation and development, becoming an indispensable tool in modern medical diagnosis and treatment. Introduced in the 1950s, ultrasound technology primarily featured A-mode and B-mode ultrasound. A-mode ultrasound (Amplitude Mode) was mainly used to measure the distance of tissue interfaces, generating one-dimensional amplitude images, while B-mode ultrasound (Brightness Mode) produced two-dimensional grayscale images through brightness modulation, providing a more intuitive display of tissue structures. Although these early technologies had relatively low image quality and resolution, they marked the initial application and development of medical ultrasound imaging technology [1].

With advancements in electronic and computer technologies, real-time two-dimensional ultrasound (2D Ultrasound) gained popularity between the late 1960s to the 1970s. This technology, by utilizing mechanical or electronic scanning probes to generate and display real-time two-dimensional images of the human body, greatly improved the efficiency and diag-

Address correspondence to: Haipo Cui, School of Health Science and Engineering, University of Shanghai for Science and Technology, NO.334, Jungong Road, Shanghai 200093, China. Tel: +86-21-55271290, E-mail: hpcui@usst.edu.cn; **Fujia Sun**, School of Mechanical Engineering, University of Shanghai for Science and Technology, NO.516, Jungong Road, Shanghai 200093, China. Tel: +86-13621773624, E-mail: chinasfj@126.com.

Table 1. Characteristics of ultrasound waves of different frequencies and their application

	Frequency (MHZ)	Characteristics	Applications
Low-frequency ultrasound	2-5	Capable of penetrating deeper tissues, suitable for observing deeper structures.	Liver, pancreas, heart, etc.
Mid-frequency ultrasound	5-12	Has higher resolution, suitable for observing structures at moderate depths.	Digestive tract, kidneys, bladder, etc.
High-frequency ultrasound	12-20	High-frequency ultrasound has higher resolution, suitable for observing superficial structures.	Breast, thyroid, ocular structures, etc.

nostic capabilities of ultrasound examinations [2]. It became widely applied in abdominal, cardiac, and obstetric examinations. Since then, medical ultrasound imaging technology has become a focal point of research. Technologies such as three-dimensional ultrasound, harmonic imaging, and endoscopic ultrasound have continued to evolve. These advancements have significantly improved the accuracy and efficiency of clinical diagnosis while expanding the application scope of ultrasound in disease diagnosis, treatment, and prognosis evaluation, solidifying its critical role in modern medicine.

To achieve high-quality ultrasound imaging, there is a growing demand for advanced ultrasound beamforming algorithms. The conventional Delay-and-Sum (DAS) Beamforming algorithm aligns the phases of signals from specific directions by applying delays and weights to signals received by each antenna, thereby enhancing signals from those directions. While this method is simple and computationally efficient, it has limited ability to suppress sidelobes and cannot effectively filter out interference signals from other directions [3]. The Dynamic Receive Focus algorithm, which fixes the transmission focus and overlays delayed ultrasound echo signals to obtain images, provides higher resolution and contrast near the transmission sound field focus, but results in overall lower quality ultrasound images [4]. The Synthetic Aperture (SA) beamforming algorithm, proposed by the team led by Professor Jensen at the Fast Ultrasound Imaging Center of the Technical University of Denmark, improves ultrasound image quality by sequentially excites individual array elements for wave transmission and allowing all array elements to receive the signals. This bidirectional focus of both transmission and reception, achieved through time-of-flight calculations, significantly enhances image clarity [5]. The Minimum Variance (MV) beamforming algorithm, proposed by Capon, constructs the weights of each channel in the phased array ultrasound endoscope from a signal processing perspective. It maintains an ideal signal while suppressing the total output signal energy, thereby improving image quality [6]. Nilsen's diagonal loading algorithm and subarray smoothing algorithm further enhance the robustness of the MV algorithm [7].

Domestic researchers have also conducted in-depth research on ultrasound imaging algorithms. Li et al. applied graphics processing unit parallel computing to the SA algorithm, solving the issues of computational complexity and large data demands, which improved imaging speed [8]. Su Ting et al. proposed the multi-line acquisition delay multiply and sum algorithm, which reduces the correlation between echo signals by combining and multiplying them using the MV approach [9]. Wang et al. proposed a MV algorithm that combines signal-to-noise ratio post-filtering and feature space fusion, leading to enhanced resolution and contrast compared to the traditional MV algorithm, with improved adaptability to noise [10].

Through domestic and international research, it is evident that classic beamforming algorithms such as DAS, MV, SA, and Generalized Sidelobe Canceller (GSC) remain essential in medical ultrasound imaging. This paper reviews the research progress on beamforming algorithms in the field of medical ultrasound. The second section introduces the basic principles and technical characteristics of ultrasound beamforming, including the generation, propagation, and reflection mechanisms of ultrasound waves. The third section briefly describes the literature retrieval process and summarizes the main content and conclusions of the reviewed literature. The fourth section introduces more classical beamforming algorithms and related technologies in existing research. The final section summarizes the main trends and challenges in current research on ultrasound endoscopic image processing and proposes future research directions.

The basic principle of endoscopic ultrasound

The acoustic principles and propagation characteristics of ultrasound are the foundation of ultrasound imaging. Ultrasound is a type of mechanical wave with a frequency higher than the

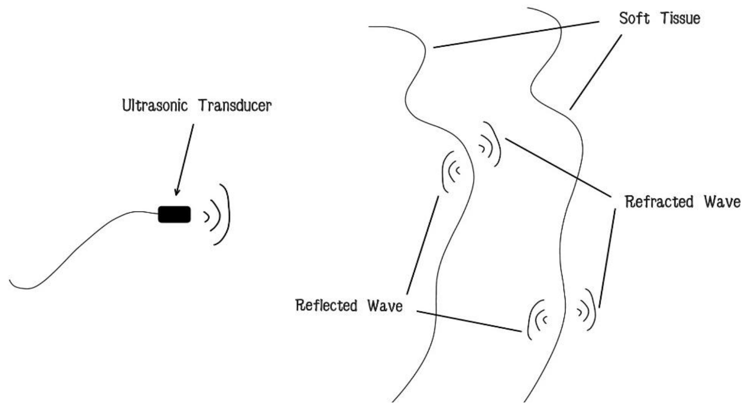

Figure 1. Reflection, refraction, and echo signal illustration.

human hearing range, typically above 20 kHz. The higher the frequency, the shorter the wavelength, enabling higher-resolution imaging. In medical ultrasound systems, the vibration frequency of sound sources generally ranges from 2 to 20 MHz. **Table 1** summarizes the various medical applications of these ultrasonic waves at different frequencies.

Ultrasound waves are emitted through an ultrasound probe or transducer, which contains one or more piezoelectric crystals that convert electrical energy into mechanical vibrations, producing the ultrasound waves. As these waves propagate through the body, they interact with different tissues, each of which has unique acoustic properties. At the boundaries between different soft tissues, the waves reflect and refract. When ultrasound waves encounter these tissue boundaries, part of the energy is reflected back, forming echoes. The piezoelectric crystals in the ultrasound probe convert the received echo signals into analog electrical signals, as illustrated in **Figure 1**.

These signals undergo a series of processing steps, including amplification, gain compensation, filtering, analog-to-digital conversion, and demodulation, before being sent to the display. During these steps, advanced image processing algorithms and techniques, such as noise reduction algorithms, image enhancement techniques, motion correction algorithms, and deep learning methods, are applied to improve the quality and accuracy of ultrasound images. The beamforming algorithms play a crucial role in the reception of reflected signals. During this process, the beamforming algorithm adjusts the transmission and reception time delays, as well as the phase and amplitude of multiple transducer elements in the ultrasound probe. By doing so, it optimizes the direction, focus, and shape of the ultrasound beam, thereby enhancing the resolution, contrast, and depth of the images.

Literature research

We conducted a literature search using keywords such as “medical ultrasound imaging” and “beamforming algorithms” across platforms like Google Scholar, Web of Science, and PubMed.

After thoroughly reviewing and categorizing a large number of papers, we selected over one hundred papers related to beamforming algorithms, including DAS, SA, MV, Regularization, and GSC. Among these, more than ninety papers were published within the last fifteen years. We summarized and classified nearly one hundred papers from 2009 onwards, selecting over thirty representative studies for in-depth discussion. **Table 2** summarizes the main content and research conclusions of these studies.

Synthetic aperture ultrasonography (SAUS)

SA technology was initially utilized for radar technology. SA Radar collects radar signals from a moving platform and utilizes signal processing techniques to simulate a large antenna aperture. SA Radar systems achieve high-resolution imaging by synthesizing a large aperture through motion. SA algorithms process the collected radar signals to generate high-resolution images. SA Radar finds extensive applications in various fields such as military, geological exploration, and environmental monitoring [41, 42].

Inspired by high-resolution imaging used in radar and optics, Professor Jørgen’s team at the Technical University of Denmark improved the SA algorithm and introduced it into medical ultrasound imaging. The specific steps of SA algorithm include data acquisition, motion compensation, data focusing, image processing, image enhancement, and post-processing. During the data acquisition stage, signal data are collected from different positions or directions. Subsequently, motion compensation is applied to correct for any platform or sensor movement during data collection. Next, the collected data is focused using signal processing techniques to concentrate signals from different positions or directions onto a single focal point. Finally, this focused data are used to generate high-resolution images, which can be further enhanced and post-processed to meet specific

Table 2. Summary of literature

Authors	Main content	Research conclusions
Chen et al. [11]	A SAF Method to Improve Signal-to-Noise Ratio and Resolution in Endoscopic Ultrasound.	Compared to traditional methods, this approach can improve the signal-to-noise ratio and resolution of ultrasound images by 9.38 dB and 51%, respectively.
Trots et al. [12]	STA Method Combined with Golay Coded Transmission.	While maintaining the resolution of ultrasound images, this method improves the signal-to-noise ratio and increases the imaging depth.
Chen et al. [13]	A Low-Complexity Global Motion Compensation Algorithm Based on the STA Method.	Compared to uncompensated images, the proposed motion compensation algorithm can improve the image CR and CNR by 13.73 dB and 2.04 dB, respectively.
Tasinkevych et al. [14]	Optimization of the MSTA ultrasound imaging method.	The optimal transmit aperture size provides balance between lateral resolution and penetration depth in the obtained two-dimensional ultrasound images, while maintaining a high frame rate.
Zhou et al. [15]	SASB Algorithm Based on Chirp Coded Excitation.	It achieves range-independent resolution while significantly reducing the size of front-end data, attaining imaging quality comparable to baseline 3D SASB.
Mirzaei et al. [16]	VSSA Imaging ultrasound imaging technology.	It overcomes the depth of field limitations of traditional source synthetic aperture imaging, offering significant advantages in high resolution, high A-line count, and penetration depth, and it can significantly improve the accuracy of lateral strain estimation.
Synnevag et al. [17]	An adaptive method with a Minimum Variance beamformer.	The Minimum Variance beamformer can compensate for resolution loss by using smaller transducers, wider transmission beams, or lower transmission frequencies.
Sreejeesh et al. [18]	Quadrature Rotation Decomposition-MVDR Beamforming Algorithm.	By solving the problem of high computational complexity of the MVDR algorithm, it has an advantage in terms of computation time and can be used for ultra-fast adaptive beamforming applications.
Holfort et al. [19]	A MV Method for Near-field Broadband Data Beamforming.	The Frequency Subband MV significantly improves the lateral resolution and contrast of imaging while reducing the number of transmissions, and it exhibits good tolerance to pointing vector errors.
Yan et al. [20]	MV based on Submatrix Space Coherence with the Sign Coherence Factor.	This method reduces sidelobe noise without increasing computational complexity and significantly improves the resolution and contrast of imaging in coherent plane-wave compounding.
Wang et al. [21]	CMSAW.	CMSAW introduces aperture coherence-based adaptive diagonal loading to enhance speckle preservation performance. CMSAW-MV improves resolution and suppresses sidelobes, incoherent clutter, and noise.
Aliabadi et al. [22]	OESMV.	This new signal-to-noise subspace identification method allows for flexible adjustment based on specific imaging needs to achieve optimal imaging results, significantly improving aspects such as image resolution, contrast, and grayscale levels.
Li et al. [23]	An eigen-based GSC.	This method can reduce sidelobe levels and improve contrast. It offers better lateral resolution and contrast compared to non-adaptive beamformers.
Li et al. [24]	A forward and backward generalized sidelobe canceller method for medical ultrasound imaging.	This method achieves good lateral resolution and contrast without the need for preprocessing algorithms. It can improve the imaging quality of medical ultrasound systems with lower computational overhead and higher reliability.
Yang et al. [25]	Cross Sub-aperture Averaging GSC.	Compared to DS, SA, and traditional GSC methods, GSC-CROSS improves lateral resolution by 76.9%, 68.8%, and 17.1% respectively.
Yang et al. [26]	A beamforming algorithm combining generalized sidelobe canceleation with feature space Wiener filtering.	Compared to DS and SA beamforming methods, this approach significantly improves the imaging quality of medical ultrasound systems in terms of lateral resolution and contrast.
Kumar et al. [27]	Deep learning-based algorithm to estimate inactive channel data in periodic sparse arrays.	The algorithm uses data from multiple active channels to estimate inactive channel data. This effectively reduces the element spacing in beamforming, thereby suppressing grating lobes, improving the image quality of sparse arrays.
Hyun et al. [28]	Neural network framework for beamforming ultrasound signals into speckle-reduced B-mode images.	This method demonstrates that networks trained in computer simulations can be generalized to actual in vivo imaging to produce images with significantly reduced speckle while preserving resolution.
Mamistvalov et al. [29]	Deep learning-based B-mode image reconstruction from temporally and spatially subsampled channel data.	The resolution is higher compared to previously proposed reconstruction methods from compressed data (such as NESTA), and comparable noise levels to DAS beamforming from fully sampled data.
Perdios et al. [30]	CNN-based image reconstruction combined with cross-correlation-based speckle tracking algorithm.	This method could unleash the full potential of ultrafast ultrasound, finding applications in areas such as ultrasensitive cardiovascular motion and flow analysis or shear wave elastography.

Authors	Main content	Research conclusions
Shin et al. [31]	MPAX based on Delay and Apodization Crosstalk.	The MPAX technique has been proven to be a highly effective method for suppressing reverberation clutter. This technique robustly suppresses near-field reverberation clutter, significantly enhancing the contrast of ultrasound images.
Nghia et al. [32]	A unified pixel-based beamforming algorithm adapting to the non-spherical waveform of the transmitted beam.	The unified pixel-based beamformer shows significant improvements in image quality compared to other delay-and-sum methods and demonstrates robust performance in limited in vivo studies.
Matrone et al. [33]	Short-Lag Focused F-DMAS formula to limit the signal lag time in the calculation of the coherence matrix used for beamformer formation.	The Short-Lag Focused F-DMAS formula controls the delay time of the signals involved in spatial coherence computation. This helps to maintain or enhance the performance of the F-DMAS algorithm while reducing computational complexity.
Dei et al. [34]	A CF weighting technique combined with ADMIRE.	The CF-weighted ADMIRE further improves image quality in certain aspects. The CF weighting used as a post-processing technique enhances contrast while reducing CNR and speckle SNR.
Rajamaki et al. [35]	Hybrid beamforming method using sparse arrays.	Combining sparse arrays with hybrid beamforming can significantly reduce the number of elements and front-end requirements to achieve the resolution of fully digital uniform arrays.
Ni et al. [36]	Simultaneous excitation of array elements with random sequences encoding, generating an unfocused ultrasound wavefront with random interference.	This method can enhance the detection of organ boundaries and aid in lesion localization in clinical applications such as abdominal and musculoskeletal imaging.
Goudarzi et al. [37]	A flexible beamforming framework using RED.	The RED algorithm provides the best image quality in terms of contrast metrics while preserving speckle statistics.
Asif et al. [38]	Sequential DAS method for focused transmission using fast-marching method.	This method helps overcome fat-induced signal distortion, thereby accurately imaging various pathologies in the liver and abdomen.
Guo et al. [39]	A pixel-based Delay Multiply and Sum beamforming with a Wiener filter.	Compared to traditional dynamic focusing, it has shown a significant improvement in lateral resolution. Compared to the conventional pixel-based algorithm, this method greatly enhances spatial resolution and contrast while maintaining the good characteristics of the beamformer.
Vayyeti et al. [40]	F-DowMAS nonlinear beamforming method.	By adaptively computing the optimal weights for each imaging point, F-DowMAS effectively enhances the resolution and contrast of the image while reducing noise and artifacts.

Note: SAF, Synthetic Aperture Focusing; STA, Synthetic Transmit Aperture; CR, contrast ratio; CNR, contrast-to-noise ratio; MSTA, Multi-Element Synthetic Transmit Aperture; SASB, Synthetic Aperture Sequential Beamforming; VSSA, Virtual Source Synthetic Aperture; MV, Minimum Variance; CMSAW, Covariance Matrix-based Adaptive Weighting; OESMV, Oblique Eigen-space Minimum Variance; GSC, Generalized Sidelobe Canceller; GSC-CROSS: Cross-Subarray Averaging GSC; DS, Delay-and-Sum; SA, Synthetic Aperture; CNN, Convolutional Neural Network; MPAX, Multi-Phase Apodization Crosstalk; F-DMAS, Filtered Delay Multiply and Sum; CF, coherence factor; ADMIRE, aperture domain model image reconstruction; RED, Regularization by Denoising; F-DowMAS, Filtered Delay Optimal Weighted Multiply and Sum.

requirements. The SA beamforming algorithm, illustrated in **Figure 2**, significantly improves imaging resolution and quality, holding important implications for medical diagnostics and other fields [5].

SAUS offers several advantages over traditional beamforming methods. Since it achieves fully dynamic focusing during both transmission and reception, SAUS offers higher spatial resolution. Additionally, since fewer components are needed to generate the waveform during each ultrasound pulse transmission, SAUS consumes less energy. These advantages have made SAUS a hot topic in beamforming algorithm research. Chen et al. proposed a SA Focusing (SAF) method to improve the signal-to-noise ratio (SNR) and resolution in ultrasound endoscopy. This technique leverages the rotational characteristics of the transducer probe, transmitting and receiving echoes at different times and positions during the rotational scan. By utilizing the coding and linear frequency modulation characteristics of the echoes, the algorithm develops axial and lateral matched filters to achieve compression in both directions [11]. Compared to traditional methods, SAF improves the SNR and resolution of ultrasound images by 9.38 dB and 51%, respectively. Therefore, it holds potential for future clinical and research applications. The Synthetic Transmit Aperture (STA) method provides fully dynamic focusing in both transmission and reception modes, offering the highest imaging quality. In the STA method, each array element sequentially emits pulses, while all elements receive echo signals. Data is acquired from multiple directions during transmission, and a complete image is reconstructed based on this data. The advantage of this method is that fully dynamic focusing can be applied during both transmission and reception, resulting in superior quality images. Trots and colleagues conducted theoretical and experimental studies on STA combined with Golay-coded

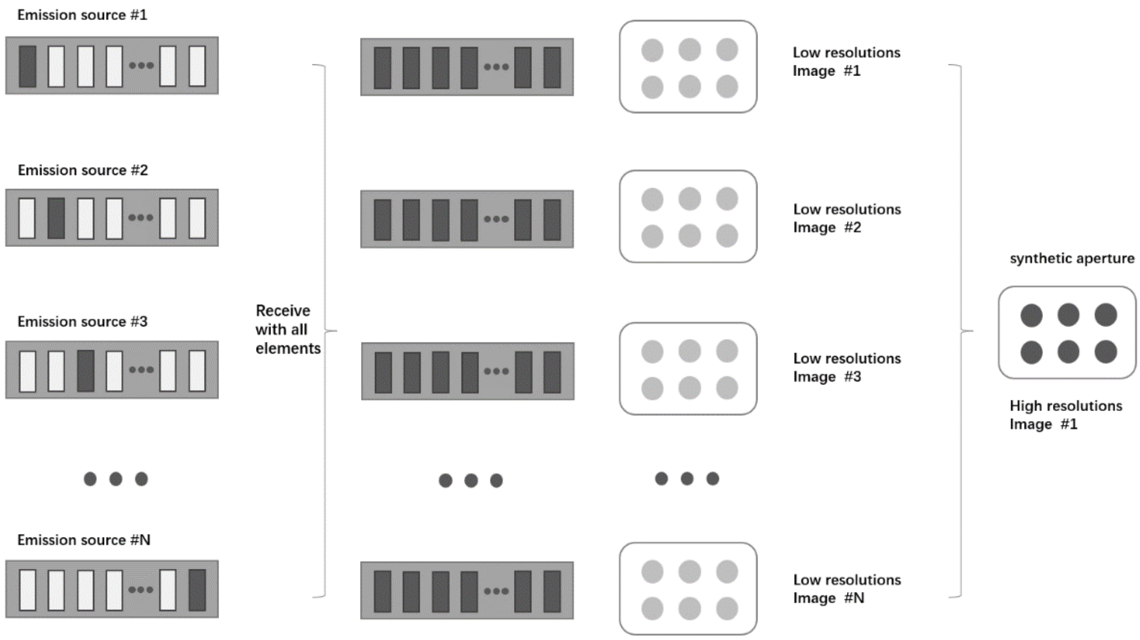

Figure 2. Development process of Synthetic Aperture beamforming algorithm.

transmission for medical ultrasound imaging [12]. The transmission of long waveforms with specific autocorrelation functions can increase the total energy of the transmission signal without increasing peak pressure. This enhances the SNR of the image and increases the display depth while maintaining ultrasound image resolution. Since high-resolution images in STA are formed by superimposing low-resolution images, they are susceptible to motion between transmissions. Chen et al. proposed a low-complexity global motion compensation algorithm, which uses common interest regions between different transmissions in STA imaging to form backward and forward beam vectors; By analyzing the relationship between specific beam vectors in STA imaging, this algorithm assesses the magnitude and direction of motion [13]. This motion compensation algorithm effectively reduces imaging blurring and distortion caused by motion, significantly improving the quality of the resulting high-resolution images. The low complexity of the algorithm makes it highly feasible and practical for real-world applications.

Compared to the traditional SA technology, the Multi-element Synthetic Transmit Aperture (MSTA) method effectively improves the frame rates of imaging systems while achieving a good balance between penetration depth and lateral resolution, making it one of the most promising methods in ultrasound imaging. Tasinkevych et al. optimized the MSTA method by identifying the ideal transmission aperture size that achieves the best balance between lateral resolution and penetration depth for 2D ultrasound images, all while maintaining a high frame rate [14].

Another advanced imaging method, SA Sequential Beamforming (SASB), merges the advantages of SA imaging with sequential beamforming, enhancing both the resolution and contrast of ultrasound images. It achieves resolution independent of distance while significantly reducing the size of the front-end data. Jian Zhou et al. proposed a 3D SASB volume rate enhancement method based on chirp-coded excitation, which improves the volume rate without compromising image quality. This method simultaneously uses four sub-apertures for both transmission and reception and employs a linear chirp as the excitation waveform to reduce interference. Cyst simulations using Field II indicate that this method achieves imaging quality comparable to baseline 3D SASB in both shallow and deep regions [15]. However, 3D ultrasound imaging generates a large amount of data at the front end, making it less unsuitable for high-volume portable medical applications. Virtual Source SA (VSSA) imaging technique offers an alternative approach. VSSA performs SA beamforming on focused transmit data, addressing the depth-of-field limitations of traditional SA imaging while maintaining the same lateral resolution. Mirzaei utilized VSSA for beamforming to achieve high resolution, a high number of A-lines, and penetration depth advantages similar to both SA and line-by-line imaging methods [16]. When compared to a commonly used lateral strain estimation method, VSSA method showed significant improvements. This

Table 3. Comparison of SA related algorithms in ultrasound imaging

Method	Advantages	Disadvantages	Effect comparison
SAF	Significantly improves signal-to-noise ratio and resolution.	Limited imaging depth and high data processing complexity.	Significant improvement in image quality but with increased complexity.
Golay Encoding in STA	Suppresses sidelobe amplitude and significantly improves signal-to-noise ratio.	Increases the computational burden of the system.	Significant improvement in image quality at the cost of increased complexity.
Motion Compensation Beamforming in STA	Improves both CR and SNR.	Affects the trade-off between imaging depth and resolution.	Slight improvement in image quality without additional complexity.
MSTA for Optimal Transmission Aperture	Significantly increases scattering amplitude with minimal lateral resolution loss.	Increases computational complexity of the system.	Significant improvement in image quality at the cost of higher complexity.
SASB With Chirp Encoding Excitation	Significantly increases volume rates without compromising image quality.	Requires high computing power and complex signal processing techniques.	Exceptional improvement in image quality, increased complexity and cost.
VSSA Imaging	Improves penetration depth while maintaining lateral resolution.	Increases computational complexity and implementation costs.	Moderate improvement in image quality with increased complexity.

Note: SA, Synthetic Aperture; SAF: Synthetic Aperture Focusing; STA, Synthetic Transmit Aperture; CR, contrast ratio; SNR, signal-to-noise ratio; MSTA, Multi-Element Synthetic Transmit; SASB, Synthetic Aperture Sequential Beamforming; VSSA, Virtual Source Synthetic Aperture.

technique not only enhances image clarity and detail presentation but also improves imaging of deep tissues, making it perform excellently in practical applications.

The studies mentioned above focus on SA imaging and introduce various algorithms and coding methods to optimize ultrasound imaging. The primary purpose is to improve image quality, signal-to-noise ratio, and adapt to different application scenarios. However, despite the advantages, SA technology involves complex signal processing algorithms and large data volumes, significantly increasing computational complexity compared to DAS method. The real-time performance of the system still faces challenges. **Table 3** summarizes the SA related technologies mentioned above.

MV beamforming

Adaptive beamforming algorithms are advanced beamforming techniques used to improve the quality of medical ultrasound imaging. Unlike traditional fixed beamforming methods, adaptive beamforming algorithms dynamically adjust beamforming weights based on the statistical properties of the received signals to optimize image resolution and contrast [43]. These algorithms determine the beamforming weight vectors by solving an optimization problem. The MV beamforming algorithm is one of the most commonly used adaptive beamforming algorithms. Its primary goal is to minimize the variance of the output signal by appropriately combining sensor signals in the array, thereby enhancing the desired signal in a specific direction while suppressing interference signals from other directions. Consequently, it reduces sidelobes and improves signal quality. **Figure 3** shows the architecture of the MV beamformer. Originally proposed by Capon in 1969, the MV beamforming is based on the Linear Minimum Mean Square Error theory. From a signal processing perspective, it constructs optimal weights for each channel in a phased array ultrasound endoscope to balance the desired signal against the interference signals. These weights are then applied to the sensor signals to form the output beam, thereby enhancing image quality [6]. MV beamforming performs well in low-noise environments and when the array accuracy is high. However, its performance may degrade when the directions of signal and noise are highly correlated. Therefore, in practical applications, MV beamforming typically requires consideration of the environmental conditions and signal characteristics. To improve performance, it is often combined with other beamforming methods, especially in challenging conditions where signal-to-noise ratios are low or interference is high.

In medical imaging, the simplest DAS beamformer is considered the lowest-performing due to its low resolution and relatively weak interference suppression capabilities. Compared to DAS beamformers, the MV beamforming algorithm offers better resolution at the cost of significantly increased computational complex-

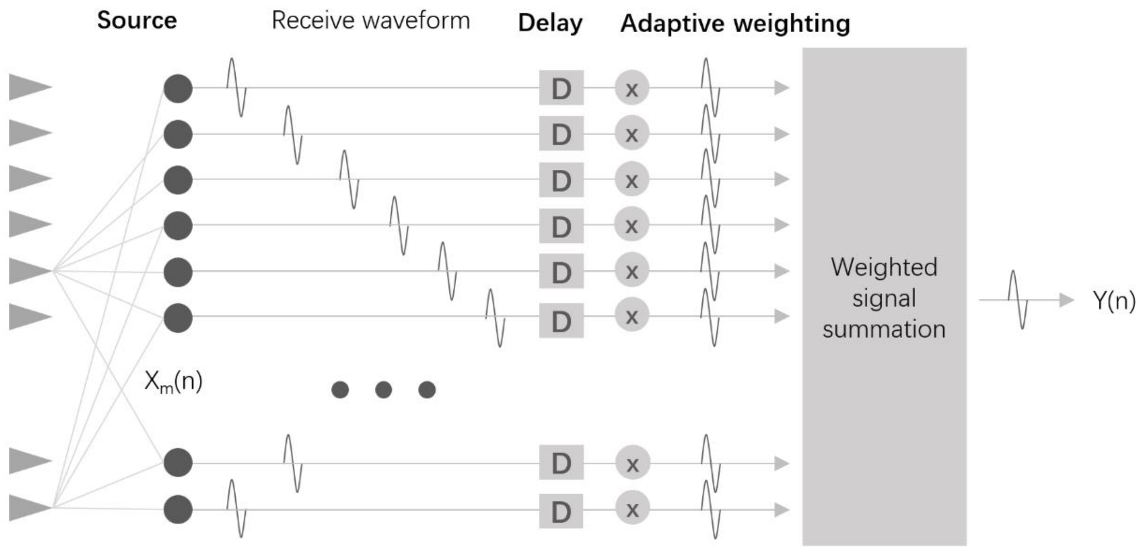

Figure 3. Minimum Variance beamformer architecture.

ity. Synnevag et al. demonstrated that using an adaptive method with a MV beamformer, characterized by low sidelobe levels and narrow beamwidth, not only improves resolution but also enhances imaging quality. By replacing the DAS beamformer with a MV beamformer at the receiving end, it is possible to reduce aperture size, increase frame rate, and improve penetration depth without sacrificing image quality [17]. The MV beamformer can also compensate for resolution loss when using smaller transducers, wider transmit beams, or lower transmit frequencies, making it a powerful tool for medical ultrasound imaging with broad application prospects and potential clinical value.

Sreejeesh proposed an enhanced MV Distortionless Response (MVDR) beamforming architecture, where the adaptive weight vector is calculated based on an improved Column-by-Column Given Rotation (CGR) method. Unlike traditional MVDR beamformers, the Quadrature Rotation Decomposition-MVDR beamformer is suitable for hardware implementation [18]. To improve real-time performance, a CGR-based parallel pipelined Quadrature Rotation Decomposition structure was adopted during the adaptive weight calculation phase, providing a highly efficient MVDR beamforming algorithm suitable for ultra-fast adaptive beamforming applications. Holfort et al. proposed an MV method for near-field beamforming of broadband data. This method is implemented in the frequency domain, providing a set of adaptive complex demodulation weights for each frequency sub-band. By combining the advantages of broadband signal processing and the MV beamforming algorithm, the aim is to significantly improve the resolution and contrast of ultrasound images. When processing frequency sub-bands, the broadband signal is divided into multiple sub-bands, with the MV beamforming algorithm applied to each sub-band, and the results then combined. This method utilizes the spectral information of broadband signals to enhance image quality [19]. Their validation using SA and plane wave transmission data—simulating 13-point targets and a circular cyst—demonstrated substantial improvements in lateral resolution, contrast, and tolerance to beam vector errors, while also reducing the number of transmissions required. Yan et al. combined MV based on submatrix spatial coherence with the Sign Coherence Factor. This method divides the receiving array into multiple submatrices and calculates the spatial coherence among them, effectively reducing coherent noise and improving image quality [20]. Additionally, this method can reduce sidelobe noise without increasing computational complexity. It significantly enhances the imaging resolution and contrast in coherent plane wave compounding imaging.

Despite the significantly improved image resolution, the performance of most MV beamforming algorithms in noise suppression is limited. Wang proposed a new pixel-adaptive weighting method based on Covariance Matrix-based Adaptive Beamforming to enhance the imaging performance of MV beamformers, namely Covariance Matrix-based Adaptive Weighting (CMSAW). The proposed CMSAW method estimates the corrected covariance matrix by adaptively applying spatial smoothing, rotational averaging, and diagonal reconstruction to compute the mean-to-standard deviation ratio [21]. CMSAW introduces adaptive diagonalization based

Table 4. Comparison of algorithms related to MV technology in ultrasound imaging

Method	Advantages	Disadvantages	Effect comparison
MV beamformer	Increases penetration depth, improves image quality.	The calculation process is complex and time-consuming, and sensitive to noise.	Improved image quality with wide application but increased CC.
Quadrature Rotation Decomposition-MVDR	High computational efficiency, suitable for ultra-fast adaptive beamforming applications.	Requires complex hardware design and optimization, with limited applicability.	Improved image quality, reduced CC, but high cost and limited applicability.
Broadband MV beamforming	Improves imaging quality and resolution.	High complexity, sensitive to broadband noise.	Significant improvement in image quality, but with increased CC.
Submatrix Spatial Coherence MV beamforming	Improves image contrast and clarity, reduces noise.	Highly dependent on the parameter selection and optimization.	Improved image quality with low noise, increased complexity.
Covariance Matrix-based Adaptive Weighting for MV beamforming	Strong adaptability and significant image quality improvements.	Complex adaptive weighting increases the computational complexity.	Improved image quality, but with high CC and poor real-time performance.
MV beamformer based on principal component analysis	Significantly improves image contrast and reduces data processing workload.	Algorithm complexity increases, making it sensitive to noise.	Improved image quality and reduced CC, but at high design costs.

Note: MV, Minimum Variance; MVDR, Minimum Variance Distortionless Response; CC, computational complexity.

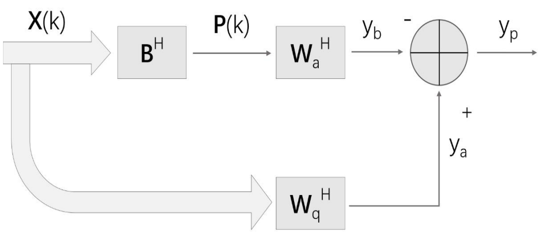

Figure 4. Structure of generalized sidelobe canceler.

on aperture coherence to enhance speckle preservation performance. CMSAW-MV can improve resolution and suppress sidelobes, incoherent clutter, and noise. With a computational complexity of O(N^2), CMSAW is suitable for real-time applications when utilizing a graphics processing unit. Eigen-space-based beamformers can remove most noises through the orthogonal projection of the signal subspace, offering better imaging contrast than traditional MV beamformers. Aliabadi proposed an innovative eigen-space beamformer called Oblique Eigen-Space MV (OESMV). This beamformer takes into account the correlation between signal and noise, by examining the SNR and using eigen-decomposition to distinguish between signal and noise subspaces [22]. The OESMV technique computes beamformer weights by projecting the MV weight vector along the noise subspace and onto the signal subspace using an oblique projection matrix. This approach allows for flexible adjustments according to specific imaging needs, yielding improved resolution, contrast, and grayscale quality.

Both the CMSAW and OESMV beamformers are extensions of MV beamforming, with the shared goal of improving contrast and resolution by minimizing output power. These methods maintain the adaptive qualities of MV beamforming but aim to reduce the computational complexity typically associated with MV techniques. However, the implementation of these algorithms requires specialized hardware and optimized algorithm design, which increases development costs and difficulty. Furthermore, these methods tend to perform poorly in noisy environments or scenarios with large datasets. **Table 4** summarizes the MV-related technologies mentioned above.

GSC

GSC is an advanced adaptive beamforming technique that effectively enhances the desired signal in the target direction while suppressing interference signals. It is widely used in fields such as radar, sonar, wireless communications, and medical ultrasound imaging, providing significant performance advantages [44-46]. GSC transforms the constrained problem of traditional adaptive beamforming algorithms into an unconstrained one by separating the linearly constrained space, thus overcoming the signal cancellation issue found in MV methods [47]. The structure of a GSC is illustrated in **Figure 4**. For adaptive beamforming, due to the high correlation of medical ultrasound echo signals, some processing algorithms must be introduced to eliminate this correlation. A commonly used method is the subarray averaging technique proposed by Evans et al. [48]. However, as the number of subarrays increases, the performance of GSC may converge toward that of a non-adaptive beamformer (like SA), reducing

Table 5. Comparison of algorithms related to GSC technology in ultrasound imaging

Method	Advantages	Disadvantages	Effect comparison
Eigenspace-Based Generalized Sidelobe Canceler Beamforming	Reduces computational complexity, enhances interference suppression capability.	Eigenvalue calculation is relatively complex and sensitive to noise.	Reduced computational complexity but with limited improvement in imaging quality.
Forward-backward Generalized Sidelobe Canceler Beamforming	Significantly improves spatial resolution and interference suppression.	The complexity of calculations increases, and the implementation of algorithms becomes more complex.	Improved image quality at the cost of higher computational complexity
Cross Sub-aperture Averaging Generalized Sidelobe Canceler Beamforming	Enhances imaging quality with greater robustness	Increased computational complexity, affecting real-time performance.	Improved image quality but with increased computational complexity.
Generalized Sidelobe Canceler Beamforming Combined with Eigenspace-Wiener Postfilter	Improves contrast and resolution of imaging, and effectively suppressed noise and scattering.	High computational workload, requiring additional hardware resources and optimization.	Significant improvement in image quality, but with increased computational complexity and cost.

Note: GSC, Generalized Sidelobe Canceller.

its adaptive advantage. While GSC can improve lateral resolution, this does not always lead to a corresponding increase in contrast. Therefore, how to obtain a reliable covariance matrix estimate that enhances lateral resolution while also improving image contrast has become a research hotspot [25].

The use of GSC significantly enhances the lateral resolution of medical ultrasound systems, but its ability to improve contrast is often unsatisfactory. Li et al. proposed a new eigen-based GSC for medical ultrasound imaging, which improves both lateral resolution and contrast [23]. In this method, the GSC weight vector is projected onto a vector subspace constructed from the eigen structure of the covariance matrix to obtain a new eigen-based GSC weight vector. By replacing the GSC weight vector with this new one, the sidelobe level is reduced, leading to improved contrast and lateral resolution. This method provides better lateral resolution and contrast compared to non-adaptive beamformers. Accurate estimation of the covariance matrix is crucial in adaptive ultrasound imaging as it fundamentally affects the performance of adaptive beamformers.

Li's team also developed a new forward and backward Generalized Sidelobe Canceller method for medical ultrasound imaging [24]. This method accurately estimates the covariance matrix using forward and backward subarray averaging. As a result, forward and backward Generalized Sidelobe Canceller achieves excellent lateral resolution and contrast, offering improved imaging quality for medical ultrasound systems. Additionally, this method is noted for its lower computational complexity and higher reliability, making it a practical solution for real-time ultrasound imaging applications.

Yang et al. proposed a new Cross-Subarray Averaging GSC (GSC-CROSS) method for medical ultrasound imaging, which uses a cross-covariance matrix instead of the traditional covariance matrix estimation [25]. In experiments using simulated echo data from scatterers and cyst-like targets, GSC-CROSS showed notable improvements in lateral resolution. Specifically, compared to DS, SA, and traditional GSC methods, GSC-CROSS improved lateral resolution by 76.9%, 68.8%, and 17.1%, respectively. The following year, Yang proposed a beamforming algorithm that combines GSC and eigen-space Wiener post-filtering. Based on the eigen-space decomposition of the covariance matrix of the received data, the components of the Wiener post-filter are calculated from the signal matrix and noise matrix. The adaptive weight vector of the GSC is further constrained by the eigen-space Wiener post-filter, making the output energy of the receiving array more closely match the desired signal compared to traditional GSC output [26]. In comparative evaluations, this method reduced the Full Width at Half Maximum by 85.5%, 80.5%, and 38.9% over DS, SA, and GSC beamforming, respectively, and improved the Contrast Ratio (CR) by 123.6%, 47.7%, and 84.4%, respectively.

Both GSC-CROSS and the combined GSC-eigenspace Wiener post-filter method significantly enhance the lateral resolution and contrast of medical ultrasound imaging systems. However, these improvements are often accompanied by an increase in computational complexity, which may affect real-time performance and implementation simplicity. **Table 5** summarizes the GSC related technologies and their respective performance enhancements, providing a comparative overview of the advancements discussed.

Algorithms related to machine learning and deep learning

Machine Learning (ML) and Deep Learning (DL) represent the latest advancements in the field of artificial intelligence. ML enables computers to learn from data and continuously improve their performance. ML methods include supervised learning, unsupervised learning, and reinforcement learning, with common algorithms such as linear regression, logistic regression, and decision trees [49]. DL, on the other hand, is a more advanced form of machine learning that uses multi-layer neural networks to simulate the human brain's structure, automatically learning complex feature representations from data to achieve higher levels of abstraction and learning capabilities. DL has achieved significant success in fields such as image recognition, speech recognition, and natural language processing [50]. These two technologies have widespread applications in various domains. In the medical field, ML and DL assist doctors in diagnosing diseases, predicting disease progression, and play crucial roles in drug development and clinical trials [51]. These technologies have contributed significantly to advancements in ultrasound beamforming, optimizing the beamforming process, improving image quality, and reducing noise and artifacts through complex data analysis and pattern recognition capabilities [52-58].

Sparse arrays reduce the number of active elements by increasing the spacing between elements, which grating lobe artifacts that degrade ultrasound image quality and reduce the contrast-to-noise ratio (CNR) in ultrasound imaging. Kumar et al. proposed a customized DL-based algorithm to estimate inactive channel data in periodic sparse arrays. This algorithm uses data from multiple active channels to estimate the inactive channels, effectively reducing element spacing in beamforming, thereby suppressing grating lobes [27]. The performance of this algorithm was validated with line targets in a water tank, multipurpose tissue-mimicking phantoms, and in vivo carotid artery data. Compared to pseudo-fully sampled arrays, grating lobe suppression improved by up to 15.25 dB, and CNR increased. The improvement in CNR in low-echo regions was more significant than in high-echo regions. The algorithm also maintained low root mean square error of phase unwrapping between fully sampled and pseudo-fully sampled arrays, makes it suitable for Doppler and elastography applications. Additionally, the speckle pattern was also preserved, making the estimated data suitable for quantitative ultrasound applications. This algorithm shows promise for improving sparse array performance and be applied in small ultrasound devices and two-dimensional arrays. Speckle noise, a common issue in traditional beamforming methods, often reduces the quality of ultrasound B-mode images. Hyun et al. proposed a framework using neural networks to reduce speckle noise during the beamforming process. A deep fully convolutional neural network (CNN) was trained to accept channel signals and output speckle-reduced echo estimates [28]. This method introduced a log-normalization loss function suitable for ultrasound imaging. Their studies showed that it is feasible to reconstruct ultrasound B-mode images using machine learning neural networks. Furthermore, the network, trained only on computer simulations, can be extended to real in vivo imaging, generating images with significantly reduced speckle noise while maintaining resolution.

Traditional medical ultrasound beamforming relies on high sampling rates that far exceed the actual Nyquist rate of the received signals, leading to large data storage and processing demands. This creates hardware and software challenges in the development of ultrasound devices and algorithms, ultimately affecting their performance. Recognizing the potential of deep learning in medical imaging, Mamistvalov et al. proposed a DL-based method for B-mode image reconstruction from temporally and spatially subsampled channel data [29]. Their approach begins by sub-sampling thedata below the Nyquist rate, aligning it in the frequency domain, and then converting it back to the time domain. The data were further subsampled spatially to acquire only a subset of the received signals. An encoder-decoder CNN was then trained using this partial data, with the MV beamformed signal generated from the original fully sampled data as the target. Their method produced high-quality B-mode images with superior resolution compared to previously proposed compressed data reconstruction techniques (e.g., NESTA) and DAS beamforming of fully sampled data. In terms of contrast-to-noise ratio, their results were comparable to MV beamforming with fully sampled data, achieving better and more efficient imaging than most current clinical practices. Ultrafast ultrasound imaging, capable of acquiring full-view images at thousands of frames per second, enables the analysis of rapidly changing physical phenomena in the human body. However, this im-

Table 6. Comparison of algorithms related to DL technology in ultrasound imaging

Method	Advantages	Disadvantages	Effect comparison
Gap-Filling Method for Suppressing Grating Lobes in Ultrasound Imaging Using DL	Effectively suppresses grid lobes, improves image quality and resolution.	Lack of generalization, requires a large amount of data sets and computing resources.	Significant improvement in image quality, but with high complexity and poor real-time performance.
Beamforming and Speckle Reduction Using Neural Networks	Enhances image contrast, automatically captures complex signal features during training.	High demand for computing resources, risk of overfitting with insufficient data.	Substantial improvement in image quality, but resource-intensive and limited real-time performance.
Deep-Learning Based Adaptive Ultrasound Imaging from Sub-Nyquist Channel Data	Reduces data acquisition and processing complexity while maintaining high-quality imaging results.	High implementation difficulty, requires extensive computing resources.	Improved image quality, but with high complexity and suboptimal real-time performance.
CNN-Based Ultrasound Image Reconstruction for Ultrafast Displacement Tracking	Improves speed and accuracy in dynamic imaging with ultrafast displacement tracking.	High cost of data acquisition and annotation, and limited generalization ability.	Enhanced image quality and fast imaging speed, but with poor generalization ability and the high cost.

Note: DL, Deep Learning; CNN, Convolutional Neural Network.

aging modality faces a trade-off between frame rate and image quality-higher frame rates can introduce motion artifacts while improving image quality typically requires more acquisitions, slowing the process. Perdios et al. addressed this challenge with a CNN-based method that reconstructs high-quality frames from single ultrafast acquisitions while using only two consecutive frames for two-dimensional displacement estimation. By integrating this CNN-based image reconstruction with a cross-correlation-based speckle tracking algorithm, they were able to estimate displacement even in areas affected by sidelobe and grating lobe artifacts, which traditional DAS methods struggle with [30]. Therefore, the proposed method may unlock the full potential of ultrafast ultrasound, finding applications in ultra-sensitive cardiovascular motion and flow analysis or shear wave elastography.

These studies illustrate the power of deep learning to enhance various aspects of ultrasound imaging, from beamforming and artifact suppression to speckle noise reduction and image reconstruction. Their advantages lie in the significant improvements in image quality and adaptability. However, challenges remain, such as high computational resource requirements, strong data dependence, and high implementation complexity. **Table 6** summarizes DL-related techniques mentioned above.

Other beamforming algorithms

Reverberation noise is a significant issue in ultrasound imaging, as it results from multiple reflections of sound waves between structural boundaries, resulting in image clutter and reduced contrast. To mitigate the impact of reverberation noise, Shin et al. proposed a novel beamforming technique called Multiphasic Adaptive Cross-Cancellation (MPAX), an improved version of the Delay and Apodization Crosstalk technique. While Delay and Apodization Crosstalk uses complementary square wave amplitude cancellations, MPAX improves upon this by employing multiple pairs of complementary sine phase cancellations, which more precisely control the amplitude and position of grating lobes. This results in an improved weighting matrix that effectively suppresses reverberation noise [31]. MPAX has demonstrated significant success in reducing near-field reverberation noise and improving ultrasound image contrast, making it a promising tool for generating high-contrast images and enabling more accurate clinical diagnoses. In another approach, Nghia et al. proposed a new unified pixel-level beamforming algorithm that better adapts to the non-spherical waveforms of transmitted beams, allowing the selection of the optimal signal for data synthesis from each transducer waveform at that location [32]. This method significantly improves image resolution and contrast by optimizing signal processing for each pixel, though it increases computational costs, requiring more resources and longer processing times. Nevertheless, the algorithm performed excellently in limited in vivo studies, demonstrating its reliability in handling real biological tissues. The results indicate that although further optimization and research are needed to reduce computational costs, this new beamforming algorithm has significant potential in clinical applications and could be widely used in medical diagnostics.

In Multi-Line Transmission, high frame rate ultrasound imaging is achieved by simultaneously transmitting multiple focused beams in different directions, thereby increasing imaging speed and efficiency. However, this method can lead to crosstalk between different beams, resulting in unwanted artifacts that affect image quality. The Filtered Delay Multiply and Sum (F-DMAS) beamforming algorithm has been proven to reduce such artifacts. This beamformer effectively reduces artifacts in the image and improves spatial resolution by using a nonlinear spatial coherence algorithm, resulting in clearer imaging. Matrone et al. proposed a "short-delay F-DMAS" formula to enhance the performance of the F-DMAS beamformer while managing computational complexity [33]. Specifically, by setting a maximum delay value to control the signal delay time involved in spatial coherence calculations, the "short-delay F-DMAS" formula maintains or improves the performance of the F-DMAS algorithm. Byram et al. introduced a model-based beamforming algorithm, known as Aperture Domain Model Image Reconstruction (ADMIRE) [59-62]. This algorithm uses a model of the reflected wavefronts of scatterers within the region of interest in the aperture domain signal, enabling the algorithm to identify scatterer locations and suppress clutter, particularly off-axis scattering and reverberation artifacts. By decomposing this signal into components of clutter and the desired signal, ADMIRE effectively suppresses clutter, including off-axis scattering and reverberation artifacts, resulting in clearer images. The algorithm preserves de-cluttered channel data, which can be further processed by other techniques to enhance image quality. Dei et al. developed a Coherence Factor (CF) weighting technique, finding that ADMIRE combined with CF weighting further improved image quality in certain aspects [34]. CF weighting, as a post-processing technique, enhances contrast while reducing CNR and speckle SNR. The results indicate that ADMIRE is robust against model mismatch caused by variations in sound speed, especially when the actual sound speed is slower than the assumed sound speed.

Hybrid beamforming significantly reduces the cost and power consumption of fully digital sensor arrays by decreasing the number of active front-end components. Sparse arrays can further reduce hardware costs. Rajamäki et al. proposed an algorithm for approximating fully digital beamforming solutions, extending to the more challenging hybrid and analog beamforming scenarios, using quantized phase shifters [35]. They determined the upper bounds for achieving fully digital solutions and derived closed-form expressions for beamforming weights in these cases. The research results indicate that combining sparse arrays and hybrid beamforming can significantly reduce the number of required elements and front-ends while achieving the resolution of a fully digital uniform array. Ni et al. introduced a new method where array elements are simultaneously excited by signals encoded with random sequences, generating non-focused ultrasound wavefronts with random interference [36]. As these wavefronts propagate through the medium, their energy is reflected back from the tissue, giving individual scatterers unique pulse responses. This method can significantly improve ultrasound imaging performance, especially in organ boundary detection and lesion localization. By using randomly encoded signals, the reflected waves from individual scatterers in the tissue have unique pulse responses, enabling more precise identification and localization of scatterers. This helps to more clearly distinguish different tissues, thereby enhancing the accuracy of organ boundary detection, particularly in cases involving complex tissue structures. Goudarzi et al. proposed a flexible framework for beamforming using the Alternating Direction Method of Multipliers, where each term is optimized separately. Their formulation includes the use of denoising algorithms within the beamforming process, specifically the Plug-and-Play and Regularization by Denoising (RED) [37]. The RED algorithm provides superior image quality in terms of contrast metrics while preserving speckle statistics.

Conventional ultrasound imaging typically employs DAS beamforming with dynamic receive focusing for image reconstruction, valued for its simplicity and robustness. However, DAS beamforming geometrically estimates delays assuming a constant speed of sound in the medium, typically 1540 m/s, without accounting for tissue heterogeneity. This approximation leads to cumulative delay estimation errors with increasing depth, reducing the resolution, contrast, and overall accuracy of ultrasound images. Asif et al. proposed a DAS method based on the fast-marching method for focused transmission, which utilizes an approximate speed of sound map to estimate refraction-corrected propagation delays for each pixel in the medium [38]. This method has been qualitatively and quantitatively validated at an imaging depth of approximately 11 cm, showing significant improvements in imaging errors caused by tissue heterogeneity, especially when speed of sound variations are induced by fat layers, making it valuable for complex abdominal and liver imaging applications. Guo et al. introduced a pixel-based Delay Multiply and Sum beamforming method combined with a Wiener filter to enhance ultrasound image quality [39]. Compared to traditional dynamic focusing, the unified pixel-based beamforming technique significantly improves lateral resolution. Besides, this method retains favorable characteristics of beamformers while significantly enhancing spatial resolution and contrast compared to the unified pixel-based algorithm. Its simplicity and excellent performance demonstrate its potential for clinical applications. Vayyeti et al. proposed a novel nonlinear beamforming method called Filtered Delay Optimal Weighted Multiply and Sum (F-DowMAS), which adapts optimal weights for each imaging point in traditional focused beam systems [40]. This method shows significant advantages in improving image quality, including better resolution and contrast, and reduced noise and artifacts. Compared to DAS and F-DMAS, F-DowMAS improves axial resolution by 57.04% and 46.95%, lateral resolution by 58.21% and 53.40%, CR by 67.35% and 39.25%, and CNR by 44.04% and 30.57%, respectively. This method provides a new direction in ultrasound imaging technology, showcasing the immense potential of nonlinear beamforming algorithms in enhancing diagnostic capabilities.

Discussions and challenges

SA technology and its improved beamforming algorithms offer significant advantages in enhancing resolution and improving the signal-to-noise ratio. However, these technologies require substantial processing power and memory resources. Additionally, SA techniques are highly sensitive to motion, making them prone to motion artifacts, which challenges their real-time application. MV algorithms, known for reducing coherent noise and significantly improving resolution and contrast, face similar challenges. GSC algorithms can reduce interference by canceling the phase and amplitude of undesired signals, showing robustness in multipath propagation and noisy environments. However, similar to SA and MV, they require significant computational resources and may introduce additional complexity in some cases. Machine learning and deep learning have revolutionized ultrasound beamforming by providing tools that can adapt to nonlinear relationships and complex signal environments. These methods excel at enhancing image resolution and contrast. However, the training and tuning processes of these models can be time-consuming and computationally intensive, making real-time applications nearly impossible. Composite beamforming algorithms offer the advantage of combining multiple beamforming techniques, thereby achieving higher image quality and performance. By integrating various algorithms, the limitations of individual techniques can be addressed, leading to improved resolution, contrast, and noise resistance. Additionally, composite algorithms can be flexibly adjusted for adaptation to different imaging needs and patient characteristics, allowing for more personalized imaging outcomes.

In recent years, the importance of ultrasound imaging in medicine has increased significantly. Medical ultrasound is a non-invasive and safe imaging technique that does not involve radiation or contrast agents, posing no risk of radiation damage to patients and being suitable for individuals of all ages. Ultrasound imaging is widely used in clinical diagnosis across almost all medical fields, including cardiology, hepatology, nephrology, endocrinology, gynecology, obstetrics, and orthopedics, for detecting and diagnosing various diseases and abnormalities. Additionally, ultrasound imaging offers advantages such as real-time capability, low cost, and portability, making it valuable in emergency medicine, surgical guidance, bedside diagnosis, and routine clinical practice. Ultrasound beamforming plays a crucial role in optimizing image resolution, contrast, and overall quality. This not only allows physicians to observe tissue structures and lesions more clearly but also aids in guiding interventional treatments, improving surgical outcomes. Therefore, the continuous advancement of ultrasound beamforming technology is vital for enhancing clinical diagnosis and medical standards. Future developments will depend on efficient algorithms, advanced noise suppression techniques, accurate speed-of-sound corrections, optimization of cost and energy consumption, and integration with multimodal imaging. These innovations will drive the widespread application of ultrasound beamforming technology in medical imaging, enhancing the accuracy and efficiency of clinical diagnosis.

Conclusion

In summary, ultrasound beamforming technology is one of the core components of medical ultrasound imaging, and its advancements directly impact image quality and diagnostic accuracy. Although existing beamforming techniques (such as SA, MV, and GSC) and deep learning-based methods have achieved significant progress in improving resolution, contrast, and noise resistance, their high computational resource requirements and complexity remain major obstacles to real-time applications. Composite algorithms, by integrating multiple techniques, offer effective solutions to these challenges. At the same time, medical ultrasound, due to its non-invasive, safe, and real-time nature, has become an indispensable tool for clinical diagnosis and treatment. In the future, through algorithm optimization, enhanced system efficiency, and integration with multimodal imaging, ultrasound beamforming technology will play an even greater role in medicine, providing patients with more precise, efficient, and personalized diagnostic and treatment experiences.

Author contributions: Fei Liu proposed ideas, conducted information searches, organized and analyzed data, and write the manuscript. Haipo Cui proposed ideas, reviewed and edited the manuscript. Fujia Sun reviewed and edited the manuscript. Shuhao Hou helped write the manuscript. Peng Yue participated in manuscript revisions. All authors read and approved the final manuscript.

References

[1] Bushberg JT, Seibert JA, Leidholdt EM, et al. The essential physics of medical imaging. Philadelphia (US). Lippincott Williams and Wilkins, 2011.

[2] Kremkau FW. Diagnostic Ultrasound: Principles and Instruments. Ultrasound Q 1994;12(1):65.

[3] Madhavanunni AN, Raveendranatha Panicker M. Beam multiply and sum: A tradeoff between delay and sum and filtered delay multiply and sum beamforming for ultrafast ultrasound imaging. Biomed Signal Process Control 2023;85:104807.

[4] Baker LAS, Bamber JC. Effect of dynamic receive focusing on Reflex Transmission Imaging (RTI). 2002 IEEE Ultrasonics Symposium, 2002. Proceedings. 2002;1581-1584 vol.1582.

[5] Jensen JA, Nikolov SI, Gammelmark KL, et al. Synthetic aperture ultrasound imaging. Ultrasonics 2006;44 Suppl 1:e5-e15.

[6] Yu ZL, Hwa Er M. A robust minimum variance beamformer with new constraint on uncertainty of steering vector. Signal Process 2006;86(9):2243-2254.

[7] Nilsen CI, Hafizovic I. Beamspace adaptive beamforming for ultrasound imaging. IEEE Trans Ultrason Ferroelectr Freq Control 2009;56(10):2187-2197.

[8] Li W, Chen XD, Li JK, et al. Parallel Implementation of Endoscopic Ultrasound Synthetic Aperture Imaging Algorithm. Laser Optoelectron Prog 2017;54(10);394-402.

[9] Su T, Wang YY, Zhang S. Delay Multiply and Sum Ultrasound Beamforming Algorithm Based on Multi-Line Reception. J Northeastern Univ (Nat Sci) 2019;40(06):771-776.

[10] Wang P, Jiang JY, Li F, et al. Minimum Variance Ultrasound Imaging Algorithm Based on Signal-to-Noise Ratio Post-Filtering and Feature Space Fusion. Acta Acust 2019;44(01):136-144.

[11] Chen X, Li M, Li Y, et al. Synthetic aperture focusing for medical endoscopic ultrasonography. J Xray Sci Technol 2011;19(1):127-137.

[12] Trots I, Tasinkevych Y, Nowicki A, et al. Golay Coded Sequences in Synthetic Aperture Imaging Systems. Arch Acoust 2011;36(4):913-926.

[13] Chen YH, Lin YM, Ho KY, et al. Low-Complexity Motion-Compensated Beamforming Algorithm and Architecture for Synthetic Transmit Aperture in Ultrasound Imaging. IEEE Trans Acoust Signal Process 2014;62(4):840-851.

[14] Tasinkevych Y, Trots I, Nowicki A, et al. Optimization of the Multi-element Synthetic Transmit Aperture Method for Medical Ultrasound Imaging Applications. Acoust Imaging 2012;37:47-55.

[15] Zhou J, Wei S, Jintamethasawat R, et al. High-Volume-Rate 3-D Ultrasound Imaging Based on Synthetic Aperture Sequential Beamforming With Chirp-Coded Excitation. IEEE Trans Ultrason Ferroelectr Freq Control 2018;65(8):1346-1358.

[16] Mirzaei M, Asif A, Rivaz H. Virtual Source Synthetic Aperture for Accurate Lateral Displacement Estimation in Ultrasound Elastography. IEEE Trans Ultrason Ferroelectr Freq Control 2021;68(5):1687-1695.

[17] Synnevag JF, Austeng A, Holm S. Benefits of minimum-variance beamforming in medical ultrasound imaging. IEEE Trans Ultrason Ferroelectr Freq Control 2009;56(9):1868-1879.

[18] Sreejeesh SG, Sakthivel R, Kidav JU. Superior Implementation of Accelerated QR Decomposition for Ultrasound Imaging. IEEE Access 2020;8:156244-156260.

[19] Holfort IK, Gran F, Jensen JA. Broadband minimum variance beamforming for ultrasound imaging. IEEE Trans Ultrason Ferroelectr Freq Control 2009;56(2):314-325.

[20] Yan X, Wang Y. A submatrix spatial coherence approach to minimum variance beamforming combined with sign coherence factor for coherent plane wave compounding. Technol Health Care 2022;30(S1):11-25.

[21] Wang Y, Wang Y, Liu M, et al. Minimum variance beamforming combined with covariance matrix-based adaptive weighting for medical ultrasound imaging. Biomed Eng Online 2022;21(1):40.

[22] Aliabadi S, Yu J, Wang Y. Enhance contrast in PCA based beamformers using smoothing

kernel. Biomed Mater Eng 2015;26 Suppl 1:S1613-S1621.
[23] Li J, Chen X, Wang Y, et al. Eigenspace-Based Generalized Sidelobe Canceler Beamforming Applied to Medical Ultrasound Imaging. Sensors (Basel) 2016;16(8):1192.
[24] Li J, Chen X, Wang Y, et al. Forward-backward generalized sidelobe canceler beamforming applied to medical ultrasound imaging. AIP Adv 2017;7(1):015201.
[25] Yang J, Li J, Chen X, et al. Cross Subaperture Averaging Generalized Sidelobe Canceler Beamforming Applied to Medical Ultrasound Imaging. Appl Sci 2021;11(18):8689.
[26] Yang J, Chen X, Cai H, et al. Generalized sidelobe canceler beamforming combined with Eigenspace-Wiener postfilter for medical ultrasound imaging. Technol Health Care 2022;30(S1):501-512.
[27] Kumar V, Lee PY, Kim BH, et al. Gap-Filling Method for Suppressing Grating Lobes in Ultrasound Imaging: Experimental Study With Deep-Learning Approach. IEEE Access 2020;8:76276-76286.
[28] Hyun D, Brickson LL, Looby KT, et al. Beamforming and Speckle Reduction Using Neural Networks. IEEE Trans Ultrason Ferroelectr Freq Control 2019;66(5):898-910.
[29] Mamistvalov A, Amar A, Kessler N, et al. Deep-Learning Based Adaptive Ultrasound Imaging From Sub-Nyquist Channel Data. IEEE Trans Ultrason Ferroelectr Freq Control 2022;69(5):1638-1648.
[30] Perdios D, Vonlanthen M, Martinez F, et al. CNN-Based Ultrasound Image Reconstruction for Ultrafast Displacement Tracking. IEEE Trans Med Imaging 2021;40(3):1078-1089.
[31] Shin J, Chen Y, Malhi H, et al. Ultrasonic Reverberation Clutter Suppression Using Multiphase Apodization With Cross Correlation. IEEE Trans Ultrason Ferroelectr Freq Control 2016;63(11):1947-1956.
[32] Nguyen NQ, Prager RW. High-Resolution Ultrasound Imaging With Unified Pixel-Based Beamforming. IEEE Trans Med Imaging 2016;35(1):98-108.
[33] Matrone G, Ramalli A. Spatial Coherence of Backscattered Signals in Multi-Line Transmit Ultrasound Imaging and Its Effect on Short-Lag Filtered-Delay Multiply and Sum Beamforming. Appl Sci 2018;8(4);486.
[34] Dei K, Byram B. A Robust Method for Ultrasound Beamforming in the Presence of Off-Axis Clutter and Sound Speed Variation. Ultrasonics 2018;89:34-45.
[35] Rajamäki R, Chepuri SP, Koivunen V. Hybrid Beamforming for Active Sensing Using Sparse Arrays. IEEE Trans Signal Process 2020;68:6402-6417.
[36] Ni P, Lee HN. High-Resolution Ultrasound Imaging Using Random Interference. IEEE Trans Ultrason Ferroelectr Freq Control 2020;67(9):1785-1799.
[37] Goudarzi S, Basarab A, Rivaz H. Inverse Problem of Ultrasound Beamforming With Denoising-Based Regularized Solutions. IEEE Trans Ultrason Ferroelectr Freq Control 2022;69(10):2906-2916.
[38] M S A, Malamal G, A N M, et al. Fast Marching based Tissue Adaptive Delay Estimation for Aberration Corrected Delay and Sum Beamforming in Ultrasound Imaging. 2023 45th Annual International Conference of the IEEE Engineering in Medicine & Biology Society (EMBC) 2023:1-4.
[39] Guo H, Xie HW, Zhou GQ, et al. Pixel-based approach to delay multiply and sum beamforming in combination with Wiener filter for improving ultrasound image quality. Ultrasonics 2023;128:106864.
[40] Vayyeti A, Thittai AK. Optimally-weighted non-linear beamformer for conventional focused beam ultrasound imaging systems. Sci Rep 2021;11(1):21622.
[41] Curlander JC, McDonough RN. Synthetic Aperture Radar: Systems and Signal Processing. New York (US). Wiley, 1991.
[42] Soumekh M. Synthetic Aperture Radar Signal Processing with MATLAB Algorithms. New York (US). Wiley, 1999.
[43] Shen CC, Huang CL. Improvement in Multi-Angle Plane Wave Image Quality Using Minimum Variance Beamforming with Adaptive Signal Coherence. Sensors (Basel) 2024;24(1):262.
[44] Li JK, Wang Y, Chen XD, et al. A robust approach to generalized sidelobe canceler for medical ultrasound imaging. J Med Imag Health Inf 2018;8(1):88-93.
[45] Wang Y, Zheng C, Zhao X, et al. Adaptive scaling Wiener postfilter using generalized coherence factor for coherent plane-wave compounding. Comput Biol Med 2020;116:103564.
[46] Li JK, Ma Z, Mao L, et al. Broadband generalized sidelobe canceler beamforming applied to ultrasonic imaging. Appl Sci 2020;10(4):1207.
[47] Albulayli M, Rakhmatov D. Hybrid adaptive/nonadaptive beamforming for ultrasound imaging. 2013 IEEE International Conference on Acoustics, Speech and Signal Processing 2013;1061-1065.
[48] Evans JE, Johnson JR, Sun DF. High resolution angular spectrum estimation techniques for terrain scattering analysis and angle of arrival estimation. Proc 1st ASSP Workshop Spectral Estim 1981;134-139.
[49] Bishop CM. Pattern Recognition and Machine Learning. New York (US). Springer New York,

2006.
[50] Goodfellow I, Bengio Y, Courville A. Cambridge, MA (USA). Deep learning. MIT press, 2016.
[51] Obermeyer Z, Emanuel EJ. Predicting the Future - Big Data, Machine Learning, and Clinical Medicine. N Engl J Med 2016;375(13):1216-1219.
[52] Luijten B, Cohen R, de Bruijn FJ, et al. Adaptive Ultrasound Beamforming Using Deep Learning. IEEE Trans Med Imaging 2020;39(12):3967-3978.
[53] Mamistvalov A, Eldar YC. Compressed fourier-domain convolutional beamforming for wireless ultrasound imaging. arXiv:2010.13171 2020.
[54] Wang Z, Chen J, Hoi SCH. Deep Learning for Image Super-Resolution: A Survey. IEEE Trans Pattern Anal Mach Intell 2021;43(10):3365-3387.
[55] Ashikuzzaman M, Heroux A, Tang A, et al. Displacement Tracking Techniques in Ultrasound Elastography: From Cross Correlation to Deep Learning. IEEE Trans Ultrason Ferroelectr Freq Control 2024;71(7):842-871.
[56] Goudarzi S, Basarab A, Rivaz H. A Unifying Approach to Inverse Problems of Ultrasound Beamforming and Deconvolution. IEEE Trans Comput Imaging 2023;9:197-209.
[57] Huang C, Lanza di Scalea F. Application of Sparse Synthetic Aperture Focusing Techniques to Ultrasound Imaging in Solids Using a Transducer Wedge. IEEE Trans Ultrason Ferroelectr Freq Control 2024;71(2):280-294.
[58] Perdios D, Vonlanthen M, Martinez F, et al. CNN-Based Image Reconstruction Method for Ultrafast Ultrasound Imaging. IEEE Trans Ultrason Ferroelectr Freq Control 2022;69(4):1154-1168.
[59] Byram B. Ultrasonic reverberation and off-axis clutter suppression using aperture domain signal decomposition. Proc.SPIE 2013;86750T.
[60] Byram B, Dei K, Dumont D. An improved acoustic clutter model and direct in vivo assessment of off-axis and multipath clutter energy in the liver. 2014 IEEE International Ultrasonics Symposium 2014;531-534.
[61] Byram B, Dei K, Tierney J, et al. A model and regularization scheme for ultrasonic beamforming clutter reduction. IEEE Trans Ultrason Ferroelectr Freq Control 2015;62(11):1913-1927.
[62] Dei K, Byram B. The Impact of Model-Based Clutter Suppression on Cluttered, Aberrated Wavefronts. IEEE Trans Ultrason Ferroelectr Freq Control 2017;64(10):1450-1464.

Progress in Medical Devices
ISSN: 2957-5478

Zentime

Review Article https://doi.org/10.61189/192898kemezc

Research progress of ankle-foot rehabilitation robots

Hongtao Shen, Qingyun Meng, Mingxia Wei, Jiajia Zha

School of Health Science and Engineering, University of Shanghai for Science and Technology, Shanghai 200093, China.

Corresponding author: Qingyun Meng.

Declaration of conflict of interest: None.

Received August 23, 2024; Accepted October 16, 2024; Published March 31, 2025

Highlights

- Three types of ankle-foot rehabilitation robots, categorized by structure, are designed to address different stages of rehabilitation training.
- The development of control methods for rehabilitation robots, including integration of multiple control methods, remains a key area of exploration.
- The combination of artificial intelligence algorithms and rehabilitation robots represents a significant and promising research direction.

Abstract

With the development of medical-engineering integration technology and the growing clinical rehabilitation demands, intelligent rehabilitation robots have emerged as a prominent area of research in stroke rehabilitation. The application of exoskeleton rehabilitation robots holds significant potential to alleviate the pressure on rehabilitation resources in China. These robots offer high-intensity, high-repetition rehabilitation training for stroke patients, helping to restore limb motor function, improve daily living independence, and contribute to neuroplasticity. As such, they are becoming an essential treatment modality for patients with motor function disorders. In this review, we first categorize ankle-foot rehabilitation robots based on the interaction methods between the robot and the user, detailing their structural characteristics and application scenarios. Additionally, we classify existing control strategies, including admittance control, impedance control, electromyography control, trajectory tracking control, and Proportional-Integral-Derivative control, based on the rehabilitation needs at various stages of recovery. Each control method is summarized, and their current research status is analyzed. Besides, current research status of key technologies in rehabilitation robots, both domestically and internationally are also summarized in this paper. Finally, the key challenges in the development of ankle-foot rehabilitation robots and future research directions are discussed, providing a reference for the research and design of these robots.

Keywords: Stroke rehabilitation, motor function disorder, control strategies, ankle-foot rehabilitation robot

Introduction

Stroke, commonly known as a cerebrovascular accident, is an acute cerebrovascular disease characterized by high incidence, high mortality, and high disability rates [1]. Research indicates that stroke is the second leading cause of death globally and the primary cause of adult disability. Among stroke survivors, approximately 80% experience varying degrees of limb dysfunction, with hemiplegia being the most common [2, 3]. This leads to a loss of independence in daily activities and severely impacts the quality of life [4]. According to data from Seventh National Census in 2020, China has 264 million people aged 60 and above, accounting for 18.73% of the population, highlighting the significant aging trend in China [5]. Aging brings about various health issues, including a decline in limb function, which causes inconvenience for many elderly individuals. Besides stroke, neurological diseases such as

Address correspondence to: Qingyun Meng, School of Health Science and Engineering, University of Shanghai for Science and Technology, Yangpu District, Shanghai 200093, China. Tel: +86-13761813609; E-mail: mengqy@sumhs.edu.cn.

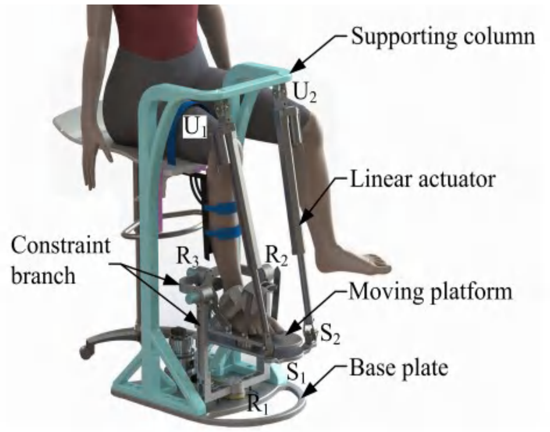

Figure 1. Wearable parallel robot. This figure is cited from [18].

multiple sclerosis and spinal cord injuries also result in limb dysfunction, necessitating targeted rehabilitation measures to improve motor function [6].

Clinical studies show that 90% of stroke patients can regain the ability to walk and live independently with effective rehabilitation treatment, while only 6% can achieve this without rehabilitation [7]. Restoring limb motor function is the primary goal of stroke rehabilitation [8]. Stroke patients often experience a range of motor impairments, such as reduced muscle strength and abnormal muscle contraction timing [9, 10]. However, the brain's plasticity allows for personalized rehabilitation treatment and training for patients with motor dysfunction. Early intervention with rehabilitation treatment for stroke patients with hemiplegia yields better outcomes. Exercise therapy, a key component of rehabilitation, can promote neural recovery, improve limb motor function, and enhance daily living abilities [11].

For stroke patients, traditional rehabilitation primarily involves one-on-one passive training administered by physicians. The effectiveness of this approach is largely dependent on the physician's skill level, and maintaining consistent training intensity can be challenging. This training model is time-consuming, labor-intensive, and involves a prolonged rehabilitation process. Moreover, it lacks quantitative and objective assessment, making it difficult to optimize training parameters for the best treatment outcomes. Furthermore, rehabilitation therapists mainly rely on their experience to assess the patient's limb condition and formulate rehabilitation plans, lacking precise detection methods to evaluate the patient's limb motor state, which hinders timely adjustments to the rehabilitation treatment plan [12]. A significant contributor to ankle dysfunction is the central nervous system damage, which requires targeted stimulation to promote the recovery of motor and sensory functions [13]. During physical therapy, patients gradually regain ankle joint range of motion, build muscle strength, and restore motor function [14].

In recent years, the development of medical-engineering integration technologies, such as the combination of robotics and medical theory, has provided new avenues for rehabilitation treatment. Research shows that rehabilitation robot technology plays a crucial role in training patients with limb dysfunction [15]. Intelligent rehabilitation robots help reduce the labor intensity of therapists, offer precise control over the complexity of motor task learning, promote the recovery of limb motor function, and enhance patients' daily living capabilities [16]. With the continuous advancement of intelligent rehabilitation robots, their standardization, intelligence, and humanization will improve, leading to faster recovery and better outcomes for patients [17].

This review begins by classifying and comparing ankle-foot rehabilitation robots based on their interaction methods with the human body, explaining the application of various control methods in these robots. It also discusses their characteristics and research status. The review then enumerates the key technologies of rehabilitation robots and summarizes the challenges faced by ankle-foot rehabilitation robots, and discusses potential future development directions.

Classification of ankle-foot rehabilitation robots

Ankle-foot rehabilitation robots can be classified based on several criteria. By drive method, they can be motor-driven, pneumatic-driven, or hydraulic-driven. By training method, they can be categorized into passive movement, active assistive movement, and resistive movement. In terms of actuator connection, they can be either serial or parallel. According to usage mode, they are classified into seated ankle-foot rehabilitation robots and recumbent ankle-foot rehabilitation robots. The most common structural classifications include platform-type, orthotic-type, and exoskeleton-type ankle-foot rehabilitation robots.

Platform-type rehabilitation robot

In the early stages of rehabilitation, muscle atrophy often weakens ankle joint movement. Plat-

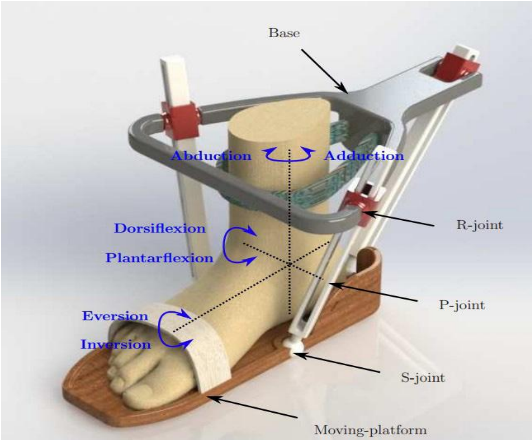

Figure 2. Parallel platform ankle foot rehabilitation robot. This figure is cited from [19].

Figure 3. 3-PRS (prismatic-revolute-spherical) parallel robot. This figure is cited from [20].

Figure 4. Pneumatic muscle-driven flexible ankle foot rehabilitation robot. This figure is cited from [21].

form-type ankle-foot rehabilitation robots are designed to gradually increase strength training by adjusting the robot's resistance and load, thereby promoting the recovery and strengthening of damaged muscles and tissues. These robots are characterized by their adaptability and high precision, ensuring reliability and safety during the rehabilitation process.

Zuo et al. designed a new type of wearable robot with a parallel platform configuration (**Figure 1**) [18]. This robot features a simple mechanical setup with sufficient motion isotropy, transmission performance, and torque capability. Compared to ankle-foot rehabilitation robots with redundant actuators, this design uses a 2-UPS/RRR (universal-prismatic-spherical/revolute-revolute-revolute) parallel mechanism to simplify operation and control system development, effectively reducing manufacturing costs and the burden on therapists. Additionally, various safety measures were implemented, including a low-moving platform to minimize seat height and removable mechanical limits to restrict the robot's working space, protecting patients from secondary injuries. The robot is equipped with a multi-mode force/position data acquisition system, which collects kinematic and dynamic information to facilitate both active and passive rehabilitation training.

Nurahmi et al. developed a constraint-based 3-RPS (revolute-prismatic-spherical) parallel robot (**Figure 2**), which features a robot system with two operational modes based on the design of the base, moving platform, and working mode [19]. The robot's ability to perform translation and rotation movements was tested by parameterizing its pose workspace. The maximum inner circle diameter was used to track the maximum tilt angle in any azimuthal direction without triggering singularities. The robot employs a reconfiguration strategy to ensure that the moving platform operates effectively at any height.

Abu-Dakka et al. developed a platform-type parallel robot (**Figure 3**), which uses passive rehabilitation training targeting ankle inversion/eversion movements [20]. Based on dynamic motion primitives and iterative learning control methods, they designed motion trajectories and used recorded forces and motion paths to repetitively guide the patient through movements within predefined repetition counts. During the exercise, perceived forces are monitored, and necessary offsets are applied to the original trajectory to adjust and reduce measurement range. After completing the preset number of repetitions, the trajectory range is gradually restored until the patient can perform the initially designed exercise.

Lu et al. from Wuhan University of Technology designed a platform-type flexible ankle-foot rehabilitation robot (**Figure 4**) with multiple degrees of freedom, driven by pneumatic muscles [21]. The robot features a drive section and a

Figure 5. Wearable robot ankle foot orthotics. This figure is cited from [22].

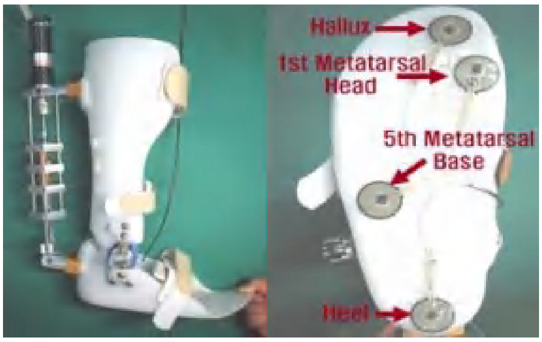

Figure 6. Single degree of freedom ankle foot orthotics. This figure is cited from [23].

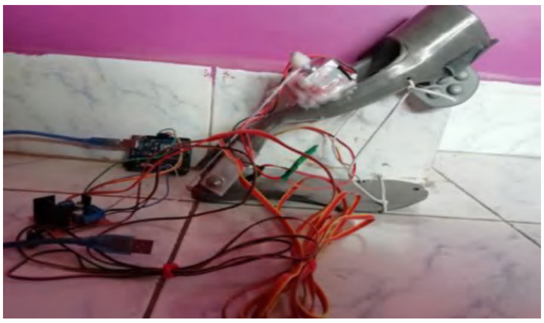

Figure 7. Electric ankle foot orthotics. This figure is cited from [24].

motion platform, ensuring alignment of the robot's and patient's ankle joint rotation centers. It mainly consists of a primary motion module, a power transmission module, and a support module, facilitating joint rotational movements for the patient. The power transmission module, driven by pneumatic muscles, connects to the motion platform via flexible cables and uses pulleys to change the direction of the driving forces, meeting the rehabilitation needs of the ankle joint. A telescopic rod in the robot's mechanism adjusts the height of the thigh support plate to accommodate patients with different leg lengths.

Orthotic-type rehabilitation robot

Orthotic-type rehabilitation robots are designed to closely fit the patient's ankle and foot, providing stable support and control. Their structure is designed to fit the anatomical model of the human body, ensuring both comfort and safety. By combining modern robotics technology with orthotic design, these robots assist patients in restoring ankle function and mobility, thereby enhancing rehabilitation outcomes.

Kwon et al. developed a lightweight and easy-to-wear ankle orthosis (**Figure 5**) [22]. It features a flexible 3D-printed frame and ankle support, which provides vertical support to prevent structural buckling. The device uses a bidirectional tendon drive to assist with plantarflexion and dorsiflexion movements. The robot also integrates a soft, wearable gait-sensing module that tracks the motion trajectory and pressure of both feet in real time, enabling feedback control. The system detects gait phases and accurately predicts timing, effectively promoting gait recovery and functional improvement in patients.

Hwang et al. designed an active ankle-foot orthosis (**Figure 6**) [23]. This device primarily consists of sensors, a controller, and actuators. The sensors use Force Sensing Resistor technology as switches to detect foot contact, with the output signals used to detect gait events and control the motor of orthosis system. A DC motor provides horizontal movement, and joint motion is adjusted by modifying the motor's speed and direction. The controller operates the actuator based on a defined control algorithm, enabling precise control over the dorsiflexion and plantarflexion movements of the ankle joint.

Sarma et al. designed and developed an electric ankle-foot orthosis (**Figure 7**) to improve ankle joint mobility in patients with foot drop and lower limb disabilities [24]. This orthosis, made of carbon fiber, includes a stepper motor that provides sufficient plantarflexion and dorsiflexion torque around the ankle joint. An Arduino controller manages the movement at the ankle joint. The motion capture system detects the body's movements during walking, and the motor-driven output voltage enables the motor to rotate, assisting in foot lifting and supporting patients in walking normally.

Kim et al. developed a pneumatic ankle-foot

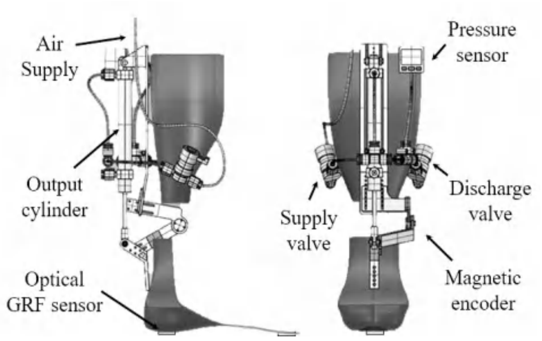

Figure 8. Pneumatic ankle foot orthotics. This figure is cited from [25].

Figure 9. Powered ankle exoskeleton robot. This figure is cited from [26].

Figure 10. Ankle exoskeleton robot. This figure is cited from [29].

orthosis (**Figure 8**), which generates a sufficient amount of pressurized air using an enhanced compressor to power a unilateral ankle-foot orthosis, assisting dorsiflexion in patients with foot drop [25]. A ground reaction force sensor detects different phases during the gait cycle, providing continuous analog output voltage. Throughout the gait cycle, the compressor activates according to the nominal rating, allowing the ankle to move freely during standing and enabling normal ankle joint movement.

Exoskeleton-type rehabilitation robot

Exoskeleton-type rehabilitation robots are designed to closely fit the surface of a patient's limbs, with a structure designed to match the human body model. These robots can safely and comfortably couple with limb movements, allowing for smooth and controlled motion. Depending on the settings, exoskeleton robots can provide passive, active-assistive, or active training, catering to the various rehabilitation needs of patients.

Tamburella et al. developed a powered ankle exoskeleton (**Figure 9**), an autonomous wearable robot designed to assist with ankle walking functions [26]. The device uses a neuromuscular controller to adjust the assistance provided by the robot based on the subject's specific capabilities. The system features linear actuators for precise force control and employs encoders, along with knowledge of the kinematic structure, to estimate the transmitted torque, which is then used for feedback in the torque control loop. For subjects with spinal cord injuries, the controller can generate human-like joint torque without the need to adjust their biomechanical or reflex parameters [27, 28].

Orekhov et al. developed a lightweight ankle exoskeleton (**Figure 10**) designed to improve the mobility of patients with neuromuscular impairments [29]. The exoskeleton uses carbon fiber materials to reduce weight and enhance long-term functionality. Force is transmitted through actuators and Bowden cables, providing personalized torque based on the patient's needs. Equipped with torque sensors, the exoskeleton provides feedback to the control system, ensuring precise tracking. During assisted walking, the exoskeleton reduces the activity of the soleus muscle and increases the self-selected walking speed, improving the efficiency of exoskeleton-assisted walking.

Gasparri et al. designed an ankle exoskeleton for walking assistance (**Figure 11**) [30]. The exoskeleton uses proportional joint torque control to instantly adapt to the biomechanical needs of the ankle joint. By providing assistance in proportion to the needs of the biological joint, the device estimates the user's joint

Figure 11. Cable powered ankle exoskeleton robot. This figure is cited from [30].

Figure 12. Reconfigurable ankle rehabilitation robot. This figure is cited from [31].

Figure 13. Electric series ankle exoskeleton robot. This figure is cited from [33].

torque in real-time. The exoskeleton torque synchronizes with the muscle demands at the joint, intuitively and safely capturing the user's intent. The robot uses a motor-driven system to assist with plantarflexion and dorsiflexion movements, with the ankle joint connected to a waist module via cables that transmit information.

Meng et al. designed a reconfigurable ankle rehabilitation robot (**Figure 12**) with an adjustable workspace capable of performing various types of ankle rehabilitation exercises [31]. The robot can be reconfigured by selecting different numbers of actuators, allowing for three single-degree-of-freedom movements, two-degree-of-freedom movements, and one three-degree-of-freedom movement. The adjustable design facilitates the interchangeability of the left and right feet. By changing the position of the sliders, the functional parts of the robot can be adjusted back and forth along the rails to accommodate users of different heights. The robot features a rotational center matching design, ensuring that the robot's rotational center closely aligns with the rotational center of ankle joint, preventing injuries during training. This robot meets the requirements for ankle rehabilitation training and offers practical usability [32].

Yeung et al. developed a portable ankle exoskeleton robot (**Figure 13**) with significant improvements in gait independence and walking speed [33]. The ankle joint is combined with a rotary motor and a torque amplifier, enabling both plantarflexion and dorsiflexion movements. In the power-assisted ankle robot mode, the device provides power to help patients with ground walking and stair training. It prevents foot drop through constant torque and calibrates in the dorsiflexion and plantarflexion directions as needed. In the swing control mode, the robot locks and unlocks the ankle joint during different gait phases, providing support to assist patients in their rehabilitation training.

Platform-type ankle-foot rehabilitation robots offer a wide range of motion and high safety by using a fixed base and a movable platform. These robots are suitable for patients at different stages of rehabilitation, as the platform can move in multiple directions to simulate natural ankle movements. Typically controlled by motors and sensors, platform-type robots allow for precise adjustment of the platform's movements. Orthotic-type robots, on the other hand, wrap around the patient's foot and ankle to provide external support and movement guidance. Compared to platform-type robots, orthotic devices have a limited range of motion but are lighter and can be adjusted according to the patient's specific needs, offering personalized rehabilitation training. Exoskeleton-type robots

Table 1. Comparison of different types of ankle rehabilitation robots

Type of Rehabilitation Robot	Advantages	Problems	Possible Solutions
Platform-Type	Providing a wide range of motion and high safety; easy to master and use; designed with comfort, enhancing patient experience	Accuracy limitations; difficult to control; limited application range; high demand for power and technical support	Introducing more precise sensors; increasing degrees of freedom; optimizing control algorithms
Orthotic-Type	Lightweight and portable; easy to customize; convenient for daily use; providing external support, reducing patient burden	Limiting patient mobility; unable to perform complex training; insufficient support for specific movements; inadequate support and power	Optimizing robot structure; introducing more efficient drive systems; increasing range of motion; developing additional support functions
Exoskeleton-Type	Highly adaptable; performing complex movements; offering high flexibility and power support; enhancing strength and facilitating rehabilitation	Complex design; heavy equipment; long wear times may cause fatigue; requiring substantial power support	Simplifying design; using lightweight materials; improving wear comfort; reducing fatigue; enhancing adaptability

are designed to accommodate various complex movement patterns to meet different rehabilitation requirements. They cover the patient's legs and feet, providing active motion support and using sensors and computer algorithms for precise motion control, offering additional force support to enhance rehabilitation training. Each type of rehabilitation robot has its own advantages and disadvantages, as shown in **Table 1**. Selecting the appropriate robot based on the patient's specific condition is key to achieving the best rehabilitation outcomes.

Ankle-foot rehabilitation robot control methods

Ankle-foot rehabilitation training is facilitated through the motion control system of an ankle-foot rehabilitation robot, with the specific control strategy chosen based on the rehabilitation goals. Based on different rehabilitation treatment needs, control strategies can be categorized into two types: active control and passive control. In active control, the robot provides appropriate assistance force and direction based on the patient's intentions and actual motor abilities, helping the patient complete the movement tasks. In passive control, the robot assists the patient by guiding them through a series of predefined rehabilitation exercises according to preset motion parameters. Passive control requires addressing issues such as uncertainties and disturbances that arise from the complex multi-joint structures of the robot and variations in load during movement.

Admittance control

In rehabilitation training, admittance control can adjust the robot's movement based on the forces exerted by the patient. Its primary goal is to control the robot's displacement based on external forces, ensuring its movement aligns with the desired dynamic characteristics. This approach provides flexible support during rehabilitation exercises, accommodating the patient's individual needs.

Siviy et al. developed a controller consisting of two nested control loops [34]. The inner loop performs closed-loop control of the motor speed in the drive system, tracking the desired cable speed trajectory generated by the outer loop. The outer loop includes two feedforward compensators for changes in Bowden cable position caused by joint movement and the forces generated by exoskeleton deformation. Force errors are compensated by a feedback admittance controller. The effect of dorsiflexion on stroke patients' ankles was assessed, optimizing offline assistance and separating positive and negative enhancement forces. Mu developed an improved rotary orthosis for arm-swing walking. In passive mode, the robot system implements a closed-loop position control algorithm [35]. In active mode, the ankle joint mechanism uses an adjustable admittance control algorithm, allowing patients to adjust the range of ankle joint motion. The system uses a series of linear actuators installed in front of the ankle joint to facilitate natural arm swinging. Force sensors at the actuator's end provide real-time force information to adjust the admittance control algorithm. The orthosis facilitates early-stage patients in regaining walking ability after injury.

Ren et al. developed a wearable rehabilitation robot for early rehabilitation training in stroke patients [36]. This robot combines video game-based training with admittance control, providing real-time feedback and adjustments by detecting resistance torque at the ankle joint.

The training, which includes 12 feedback-assisted isometric torque generation exercises along with both passive and active movements, promotes neuroplasticity and motor control. Chen et al. from Suzhou University designed an ankle exoskeleton robot with force feedback admittance control, which enhances human-robot interaction (HRI) compliance during walking assistance [37]. This system uses a cable-driven mechanism that adjusts the tension of the Bowden cable to control the assistive torque at the ankle. Admittance control provides better human-robot compliance while meeting control requirements.

Impedance control

In rehabilitation robots, impedance control ensures that the end-effector's impedance characteristics match the expected dynamic relationship, providing the desired compliance. This method primarily adjusts the system's response to external forces by modifying the control signals to achieve the desired impedance characteristics.

Liu et al. from Henan University of Science and Technology designed a pneumatic muscle redundant parallel-drive ankle rehabilitation robot [38]. They employed a compliance control strategy for active rehabilitation training, providing precise assistance and resistance during rehabilitation process. Based on impedance control theory, the system achieves error-free force tracking through trajectory planning. The combination of the control strategy and error-free force tracking guarantees both safety and compliance during assistance and resistance training.

Liu et al. developed an ankle rehabilitation platform to assist patients with ankle joint movements [39]. It consists of two symmetrical three-degree-of-freedom robotic platforms, with the robot's rotational center aligned with the patient's ankle joint center. This design allows patients to train the affected ankle joint by replicating the movements of the healthy ankle joint. The platform offers three training modes: constant-speed exercise, constant-torque impedance exercise, and conscious exercise. In constant-speed mode, the platform matches the input value. In constant-torque impedance mode, adjusting the torque threshold enables strength training for the ankle joint. In conscious mode, one side of the platform moves within the motion range. These modes support early neural rehabilitation for hemiparetic patients.

Perez-Ibarra developed an adaptive impedance control robot that is wearable and reversely driven [40]. It supports dorsiflexion, plantarflexion, inversion, and eversion within the normal range of motion. The robot's impedance control stiffness parameters are adjusted according to the patient's engagement level, guiding the patient through exercises with a game-based approach. The adaptive strategy allows for greater kinematic variability in the patient's movements. By monitoring the patient's performance during the game, the level of robotic assistance can be dynamically adjusted throughout the exercise.

Electromyographic (EMG) signal control

EMG signals provide rich information about human movement and accurately reflect neuromuscular activity. Using EMG signals as a control source for robots offers a promising control approach, as it enables the detection of movement intentions and the analysis of movement trajectories to and trigger control actions accordingly [41].

Researchers from the Shenyang Institute of Automation, Chinese Academy of Sciences, led by Zhang, developed an ankle rehabilitation robot based on adaptive control using EMG signals [42]. This robot assists patients in performing dorsiflexion and plantarflexion movements. The design simplifies the control process using a limit-based EMG model, while data-driven control methods address the uncertain dynamic characteristics of the robot system. By leveraging the antagonistic relationship between the tibialis anterior and the gastrocnemius muscles during ankle movements, the robot correlates the type of ankle movement with the contraction of individual muscle groups. The adaptive control algorithm ensures safety in HRI.

Ao et al. developed an EMG-driven Hill-type neuromuscular skeletal model [43]. This robot, featuring a single-degree-of-freedom powered exoskeleton, assists in ankle dorsiflexion. It can estimate ankle torque in real-time and accurately reflect changes in joint angles and muscle dynamics. Compared to linear proportional models, the Hill model improves predictions of joint torque at different joint angles. Patients using the Hill neuromuscular skeletal model expend less physical effort and exhibit smoother movements, as it reduces muscle co-contraction during the task, leading to more efficient rehabilitation.

Zhuang et al. designed an ankle rehabilitation robot based on EMG signal-guided admittance control [44]. This system consists of an EMG signal-driven musculoskeletal model, an admittance filter, and a position controller. Both the EMG signal-based admittance control scheme and open-loop control scheme improve the range of ankle motion in stroke patients. Proportional-derivative controllers enhance the stability of human-robot cooperation. The admittance control method provides stable and smooth tracking trajectories for assistive rehabilitation, making it suitable for implementation in portable assistive devices for robot-assisted walking.

Trajectory tracking control

Trajectory tracking control ensures that a robot's end-effector accurately follows a predefined trajectory, achieving high-precision movement control. The primary objective is to make sure the robot moves along a specified path while maintaining the expected speed and acceleration. During actual movement, real-time monitoring of the robot's position allows for the computation of error between the actual and desired trajectories.

Zhao et al. proposed a proportional-derivative control method based on deep deterministic policy gradient, which enhances the trajectory tracking accuracy of exoskeleton robots to ensure effective patient rehabilitation [45]. A degree of freedom was implemented at the robot's ankle joint to achieve dorsiflexion and plantarflexion movements. The gravity-compensated proportional-derivative control serves as the primary controller, effectively tracking the joint angles of the rehabilitation exoskeleton robot and enabling high-precision tracking control of joint angle trajectories.

Bae et al. designed a rehabilitation robot that employs trajectory tracking control as the main control method [46]. This method determines position control for each axis and utilizes force sensors on the footplate to measure ground reaction forces, compensating for vertical pelvic movements. Feedforward and feedback torque calculations drive the torques, with a feedforward torque compensation control module adjusting position, speed, and acceleration. Adjustments to the gravity compensation torque further improve control capabilities, and encoder feedback allows for real-time error tracking, aiding in the production of a standardized gait pattern for patients.

Jamwal et al. developed a parallel ankle rehabilitation robot, featuring a fixed platform and a moving platform connected by four linear flexible actuators [47]. The robot's optimal trajectory is generated by minimizing joint reaction torques and muscle-tendon unit tensions. Adjustments to the predetermined correct position errors, ensuring the robot moves in the opposite direction of these errors. Modifying the reference path can reduce the forces applied by the rehabilitation robot, and speed limits on path adaptation help maintain system stability.

Ai et al. from Wuhan University of Technology developed a pneumatic muscle-driven flexible ankle rehabilitation robot [48]. They implemented an adaptive backstepping sliding mode control method to addresses nonlinear characteristics and uncertainties in the human-robot rehabilitation process. This approach can estimate external disturbances online, enhancing the robustness of the control method and allowing real-time adjustments to control outputs, achieving high trajectory tracking accuracy. This control method reduces oscillations, thereby minimizing further harm to patients.

Proportional-Integral-Derivative (PID) control

PID control provides precise control of a system by adjusting control parameters to track a set target. It is characterized by its adjustable dynamic properties and does not rely on the model of the controlled object. Adjusting the system parameters can yield satisfactory control effects.

Nhon et al. proposed a resonant method based on PID control, which uses an interval type-2 fuzzy self-tuning PID controller to improve system control accuracy [49]. Compared to traditional PID controllers, fuzzy PID controllers demonstrate superior stability and robustness against external disturbances and exhibit faster response speeds. Type-2 fuzzy logic is particularly effective for managing complex and uncertain systems. Fuzzy logic controllers apply fuzzy set theory to manage uncertainties and nonlinearities in the system, allowing for more adaptable control strategies.

Wang et al. from Northeastern University designed a 3-SPS/S (spherical-prismatic-spherical/spherical) parallel ankle rehabilitation robot, combining fuzzy inference systems with traditional PID control to develop a fuzzy adaptive PID controller that enhances control system accuracy [50]. The robot's control module generates algorithmic control quantities based on feedback deviations to control the system. The trajectory generation module computes the movement trajectories of each limb based on the desired pose, while the sensing module

Table 2. The advantages and disadvantages of different control methods

Control methods	Advantages	Disadvantages
Admittance control	Provides compliance, enables precise force control, and adapts to constantly changing external forces or disturbances.	Requires precise parameter selection for effective performance and may struggle to maintain stability in high-stiffness scenarios.
Impedance control	Provides stable force feedback, and allows for easy integration of force and position control by adjusting impedance parameters.	Performance may be less agile in environments with large external forces or significant dynamic changes; requires high-performance actuators.
Electromyographic signal control	Provides immediate muscle activity feedback, enabling quick response to user intentions and adaptability to varying muscle activity patterns and enhancing flexibility.	Susceptible to noise and interference; muscle fatigue can alter electromyographic signals, potentially affecting system stability and control performance.
Trajectory tracking control	Improves overall system accuracy by reducing errors and deviations; accommodates various task requirements with customizable trajectories.	Requires complex computations and real-time processing; high computational loads may delay system response and depend on the accuracy.
Proportional-integral -derivative control	Effectively reduces steady-state errors and offers good robustness through adjustable proportional, integral, and derivative parameters.	May require additional adjustments or extended control strategies for time-varying or complex dynamic systems.

gathers information such as the platform's position and speed.

Lb et al. from East China University of Science and Technology developed a hybrid active-passive ankle prosthesis, which uses a combination of series and parallel springs to meet the impedance requirements at different ankle positions during walking [51]. Series springs adjust the impedance dynamically, while parallel springs serve as energy storage components. The prosthesis controller collects joint angle and torque data and uses a finite state machine to determine the gait phase of the ankle joint, outputting appropriate angles or torques. Different controllers are selected based on the detected gait to meet the complex movement needs of the ankle joint. Cui et al. from Shanghai Jiao Tong University designed a flexible ankle rehabilitation robot, which uses soft actuators, calf, and foot fixtures that are 3D-printed for lightness and practicality [52]. The robot's symmetrical pneumatic soft actuators enable dorsiflexion and plantarflexion movements. PID control methods are used to manage the robot's drive angles, with a feedback closed-loop control system constructed based on hardware devices, such as posture sensors, to achieve ankle rehabilitation training [53].

The signals generated by the human body are transmitted to the robot, allowing the selection of a control strategy based on rehabilitation needs. Each control method offers unique characteristics, as summarized in **Table 2**.

Key Technologies in Ankle-foot rehabilitation robots

HRI technology

HRI technologies enable efficient and natural interactions between humans and robots, primarily achieved through control systems, feedback mechanisms, and artificial intelligence. By leveraging the robot's strong capabilities in perceiving, acquiring, and processing biological and environmental information, and combining the human brain's exceptional decision-making ability in unfamiliar and complex situations, HRI enables a complementary advantage between humans and robots. In rehabilitation robots, HRI technologies are mainly implemented through the monitoring of physiological signals and force and position information [54].

Shi et al. developed a rehabilitation robot based on a HRI dynamics model [55]. The adaptive controller in the robot system can handle uncertainties in the stiffness coefficients of the robot's parameters and force models. A three-dimensional equivalent spring model is used to represent the interaction forces between the human and the robot, simulating the torque applied by the robot to the body. The robot addresses the limitation of recognizing patients' movement intentions due to their limited voluntary control during rehabilitation, thereby improving patient comfort.

Du et al. proposed an adaptive HRI control strategy for rehabilitation robots [56]. Based on a dynamic model, they extract surface electromyographic signals and plantar pressure features to identify movement intentions. The developed HRI information fusion model enables real-time planning of the robot's movement trajectory. An adaptive fuzzy controller enables trajectory tracking and implements adaptive HRI control for the robot.

Sensor technology

Sensor technologies play a crucial role in ensuring the adaptability and safety of rehabilitation robots. Sensors and perception devices are strategically integrated into various parts of the robot to collect data on physiological state, movement, joint velocities, and torques. The accuracy of this data directly impacts the stability and performance of the entire robotic system. Currently, multi-sensor perception systems are employed to integrate signals for more accurate gait information [57]. These systems track body posture, predict movement intentions, and monitor the physiological state of patients during rehabilitation, providing objective data for clinicians.

Yang et al. designed a rehabilitation robot based on force-torque sensing and teaching, which allows for personalized and diverse rehabilitation training for different patients [58]. A six-dimensional force sensor is installed at the ankle end to detect external contact forces. By implementing a compliance control algorithm and analyzing the robot's pose matrix, inverse kinematics modules are used to determine the joint angles, enabling the robot to follow the desired trajectory. Gao et al. developed a multi-functional rehabilitation robot capable of sitting, lying, and standing. Angle sensors are installed on the backrest and seat to measure the real-time inclination angles at the control terminal [59]. A six-dimensional force sensor at the foot collects torque information from the patient's foot, aiding clinicians in understanding the patient's condition better. Proximity sensors in the leg extension module offer non-contact detection, contributing to enhanced safety and performance during rehabilitation exercises. Zhang et al. designed a rehabilitation robot based on motion injuries [60]. The control system includes torque sensors at the output end of the motor drivers, which provide force feedback information during active training. This facilitates real-time adjustment of impedance values, improving the effectiveness of the rehabilitation process.

Muro-de-la-Herran utilized inertial sensors in gait analysis, primarily to measure angles and assess patient conditions throughout the entire gait cycle [61]. A wearable rehabilitation exoskeleton robot developed by the University of Twente in the Netherlands uses motors to drive the ankle joint movements, enabling paraplegic patients to walk without obstacles, maximizing comfort and adaptability [62]. The robot is equipped with a multi-control strategy system that adjusts overall walking control based on shifts in the body's center of gravity, which occur due to forward and lateral tilting during walking. The accuracy of the control is monitored using encoders and gravity sensors on the device.

Sensor technology plays a crucial role in detecting and transmitting subtle signals, making judgments based on the collected data to ensure that rehabilitation robots perform appropriate actions. This technology is advancing towards greater intelligence and efficiency. In human-machine interaction, software is becoming increasingly user-friendly, with new technologies enhancing the interactivity between humans and machines. Future software will significantly improve its practicality, leading to better patient experience.

Conclusion and Outlook

Rehabilitation robot provides a significant technological avenue for alleviating current healthcare challenges and enhancing training levels, offering substantial social value. Rehabilitation robots show promising prospects in the recovery of stroke patients, significantly improving upper limb, lower limb, and cognitive functions. Compared to traditional rehabilitation training, rehabilitation robots offer more stable and controllable training, ensuring optimal rehabilitation intensity and efficiency. They not only provide scientifically effective rehabilitation training to accelerate patient recovery but also address the shortage of rehabilitation therapists.

Current advancements in rehabilitation robotics reveal a range of promising technologies, each with distinct advantages and challenges. End-effector robots have simple structures and are easy to manufacture but suffer from kinematic mismatches with limb joints, limiting their ability to control multiple joints simultaneously and restricting their range of motion. Although exoskeleton rehabilitation robots offer good compliance, comfort, and portability, they lack external rigid frameworks, making the installation of motors and sensors challenging, and limiting their functional diversity and support capabilities. Future research may focus on combining rigidity with flexibility. Regarding control strategies, current systems utilize a variety of methods, often in combination, to harness the strengths of each approach and address the weaknesses of individual techniques. Future research is expected to increasingly adopt hybrid control methods.

Currently, the structure of rehabilitation robots mainly consists of traditional materials such as metals and alloys, which results in larger sizes that impacts patient comfort, thereby affecting rehabilitation therapy. The shift towards lightweight materials will improve comfort and structural efficiency. Rigid joint-based rehabilitation robots have limited movement and cannot achieve continuous deformation. The use of flexible materials such as elastomers can effectively absorb impact energy, representing an important direction for future development. A advancements in artificial intelligence, when combined with rehabilitation robots will make patient rehabilitation training more intelligent and safer, representing a key trend in future developments. Research into rehabilitation robots holds significant social implications and broad application prospects.

Author Contributions: Hongtao Shen contributed to the conception of the study and performed the discussion and wrote the manuscript. Qingyun Meng gave instruction and revision of manuscript writing. Mingxia Wei, Jiajia Zha reviewed the content of the manuscript.

References

[1] Caplan LR, Simon RP, Hassani S. Chapter 27 - Cerebrovascular disease—stroke∗. In: Zigmond MJ, Wiley CA, Chesselet M-F, editors. Neurobiology of Brain Disorders (Second Edition). Academic Press, 2023. p. 457-476.

[2] Shahbazi M, Atashzar SF, Tavakoli M, et al. Robotics-assisted mirror rehabilitation therapy: A therapist-in-the-loop assist-as-needed architecture. IEEE/ASME Trans Mechatron 2016;21(4):1954-1965.

[3] Lamers I, Maris A, Severijns D, et al. Upper limb rehabilitation in people with multiple sclerosis: a systematic review. Neurorehabil Neural Repair 2016;30(8):773-793.

[4] Mandeville RM, Brown JM, Sheean GL. A neurophysiological approach to nerve transfer to restore upper limb function in cervical spinal cord injury. Neurosurg Focus 2017;43(1):E6.

[5] Yang HM. New trend of population aging in China and new characteristics of the elderly population. Popul Res 2022;46(05):104-116.

[6] Krebs HI, Dipietro L, Levy-Tzedek S, et al. A paradigm shift for rehabilitation robotics. IEEE Eng Med Biol Mag 2008;27(4):61-70.

[7] Chen M. Application of exercise therapy and acupuncture treatment in the rehabilitation of hemiplegia after stroke. Chin Sci Technol J Database (full text version) Med Health 2016;142.

[8] Yang C, Long J, Urbin MA, et al. Real-time myocontrol of a human–computer interface by paretic muscles after stroke. IEEE Trans Cognit Dev Syst 2018;10(4):1126-1132.

[9] Williams MR. A pilot study into reaching performance after severe to moderate stroke using upper arm support. Plos one 2018;13(7):e0200787.

[10] Yang Y, Sinha N, Tian R, et al. Quantifying altered neural connectivity of the stretch reflex in chronic hemiparetic stroke. IEEE Trans Neural Syst Rehabil Eng 2020;28(6):1436-1441.

[11] Su F, Xu W. Enhancing brain plasticity to promote stroke recovery. Front Neurol 2020;11:554089.

[12] Liu L, Chen W, Zhou H, et al. Chinese Stroke Association guidelines for clinical management of cerebrovascular disorders: executive summary and 2019 update of clinical management of ischaemic cerebrovascular diseases. Stroke Vasc Neurol 2020;5(2):159-176.

[13] Zeng X, Zhu G, Zhang M, et al. Reviewing Clinical Effectiveness of Active Training Strategies of Platform□Based Ankle Rehabilitation Robots. J Healthc Eng 2018;2018(1):2858294.

[14] Li J, Zhang Z, Tao C, et al. A number synthesis method of the self-adapting upper-limb rehabilitation exoskeletons. Int J Adv Robot Syst. 2017;14(3):1729881417710796.

[15] Mehrholz J, Platz T, Kugler J, et al. Electromechanical and robot-assisted arm training for improving arm function and activities of daily living after stroke. Stroke 2009;40(5):e392-e393.

[16] Yuan RP, Tang CZ, Jiang Y, et al. Research progress on the role and mechanism of upper limb rehabilitation robots in promoting the recovery of upper limb function after stroke. Chin J Cerebrovasc Dis 2022;19(07):509-513.

[17] Dworzynski K, Ritchie G, Playford ED. Stroke rehabilitation: long-term rehabilitation after stroke. Clin Med 2015;15(5):461-464.

[18] Zuo S, Li J, Dong M, et al. Design and performance evaluation of a novel wearable parallel mechanism for ankle rehabilitation. Front Neurorobot 2020;14:9.

[19] Nurahmi L, Caro S, Solichin M. A novel ankle rehabilitation device based on a reconfigurable 3-RPS parallel manipulator. Mech Mach Theory 2019;134:135-150.

[20] Abu-Dakka FJ, Valera A, Escalera JA, et al. Passive exercise adaptation for ankle rehabilitation based on learning control framework. Sensors 2020;20(21):6215.
[21] Lu Y, Zhang X, Ai Q. Mechanism Design and Analysis of a Multi-DOF Flexible Ankle Rehabilitation Robot. J Phys: Conf Ser 2021;1884(1):012038.
[22] Kwon J, Park J-H, Ku S, et al. A soft wearable robotic ankle-foot-orthosis for post-stroke patients. IEEE Rob Autom Lett 2019;4(3):2547-2552.
[23] Hwang S, Kim J, Kim Y. THE EFFECTS OF THE WALKING WITH AN ACTIVE ANKLE FOOT ORTHOSIS: A HEMIPLEGIC PATIENT. J Biomech 2007;40(2):S450.
[24] Sarma T, Saxena KK, Majhi V, et al. Development of active ankle foot orthotic device. Mater Today: Proc 2020;26:918-921.
[25] Kim SJ, Park J, Shin W, et al. Proof-of-concept of a Pneumatic Ankle Foot Orthosis Powered by a Custom Compressor for Drop Foot Correction. 2020 IEEE Int Conf Robot Autom 2020;747-753.
[26] Tamburella F, Tagliamonte N, Pisotta I, et al. Neuromuscular controller embedded in a powered ankle exoskeleton: Effects on gait, clinical features and subjective perspective of incomplete spinal cord injured subjects. IEEE Trans Neural Syst Rehabil Eng 2020;28(5):1157-1167.
[27] Wu AR, Dzeladini F, Brug TJ, et al. An adaptive neuromuscular controller for assistive lower-limb exoskeletons: A preliminary study on subjects with spinal cord injury. Front Neurorobot 2017;11:30.
[28] Dzeladini F, Wu AR, Renjewski D, et al. Effects of a neuromuscular controller on a powered ankle exoskeleton during human walking. 2016 6th IEEE International Conference on Biomedical Robotics and Biomechatronics (BioRob) 2016;617-622.
[29] Orekhov G, Fang Y, Luque J, et al. Ankle exoskeleton assistance can improve over-ground walking economy in individuals with cerebral palsy. IEEE Trans Neural Syst Rehabil Eng 2020;28(2):461-467.
[30] Gasparri GM, Luque J, Lerner ZF. Proportional joint-moment control for instantaneously adaptive ankle exoskeleton assistance. EEE Trans Neural Syst Rehabil Eng 2019;27(4):751-759.
[31] Meng Q, Liu G, Xu X, et al. A multi-degree-of-freedom reconfigurable ankle rehabilitation robot with adjustable workspace for post-stroke lower limb ankle rehabilitation. Front Bioeng Biotechnol 2023;11:1323645.
[32] Meng Q, Liu G, Xu X, et al. Design and analysis of a supine ankle rehabilitation robot for early stroke recovery. Machines 2023;11(8):787.
[33] Yeung L-F, Lau CC, Lai CW, et al. Effects of wearable ankle robotics for stair and over-ground training on sub-acute stroke: a randomized controlled trial. J Neuroeng Rehabil 2021;18(1):19.
[34] Siviy C, Bae J, Baker L, et al. Offline assistance optimization of a soft exosuit for augmenting ankle power of stroke survivors during walking. IEEE Robot Autom Lett 2020;5(2):828-835.
[35] Mu Z, Zhang Q, Yang G-Y, et al. Development of an improved rotational orthosis for walking with arm swing and active ankle control. Front Neurorobot 2020;14:17.
[36] Ren Y, Wu Y-N, Yang C-Y, et al. Developing a wearable ankle rehabilitation robotic device for in-bed acute stroke rehabilitation. EEE Trans Neural Syst Rehabil Eng 2017;25(6):589-596.
[37] Chen D, Li WD, Zhang HM, et al. Flexible ankle exoskeleton based on force feedback admittance control. J Zhejiang Univ (Eng Sci) 2024;58(04):772-778.
[38] Liu YB, Pang XY, Zhang YB, et al. Research on Active Training and Flexibility Control of Ankle Rehabilitation Robot. J Syst Simulation 2020;32(01):54-60.
[39] Liu Q, Wang C, Long JJ, et al. Development of a new robotic ankle rehabilitation platform for hemiplegic patients after stroke. J Healthc Eng 2018;2018(1):3867243.
[40] Perez-Ibarra JC, Siqueira AA, Silva-Couto MA, et al. Adaptive impedance control applied to robot-aided neuro-rehabilitation of the ankle. IEEE Robot Autom Lett 2018;4(2):185-192.
[41] Kamavuako EN, Scheme EJ, Englehart KB. Combined surface and intramuscular EMG for improved real-time myoelectric control performance. Biomed Signal Process Control 2014;10:102-107.
[42] Zhang B, Yao J, Zhao XG, et al. An adaptive human-computer interaction control method based on electromyographic signals. Control Theory Appl 2020;37(12):2560-2570.
[43] Ao D, Song R, Gao J. Movement performance of human–robot cooperation control based on EMG-driven hill-type and proportional models for an ankle power-assist exoskeleton robot. IEEE Trans Neural Syst Rehabil Eng 2016;25(8):1125-1134.
[44] Zhuang Y, Leng Y, Zhou J, et al. Voluntary control of an ankle joint exoskeleton by able-bodied individuals and stroke survivors using EMG-based admittance control scheme. IEEE Trans Biomed Eng 2020;68(2):695-705.
[45] Zhao ZR, Tao Q, Yang T, et al. Trajectory tracking control of lower limb rehabilitation robot based on DDPG. Mach Tool Hydraul 2023;51(11):13-19.

[46] Bae E, Park S-E, Moon Y, et al. A robotic gait training system with stair-climbing mode based on a unique exoskeleton structure with active foot plates. Int J Control, Autom Syst 2020;18(1):196-205.
[47] Jamwal PK, Hussain S, Tsoi YH, et al. Musculoskeletal model for path generation and modification of an ankle rehabilitation robot. IEEE Trans Hum Mach Syst 2020;50(5):373-383.
[48] Ai Q, Zhu C, Zuo J, et al. Disturbance-estimated adaptive backstepping sliding mode control of a pneumatic muscles-driven ankle rehabilitation robot. Sensors 2017;18(1):66.
[49] Nhon P, Elamvazuthi I, Fayek H, et al. Intelligent control of rehabilitation robot: Auto tuning PID controller with interval type 2 Fuzzy for DC servomotor. Procedia Comput Sci 2014;42:183-190.
[50] Wang HF, Chen XB, Jiao L, et al. Simulation of Fuzzy Adaptive Control System for 3-SPS/S Ankle Rehabilitation Mechanism. Chin J Constr Mach 2021;19(03):238-243+249.
[51] Lb RA, Cao H, Zhu J, et al. Study on hybrid force/position control of active and passive ankle joint prostheses. J East China Univ Sci Technol 2018;44(02):283-288.
[52] Cui X, Wang YX, Wang WB, et al. Design and Control of Flexible Ankle Rehabilitation Robot. Mach Des Res 2023;39(06):1-5+16.
[53] Li SY, Han YL, Chen RW, et al. Research on lower limb rehabilitation exoskeleton control based on sliding mode PID control. Modular Mach Tool Autom Manuf Tech 2021;(03):98-101+105.
[54] Cheng H, Huang R, Qiu J, et al. Review of research progress on human-machine intelligence technology and systems. CAAI Trans Intell Syst 2020;15(02):386-398.
[55] Shi D, Zhang W, Zhang W, et al. Human-centred adaptive control of lower limb rehabilitation robot based on human–robot interaction dynamic model. Mech Mach Theory 2021;162:104340.
[56] Du YH, Qiu S, Xie P, et al. Adaptive human-machine interaction control strategy for lower limb rehabilitation robots. Acta Autom Sin 2018;44(04):743-750.
[57] Li LF, Zhu LY, Gou XF. Research Status and Development Trends of Wearable Lower Limb Exoskeleton Rehabilitation Robots. Chin Med Equip J 2019;40(12):89-97.
[58] Yang H, Han JH, Li XP. Research on Force Sensing and Dragging Teaching of Horizontal Lower Limb Rehabilitation Training Robot. Mach Des Manuf 2020;(05):272-275.
[59] Gao S. Research on a sit lie stand retractable lower limb rehabilitation robot mechanism. Yanshan University 2021.
[60] Zhang YQ. Research on the mechanism design of sports injury rehabilitation robot. Beijing Institute Of Petrochemical Technology 2020.
[61] Muro-De-La-Herran A, Garcia-Zapirain B, Mendez-Zorrilla A. Gait analysis methods: An overview of wearable and non-wearable systems, highlighting clinical applications. Sensors 2014;14(2):3362-3394.
[62] Wang S, Dijk Wv, Kooij Hvd. Spring uses in exoskeleton actuation design. 2011 IEEE International Conference on Rehabilitation Robotics 2011;1-6.

Progress in Medical Devices
ISSN: 2957-5478

Zentime

Review Article https://doi.org/10.61189/164995qvdasw

Gait prediction for lower limb exoskeleton robots based on real-time adaptive Kalman filtering

Haonan Geng[1], Xudong Guo[1], Fengqi Zhong[2], Haibo Lin[1], Guojie Zhang[3], Qin Zhang[4], Jiaheng Chen[1]

[1]School of Health Science and Engineering, University of Shanghai for Science and Technology, Shanghai 200093, China. [2]CloudSemi, Pudong New Area, Shanghai 200120, China. [3]LingYuan Iron and Steel CO., LTD, Lingyuan 122500, Liaoning Province, China. [4]Medical Engineering Department of Northern Jiangsu People's Hospital, Yangzhou 225001, Jiangsu Province, China.

Corresponding author: Xudong Guo.

Declaration of conflict of interest: None.

Received September 29, 2024; Accepted December 3, 2024; Published March 31, 2025

Highlights

- The paper develops a gait prediction control strategy for lower limb exoskeleton robots using a real-time adaptive Kalman filtering algorithm, with public gait data from a Clinical Gait Analysis serving as input.
- The model incorporates motor rotation angle, angular velocity, and angular acceleration as core parameters, calculated based on the principles of uniformly accelerated motion. It achieves gait prediction by initializing parameters, calculating Kalman gain, correcting measurements, and updating the covariance matrix.
- A control strategy guided by normal gait parameters enables the exoskeleton to transition efficiently into the desired motion state during startup and gait phase switching. The system employs a microcontroller and Raspberry Pi as its control core, integrated with Bluetooth communication for effective robot control.

Abstract

This paper presents a gait prediction method for lower limb exoskeleton robots using a real-time adaptive Kalman filtering algorithm. The exoskeleton robot targets two user groups: individuals with impaired lower limb motor function requiring rehabilitation training, where the device aids in muscle exercise during walking to facilitate recovery, and healthy individuals using it as a wearable assistive device. To enhance movement intention prediction and improve human-machine coordination, this study focuses on the gait prediction algorithm for walking assistance in healthy users and proposes a gait prediction control strategy based on normal gait orientation. The control system utilizes a microcontroller and Raspberry Pi as its core, enabling functional mode selection through multi-sensor data fusion and effective control of the robot via Bluetooth communication. By comparing the original model algorithm with the proposed real-time updating Kalman filter algorithm, the latter demonstrates feasibility, achieving a prediction error within 1°. This validates the model's effectiveness in real-time gait prediction.

Keywords: Gait prediction, lower limb exoskeleton robot, Kalman filtering

Introduction

Currently, lower limb exoskeleton robots are designed for two primary user groups. The first group includes individuals with impaired lower limb motor function who require rehabilitation. These exoskeletons simulate normal walking gait, assist patients in exercising their leg muscles, and facilitate the recovery of motor functions [1]. The second group includes healthy individuals, where exoskeletons serve as wearable booster devices in fields such as the military, industry, and first aid [2]. These devices enhance user functionality by reducing weight-bearing strain and physical exertion [3].

Commercially mature exoskeletons primarily focus on rehabilitation and employ relatively simple motion control systems. In contrast, exoskeletons for healthy users require real-time stability and improved human-machine interaction, imposing more stringent demands on mo-

Address correspondence to: Xudong Guo, School of Health Science and Engineering, University of Shanghai for Science and Technology, No.516 Jungong Road, Shanghai 200093, China. Email: guoxd@usst.edu.cn.

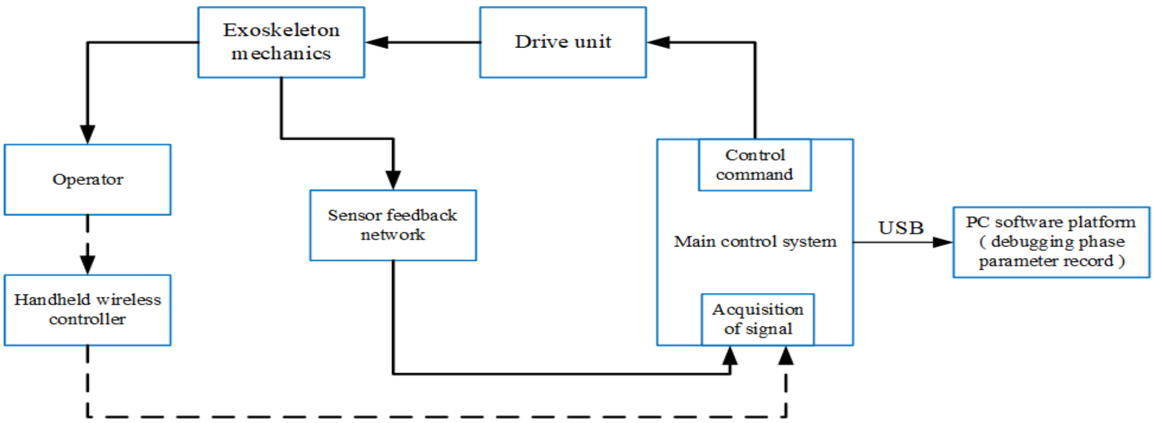

Figure 1. Schematic diagram of the overall composition of the exoskeleton system.

tion control. Qu et al. studied the phase division of normal human gait and proposed dividing motion control into two phases: assisting and following. The control system was developed using fuzzy impedance control and position control based on gait trajectory, with input parameters provided by attitude angle sensors and pressure sensors [4]. Song explored gait predictive control using Kalman filtering and Gradient Boosting algorithms to predict changes in joint angles during robot motion [5]. This approach integrates intelligent modules to estimate current joint angles and predict subsequent changes, enabling precise robot control.

The Hybrid Assistive Limb robot, developed by Cyberdyne in Japan, weighs 23 kg, has a 160-minute endurance, and offers two control systems: bioconscious control and autonomous conscious control [6, 7]. The bioconscious control system captures electromyographic signals to infer the user's movement intentions, while the autonomous control system uses prestored models to perform assisted movements. Kadone et al. evaluated the HAL robot's effectiveness in patients with gait disorders caused by compressive myelopathy, demonstrating improved gait and restored joint contours after training [8].

Kalman filters have also been widely applied in other domains. For example, Wang et al. used Kalman filtering to process correlated noise and estimate pitch angles [9]. Fan et al. applied a Kalman filter fusion algorithm to eliminate noise and clutter in sowing depth measurements, resulting in more accurate detection data [10]. Li proposed an optimization method based on Kalman filter sensor data fusion, which improved stability, anti-interference capability, and reliability even when some equipment failed [11].

The objective of this project is to develop a wearable exoskeleton robot for assisting healthy individuals during walking. This robot aims to accurately predict the user's movement intentions and provide effective assistance. The control system will use a microcontroller as the central module and integrate multi-sensor data fusion to achieve human-robot synergy. By combining sensing, electromechanical control, information detection, and artificial intelligence, the project seeks to deliver an intelligent wearable assistive device that meets user needs.

Structural design of a lower limb exoskeleton system

The lower limb exoskeleton assistive robot has been independently designed and developed, with its overall configuration illustrated in **Figure 1**. The mechanical structure mainly comprises a sliding hip joint with adaptive length adjustment, a multi-link bionic knee joint, and an electrically controlled backpack module [12-14]. The exoskeleton combines actively powered hip joints with passively assisted knee joints, improving the operator's active control, reducing energy consumption, and extending battery endurance.

As in **Figure 2**, the mechanically adaptive leg features a hip joint transmission module, a bionic knee joint linkage module, ankle and foot components, and additional accessories such as bearings and clasps. The hip joint transmission module includes a disc motor, motor tray, coupling, harmonic reducer, and a disc torque sensor, which is secured using screws. The mechanical leg employs a nested composite design with adjustable and lockable lengths, allowing it to accommodate users of varying heights. By controlling the rotation of the disc motor, electric energy is converted into kinetic energy, pushing the thigh rod to assist movement.

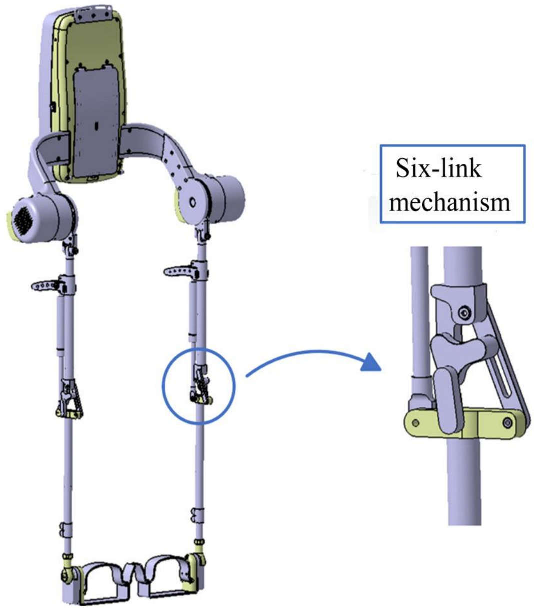

Figure 2. 3D modeling of the exoskeleton robot.

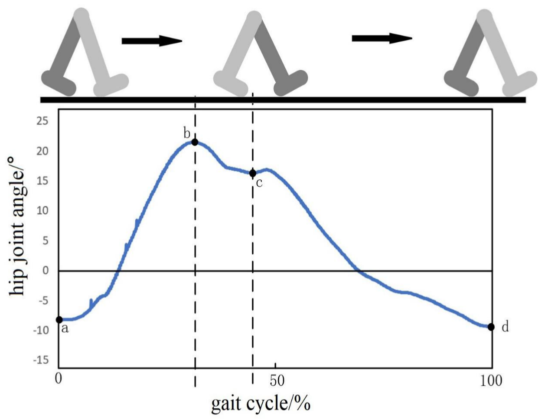

Figure 3. Angular variation curve of the hip joint during a single gait cycle.

The bionic knee joint module features a passive six-link mechanism integrated with an air spring. The air spring stores kinetic energy during knee flexion and releases it during extension, providing a boost to movement. The ankle joint is equipped with an active joint capable of 360° rotation. The footplate connects to the joint via a nested structure, and both components are height-adjustable to adapt to user-specific needs. The unilateral leg, there are 3 degrees of freedom at the hip joint, 1 degree of freedom at the knee joint, and 1 degree of freedom at the ankle joint.

Design of control system for gait prediction based on Kalman filtering

Gait analysis and control scheme design

Normal gait refers to the walking posture that minimizes body energy consumption while maintaining maximum comfort [15]. Gait analysis, a biodynamic research method, studies the human walking process using mechanical principles, specialized treatments, and knowledge of anatomy and physiology [16]. Simplifying the human body into a linkage model facilitates dynamic analysis of motion and force interactions [17]. **Figure 3** shows the angular variation curve of the hip joint during a single gait cycle in normal walking. The curve begins at the initial state (a), where the heel of the right leg contacts the ground, and the left leg's heel is about to lift off, and ends at state (d), where the right leg's heel contacts the ground again. Point b represents the critical transition point where the left leg changes direction, and point c marks the start of left leg support.

The analysis of the gait cycle and hip joint angular variation serves as the foundation for defining the functional requirements of the exoskeleton control system. First, the starting posture and movement speed must be determined. In this study, the two-legged standing position is used as the initial state, and the angular changes in normal gait are utilized to calculate the corresponding movement speeds. This ensures that the robot can rapidly transition into the assistive and following modes. When the motion reaches point b, the exoskeleton must react promptly to change direction and either follow or assist the backward movement of the human leg. At point c, the exoskeleton is required to transfer the user's center of gravity to the supporting leg while assisting the swing leg's motion.

The intelligent control system is designed with a microcontroller as its core, enabling precise control of each joint motor via programmed instructions. The system reads motor parameters and sensor data to determine the motion state of the exoskeleton and performs closed-loop feedback for adjustment and control. Additionally, the system integrates a microprocessor and an electromyography acquisition module to capture the user's leg electromyography signals. These signals are processed to detect the user's movement intentions, assisting the main control system in guiding the robot to the appropriate movement state. The overall design scheme of the exoskeleton control system is depicted in **Figure 4**.

To ensure the normal operation of the robot, a handheld control switch transmits control commands via wireless Bluetooth to manage functions such as startup and reset, ensuring user safety during robot use. The switch conveys

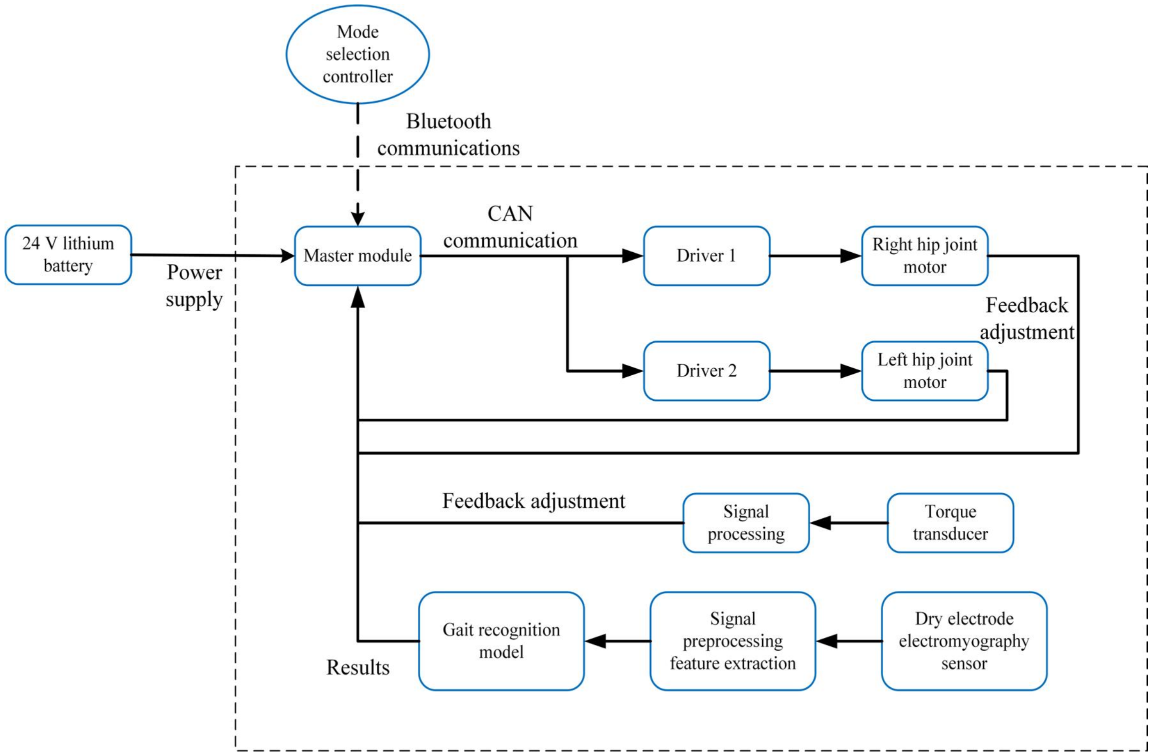

Figure 4. General design scheme of the exoskeleton control system. CAN, Controller Area Network.

commands to the main control module, which analyzes the inputs and transmits corresponding control signals to the joint motor drivers. The motors then execute these commands, enabling the exoskeleton robot to function effectively. During operation, the system primarily controls the speed of each joint motor to provide assistance. Real-time acquisition of motor rotation angles and human-machine interaction data, obtained from torque sensors, allows for precise speed adjustments, reducing resistance and improving control accuracy, safety, and stability.

The exoskeleton robot's control system is built on a comprehensive hardware platform comprising various modules. Key components include:

Power Supply Unit: A lithium battery ensures portability, freeing the system from location constraints.

Main Control Module: Based on the STM32F4 series minimum system, this serves as the core processing unit.

Joint Motors and Drives: Facilitate the robot's movements.

Sensors: Torque sensors provide critical feedback for regulation and control.

Auxiliary System: Built on a Raspberry Pi 4B microcomputer, enabling intention recognition.

These hardware elements collectively form the foundation for implementing the exoskeleton control platform.

Gait prediction based on real-time updated Kalman filtering

Design of the real-time updated Kalman filter gait prediction process

The Kalman filtering algorithm, proposed by R.E. Kalman in 1960, is a recursive filter widely used for solving linear filtering problems in discrete data [18]. It estimates the state of a dynamic system from noisy measurements, minimizing mean-square estimation error, and has been extensively applied across various engineering fields [19-21].

The algorithm consists of two phases: prediction and update [22].

Prediction Phase: The algorithm predicts the system state at the next moment using the prior optimal state estimation and the system model.

Update Phase: The Kalman gain is calculated, allowing the algorithm to compare the predicted value with newly obtained measurements and refine the state estimate for improved accuracy [23].

The core principle involves predicting the state at the Kth moment using the best estimate from the (K-1)th moment. This prediction is then corrected based on observations at the Kth moment, producing a more accurate estimate [24].

In this study, predictive control of robot motion is implemented using a real-time updated Kalman filter algorithm, with Clinical Gait Analysis data as input. The motion of the robot is primarily determined by motor parameters such as rotation angle, angular velocity, and angular acceleration, calculated based on the principle of uniformly accelerated motion. The detailed construction process of the prediction model is presented as shown below.

The predictive control process using a real-time updated Kalman filter consists of the following steps:

Inputs: Measurement parameter matrix

$$x = \begin{bmatrix} \theta \\ \omega \end{bmatrix}, \quad Q = \begin{bmatrix} D(\theta) & 0 \\ 0 & D(\omega) \end{bmatrix} \quad R = \begin{bmatrix} r_1 & r_2 \\ r_3 & r_4 \end{bmatrix}$$

where *Q* and *R* are adjustable parameters.

Outputs: Predictive matrix $y = \begin{bmatrix} \theta \\ \omega \end{bmatrix}$

1. Initialization parameters:

$$H = \begin{bmatrix} 1 & 0 \\ 0 & 1 \end{bmatrix}, \quad A = \begin{bmatrix} 1 & \Delta t \\ 0 & 1 \end{bmatrix}, \quad B = \begin{bmatrix} \frac{1}{2}\Delta t^2 \\ \Delta t \end{bmatrix}, \quad P = \begin{bmatrix} p_1 & p_2 \\ p_3 & p_4 \end{bmatrix}$$

Initially, all elements are set to zero, and angular acceleration a is considered.

2. Calculation of the current initial Kalman gain at Time :

$$k = \begin{bmatrix} k_1 & k_2 \\ k_3 & k_4 \end{bmatrix} = \frac{P(k) * H^T}{H * P(k) * H^T + R}$$

3. Correction of the measurement value at Time :

$$x(k) = x(k-1) + K * (y(k) - H * x(k-1))$$

where $x(k-1)$ represents the measurement value at the previous moment and can be initially set to 0.

4. Update of the covariance matrix at time :

$$P(k) = (I - K * H) * P(k)$$

where I is the two-dimensional identity matrix.

5. Prediction of the state at time $k+1$:

$$x(k+1) = A * x(k) + B * a$$

where a is the acceleration at time , calculated from the velocity at time and the time interval.

6. Predictive update of the covariance matrix:

$$P(k+1) = AP(k)A^T + Q$$

7. Recording of current time data: This step prepares the data required for calculating a .

Implementation of gait prediction algorithm

In this study, a control strategy for the exoskeleton robot is designed based on normal gait parameters. The control scheme uses human walking parametersas a guide, enabling the exoskeleton to quickly transition to the corresponding motion state when switching between startup and gait phases [25]. The booster function is achieved by controlling the robot's speed to exceed human motion through real-time feedback adjustment.

The development environment for the control system program is KEIL MDK, where C language is used. **Figure 5** illustrates the flowchart of the main control program. During the debugging phase, after the robot system is powered on, the master control system's clock, interrupt, serial port, and mode selection controller are initialized. The parameters of each motor and driver are then verified by connecting to a computer to ensure they function correctly.

Since the relative operating angle of the robot must be tested in real time, the initial starting state is defined as a two-legged standing position. If the robot deviates from this state after the motors are operational, it can be restored by selecting the abnormal reset mode, ensuring the initial gait data is ready for execution. The communication protocol between the mode selection controller and the master control system is AA000xBB, transmitted wirelessly via the Bluetooth module. The variable x ranges from 1 to 4, representing the following instructions: 1: Normal operation; 2: Abnormal reset of the right hip joint; 3: Abnormal reset of the left hip joint; 4: Normal reset.

In the normal reset mode, the operation stops after returning to the initial two-legged standing position.

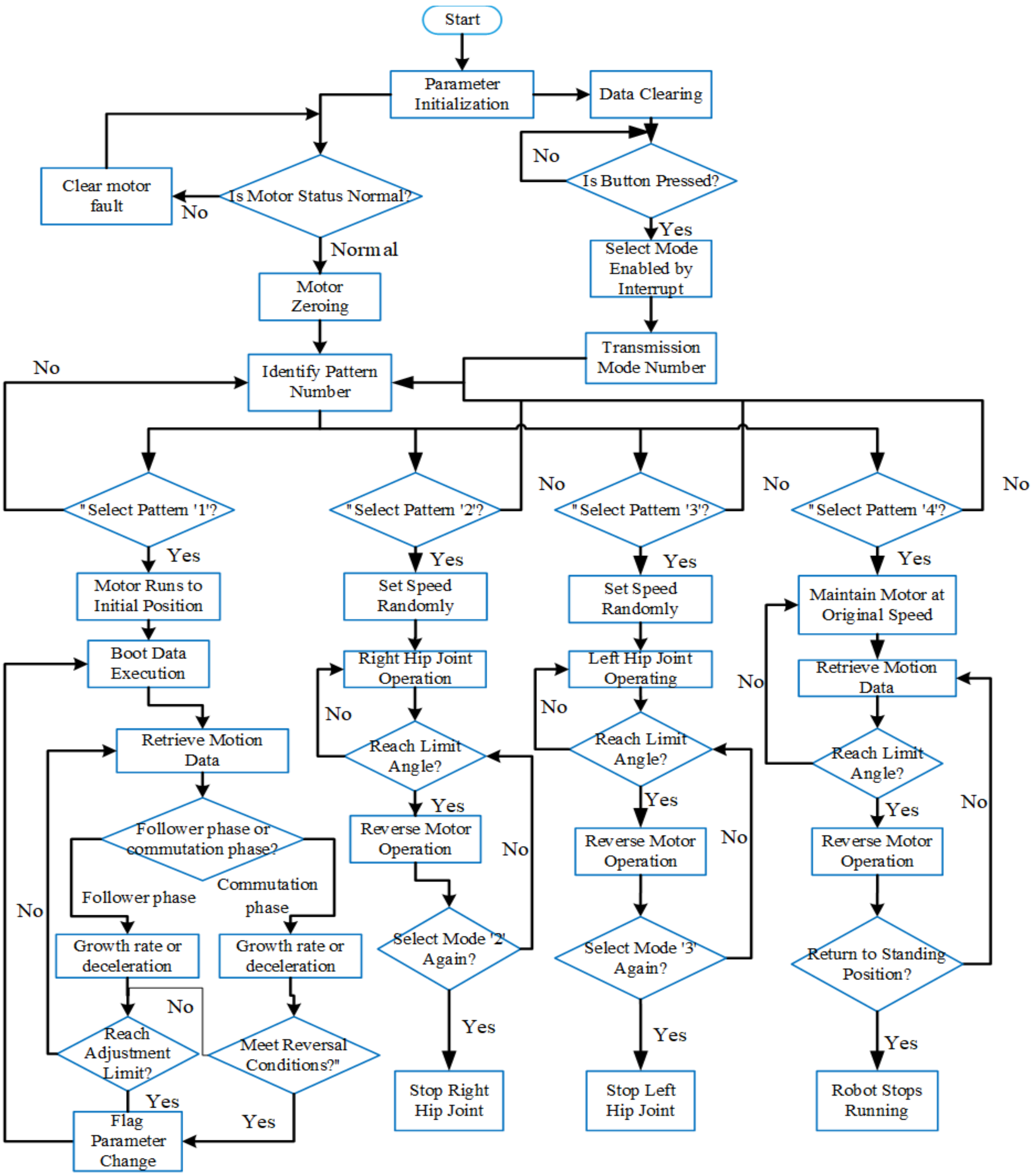

Figure 5. Main control program flow chart.

This study employs Profile Velocity Mode for robot control, focusing on the operational speed. The process is as follows [26]:

Retrieve the control index of the selected mode.

Activate the Profile Velocity Mode control mode via Service Data Object communication.

Clear any errors, enable the drivers and motors, and wait for the controller to select the working mode and transmit the corresponding control data.

In normal operation mode, the main control module transmits the initial guidance gait data to start the robot, entering the following phase. During this phase, the robot assists the human body in walking, with the torque sensor enabling users to adjust the operational speed of the robot.

When transitioning to the commutation phase, the system integrates direction switching functionality. The program evaluates the torque information from human-machine interaction and the current operating speed. Once the predefined conditions are satisfied, the system

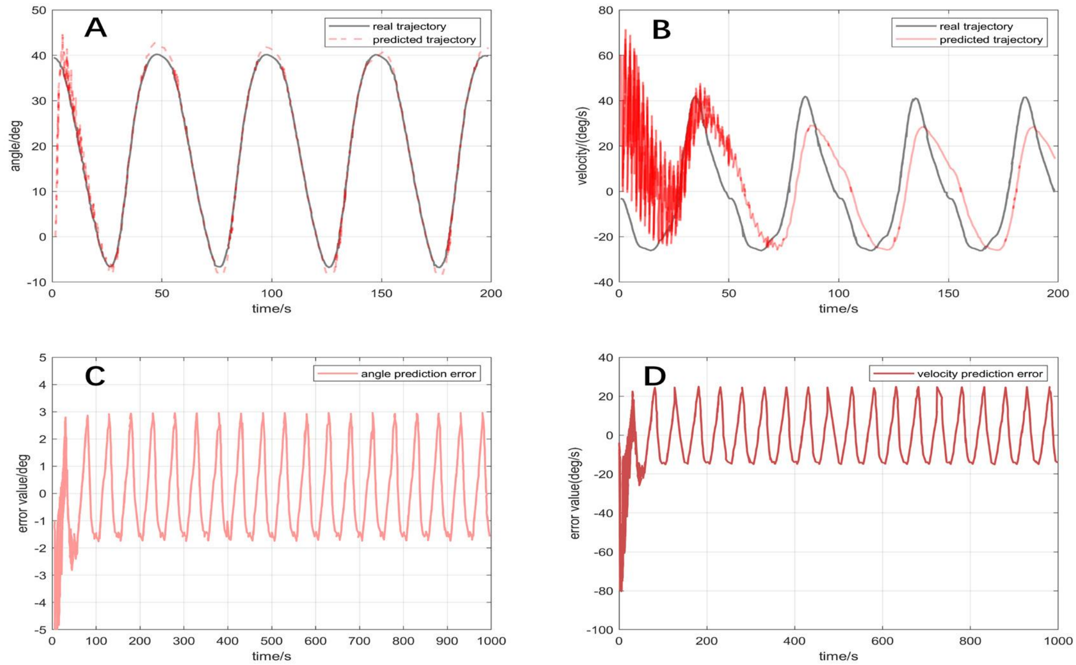

Figure 6. Simulation results of conventional Kalman filter prediction. (A) Angle change curve; (B) Velocity change curve; (C) Angle prediction error curve; (D) Speed prediction error curve.

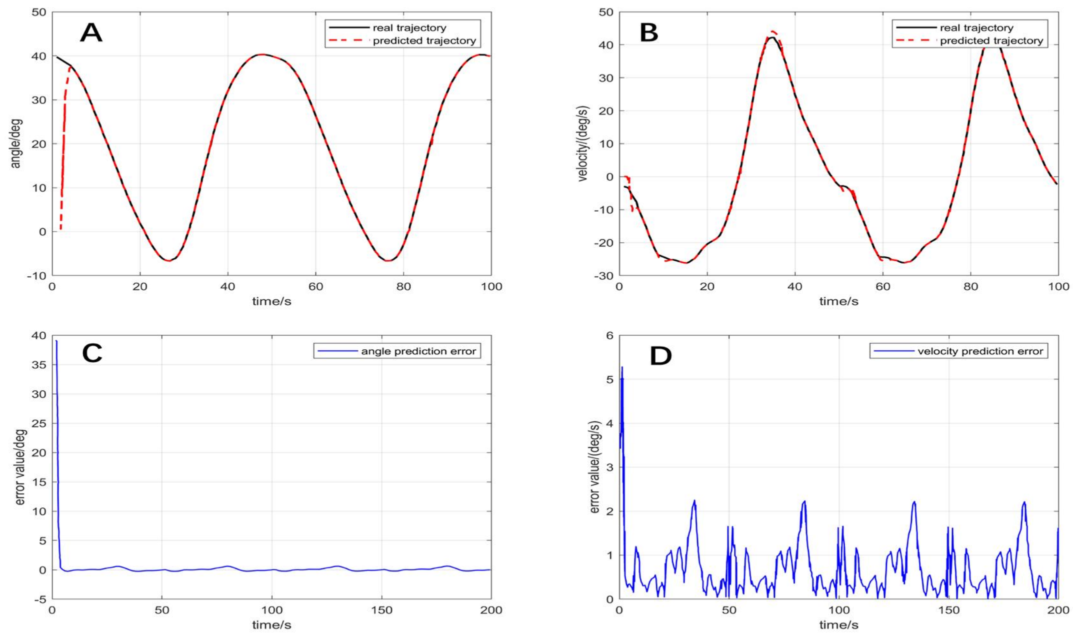

Figure 7. Simulation results of real-time updated Kalman filter prediction. (A) Angle change curve; (B) Velocity change curve; (C) Angle prediction error curve; (D) Speed prediction error curve.

transitions to the next stage of speed guidance control. To further ensure safety, the program includes limits on both the running speed and operating angle.

Result analysis

The model prediction simulations were conducted using MATLAB, with the results presented in **Figure 6** and **Figure 7**. **Figure 6** displays the prediction results of the conventional Kalman filtering model, while **Figure 7** shows the simulation results of the real-time updated Kalman filter model.

The results indicate that the real-time updated Kalman filter achieves gait predictions for lower limb exoskeleton robots that align more closely with actual motion parameters, demonstrating superior accuracy and stability. Compared with the conventional Kalman filter, the updated model achieves higher prediction accuracy, with reduced errors in both angle and velocity predictions and smaller fluctuations in the error curves.

In particular, the joint velocity change curves reveal significant jitter in the initial stage when using the conventional Kalman filter, requiring a stabilization period before aligning with the walking gait. In contrast, the real-time updated Kalman filter stabilizes much faster, effectively avoiding the jitter observed in the conventional model and adapting more rapidly to gait changes.

When stabilized, the real-time updated Kalman filter achieves a prediction error of no more than 1°, outperforming the conventional model's error range of 0°–5°, which only considers angle predictions with H=[1 0]T. This smaller error range further confirms the feasibility and effectiveness of the real-time updated model in gait prediction.

Conclusions and outlook

This study investigated a gait prediction method for lower limb exoskeleton robots using a real-time updatable Kalman filtering algorithm, aiming to enhance human-machine coordination and predict user motion intentions. A control strategy based on normal gait orientation was implemented using a microcontroller and Raspberry Pi as the core, combined with multi-sensor data fusion. The system achieved functional mode selection via Bluetooth communication. Experimental results showed that the real-time updated Kalman filter outperformed the conventional model in prediction accuracy, achieving a prediction error of no more than 1°.

Future research can focus on the following directions:

Algorithm Optimization: Enhancing computational efficiency to improve real-time performance, making the prediction algorithm more suitable for practical applications.

Integration of Additional Sensor Data: Incorporating biofeedback signals, such as electromyography, to enhance prediction accuracy and adaptability.

Broader Applications: Expanding the use of the system to military, industrial, and first-aid scenarios to meet diverse needs.

AI Integration: Leveraging advancements in artificial intelligence and machine learning to further improve gait prediction performance, enabling more intelligent and personalized support for users.

These developments will provide a robust technical foundation for the commercialization and clinical application of lower limb exoskeleton robots, advancing their utility and accessibility across various domains.

Author Contributions: Haonan Geng was responsible for writing and editing the whole paper, proposing the research idea and theoretical framework, designing the corresponding research program and implementing it. Xudong Guo was responsible for reviewing the draft paper and supervising the research work. Fengqi Zhong is responsible for the operation of the project and data analysis. Haibo Lin collected the necessary materials for the study and did some experiments. Guojie Zhang supervised the research and provided technical support. Qin Zhang provided the necessary resources and supervised the research work. Jiaheng Chen performed part of the data analysis and collected the required materials.

References

[1] Liu RP, Ou YJ. Development and Application of Lower Limb Exoskeleton Rehabilitation Robot. J Sun Yat-sen Univ (Med Sci) 2023;44(02):354-60.
[2] Acosta-Sojo Y, Stirling L. Individuals differ in muscle activation patterns during early adaptation to a powered ankle exoskeleton. Appl Ergon 2022;98:103593.
[3] Zhang JL, Li L, Liu XX. Development and Application Research of Wearable Exoskeleton Robot. Mach Electron 2018;36(03):77-80.
[4] Qu ZC. Research on intention recognition and motion control of lower limb assisted exoskeleton robot. Soochow University 2020.
[5] Song GM. Research and application of gait perception prediction and control method of lower limb exoskeleton. Hangzhou Dianzi University 2020.
[6] Kawamoto H, Hayashi T, Sakurai T, et al. Development of single leg version of HAL for hemiplegia. Annu Int Conf IEEE Eng Med Biol Soc 2009;2009:5038-5043.
[7] Hassan M, Kadone H, Suzuki K, et al. Wearable Gait Measurement System with an Instrumented Cane for Exoskeleton Control. Sensors 2014;14(1):1705-1722.
[8] Kadone H, Kubota S, Abe T, et al. Muscular Activity Modulation During Post-operative Walking With Hybrid Assistive Limb (HAL) in a Patient With Thoracic Myelopathy Due to Ossification of Posterior Longitudinal

Ligament: A Case Report. Front Neurol 2020;11:102.
[9] Wang YC, Wen CB, Wu XB. Fault detection and isolation of floating wind turbine pitch system based on Kalman filter and multi-attention 1DCNN. Syst Sci Control Eng 2024;12(1).
[10] Fan LP, Ma JJ. Design on broadcast depth detection device based on Kalman filter fusion algorithm. Ind Instrum Autom 2024;(04):7-12.
[11] Li FZ. Fusion optimization method of boiler oxygen measurement value based on Kalman filter. Resour Economization Environ Prot 2024;(08):53-56.
[12] Li BK, Tao ZY, Bian YH, et al. Design and analysis of a wearable lower extremity exoskeleton rehabilitation robot. J Lanzhou Inst Technol 2024;31(05):65-69.
[13] Bai X, Liang WY, Wang Q, et al. Progress and Trends in Lower Extremity Exoskeleton Robotics Researc. China Sci Technol Inf 2023;(17):146-9.
[14] Guo YF, Deng K, Huang LM, et al. Current Research Status of Active-Assist Lower Limb Rehabilitation Exoskeleton Robots. J Mech Transm 2024;1-16.
[15] Shi SC. Research on Control Techniques of Lower Extremity Boosting Exoskeleton. University of Electronic Science and Technology of China 2020.
[16] Huang P, Zhong HM, Chen B, et al. Three-dimensional gait analysis in normal young adults: temporalkinematic, kinematic and mechanical parameters. Chin J Tissue Eng Res 2015;19(24):3882-3888.
[17] Xiang J, Xu FY. Advances in Gait Analysis for Clinical Rehabilitation Applications. J Mod Med Health 2014;30(22):3411-3413.
[18] Tamer B. A New Approach to Linear Filtering and Prediction Problems. In: editors. Control Theory: Twenty-Five Seminal Papers (1932-1981). IEEE; 2001. p. 167-179.
[19] Zhang Y, Cao G, Li L, et al. AEKF-based trajectory-error compensation of knee exoskeleton for human–exoskeleton interaction control. Rob Intell Autom 2024;44:84-95.
[20] Li YH, Jin C, Shi HJ, et al. UAV positioning control based on Kalman filter algorithm. Nei Jiang Sci Technol 2024;45(10):40-42+109.
[21] Lu JQ, Li SY, Song LJ. The Research on Continuous Image Registration Filtering Based on Kalman Filter. Jiangxi Sci 2024;42(05):1079-1083.
[22] Zhou Y, Hu JN, Zhao Y, et al. Vehicle Target Tracking Based on Kalman Filtering Improved Compressed Sensing Algorithm. J Hunan Univ (Nat Sci) 2023;50(01):11-21.
[23] Weng X. Research on Model Predictive Control Algorithm Based on Dual Ideology. Xi'an Technological University 2022.
[24] Liu Y. Trajectory Prediction Based on Deep Learning. University of Electronic Science and Technology of China 2019.
[25] Perry J, Burnfield JM. Gait Analysis: Normal and Pathological Function. Translated by Shuyun Jiang. Shang Hai (China). Shanghai Scientific & Technical Publishers, 2017.
[26] ELLIS G. Control system design guide: using your computer to understand and diagnose feedback controllers. Amsterdam, Netherlands. Elsevier 2012.

Progress in Medical Devices
ISSN: 2957-5478

Zentime

Review Article https://doi.org/10.61189/314845qnicsc

Research progress on intestinal anastomosis technology and related devices

Yilong Chen, Lin Mao, Zijie Zhou, Chengli Song

Shanghai Institute for Minimally Invasive Therapy, School of Health Science and Engineering, University of Shanghai for Science and Technology, Shanghai 200093, China.

Corresponding author: Lin Mao.

Declaration of conflict of interest: None.

Received January 19, 2025; Accepted February 19, 2025; Published March 31, 2025

Highlights

- Continuous suturing in traditional manual suturing shortens operation time and reduces infection risk. Absorbable sutures are preferred for intestinal suturing and anastomosis to minimize foreign body reactions.
- Mechanical anastomosis with linear and circular metal staples offers distinct advantages, while new biodegradable staples demonstrate good performance.
- Magnetopressure anastomosis, leveraging magnetic attraction, has shown success in specific scenarios, providing innovative approaches to intestinal anastomosis.
- Radio frequency energy tissue welding technology enables rapid, seamless intestinal anastomosis, with fewer complications and holds strong potential for future applications.
- The support method for intestinal anastomosis, particularly the “degradable internal stent anastomosis” using a simple support method, shows significant promise in animal studies.

Abstract

This review comprehensively examines current intestinal anastomosis techniques. Traditional manual suturing methods, including intermittent and continuous sutures, provide high flexibility but but vary in infection risk and operation time. Continuous suturing is particularly effective in reducing operative time and infection risk. Suture materials include non-absorbable sutures, absorbable sutures, and natural materials, with absorbable sutures the most preferred for intestinal anastomosis. Mechanical anastomosis has gained widespread adoption, featuring both linear and circular metal staplers. Linear staplers are simple to operate, while circular staplers better align with physiological structures. Materials used in staplers include non-degradable metals (e.g., titanium, titanium alloy) and biodegradable anastomosis (e.g., magnesium alloy). Metal nail anastomosis often results in fewer complications than manual suturing in specific surgeries. Magnetic pressure anastomosis, relying on magnet attraction, has been successfully applied in clinical scenarios following extensive research. The adhesive-based approach involves medical adhesives such as cyanoacrylate and fibrin glue, offering auxiliary support for anastomosis. Energy tissue welding encompasses laser and radio frequency energy tissue welding. While laser welding poses a risk of thermal damage, radio frequency welding offers significant advantages, including faster, seamless anastomosis with reduced complications. The support method for intestinal anastomosis is a novel concept, involving the addition of support materials to the original anastomosis. It can be divided into composite and simple support methods. The simple support method, as evidenced by the “degradable internal scaffold method for digestive tract anastomosis” developed by Cai et al. in China, has demonstrated promising results in animal experiments. In conclusion, selecting the appropriate intestinal anastomosis technique depends on clinical scenarios to optimize surgical outcomes and reduce complications. The diverse technological advancements reviewed here present valuable opportunities for enhancing the quality and safety of intestinal surgery.

Keywords: Intestinal anastomosis technique, manual suture, mechanical anastomosis, magnetic pressure anastomosis, support anastomosis

I Introduction

Intestinal anastomosis is a fundamental surgical procedure that every general surgeon must master. It is among the most common procedures in abdominal surgery. Various methods of

Address correspondence to: Lin Mao, Shanghai Institute for Minimally Invasive Therapy, School of Health Science and Engineering, University of Shanghai for Science and Technology, Yangpu District, Shanghai 200093, China. Tel: +86-21-55572159. E-mail: linmao@usst.edu.cn.

intestinal anastomosis have evolved, including manual suture, metal nail device anastomosis, and "seamless closure technology". Despite advancements, these techniques cannot entirely eliminate complications such as anastomotic leakage and stenosis [1]. Moreover, with the advent of the "minimally invasive era" in modern surgery, higher standards for intestinal anastomosis have been established [2, 3].

Manual suturing remains a cornerstone technique in intestinal anastomosis, relying heavily on the surgeon's skill to accurately align and suture the intestinal tissues. The two primary suturing methods are interrupted and continuous suture. Interrupted suturing offers high flexibility, allowing adjustment to accommodate the wound's specific characteristics and facilitating effective wound observation during the healing process. However, this method is often time-consuming and more prone to infection. Conversely, continuous suturing reduces operative time, lowers infection risk, evenly distributes tissue tension, and minimizes the formation of dead spaces [4]. The selection of suture material is also critical to the success of manual suturing. Available materials include non-absorbable and absorbable sutures, as well as natural options. Each material offers distinct properties that influence the efficacy of the anastomosis and the patient's recovery trajectory [5].

However, traditional manual stitching is not without limitations. The procedure is relatively complex, necessitating a high level of technical proficiency and experience. Furthermore, it is time-consuming and associated with an increased risk of intraoperative bleeding, which increases the complexity and risk of the operation. To address these challenges, mechanical anastomosis methods, particularly metal staplers, have been developed, marking a significant advancement in intestinal anastomosis [6]. Mechanical anastomosis instruments include linear and circular staplers. Linear staplers are known for their simplicity and efficiency, while circular staplers are designed to align with the intestine's physiological structure, reducing the risk of anastomotic stenosis. The use of staplers has demonstrated clear benefits over traditional suturing techniques, including shorter operation times, fewer postoperative complications, and reduced patient discomfort [7]. Furthermore, the development of biodegradable staples offers new possibilities for improving intestinal anastomosis [8].

Despite the acknowledged benefits, mechanical anastomosis also has drawbacks. For instance, permanent titanium staples may induce inflammatory responses and lead to severe complications [9]. Consequently, exploring innovative anastomosis techniques has emerged as a focus in intestinal surgery research. Magnetopressure anastomosis utilizes magnetic attraction to create an intestinal anastomosis, thus eliminating the need for permanent foreign bodies and introducing a novel approach to this procedure. The intestinal adhesion method, involving medical adhesives such as cyanoacrylate and fibrin glue, serves as a supplementary technique to enhance anastomosis strength and reduces the risk of anastomotic leakage [10, 11]. Energy tissue welding technology, including laser welding and radio frequency (RF) energy tissue welding, employs energy sources such as light and electricity to achieve seamless anastomosis. Additionally, the concept of support-based anastomosis methods, which includes both composite and simple support techniques, offers an innovative strategy for intestinal anastomosis with promising potential.

Despite significant advancements in intestinal anastomosis technology, several challenges remain. Key research areas include improving anastomosis quality and safety to reduce postoperative complications and optimizing the selection of anastomosis methods and materials based on individual patient needs. This article aims to provide a comprehensive review of the current status and research progress of intestinal anastomosis technology. It evaluates the advantages and disadvantages of various techniques and offers insights into both research and clinical practice. The ultimate goal is to drive the continuous development and refinement of intestinal anastomosis methods, contributing to improved patient outcomes.

II Review progress

Traditional manual stitching

Traditional intestinal suture methods

Intestinal anastomosis is a critical step in surgical procedures, with the successful healing of the anastomosis significantly influencing surgical outcomes. Contemporary suturing techniques primarily include interrupted and continuous suture methods.

Interrupted sutures vs. continuous sutures

The history of manual suturing dates back to ancient China, where the renowned physician Hua Tuo is believed to have invented Ma Boiling Powder to aid in patient recovery. Since the

19^{th} century, research on manual sutures for intestinal anastomosis has progressed rapidly [12]. Interrupted suturing is considered a classic method due to its high flexibility. Each stitch is independent, allowing for adjustments based on the wound's specific conditions. Furthermore, it can be applied to wounds of various sizes and shapes and facilitates better observation of the healing process, enabling early detection and treatment of complications. However, a notable drawback is its susceptibility to infection, as dirt and debris can accumulate between knots, necessitating regular cleaning. Additionally, intermittent suturing is more time-consuming than continuous suturing since each knot must be tied individually.

To enhance efficacy and reduce operative time, the continuous suture method was developed. This method not only shortens the operation time but also maintains an intestinal patency rate comparable to that of interrupted sutures. Sert et al. conducted a comparative study, demonstrating that continuous suturing could reduce operation time by 50% [4]. The benefits of this method mainly include even distribution of tissue tension and tighter incision closure.

Suture material

A wide variety of sutures is used in manual suturing, all of which must meet specific criteria. First, sutures must be universal, sterile, non-electrolytic, non-allergenic, and non-carcinogenic to prevent bacterial growth. Second, sutures should be easy to handle, provide secure knotting without wear or cutting, and maintain adequate tension and strength. Third, for intestinal suturing, the material should be absorbed by the body, triggering only a mild biological response or no response [13].

Non-absorbable sutures

Non-absorbable sutures provide long-term support for tissues requiring sustained reinforcement, such as in cardiac or macrovascular surgeries. However, their use in intestinal anastomosis is limited due to the risk of chronic inflammation and foreign body granulomas formation. Nylon, a synthetic polyamide known for its high strength and durability is associated with a significant tissue reaction. Polyester, a synthetic polyethylene terephthalate, offers strength and longevity but also provokes a large tissue reaction.

While non-absorbable sutures offer advantages in scenarios requiring long-term support, their propensity to trigger substantial tissue reaction makes them less suitable for intestinal suturing. This limitation is primarily due to their foreign body response, a characteristic that restricts their broader application in this context.

Absorbable sutures

Absorbable sutures are designed to be absorbed by the body gradually, reducing the risk of long-term foreign body reactions. They are particularly recommended for intestinal anastomosis. VicrylPlus™, developed by Zhao et al. in 2008, contains triclosan, an antimicrobial agent, effectively inhibiting bacterial growth around the sutures [14]. Biosutures, synthesized by Pascual et al. in 2008, is a novel suture that uses adipose-derived mesenchymal stem cells for cladding, promoting intestinal healing through stem cell differentiation [15]. V-LocTM, featuring a barbed design that introduced in 2009 by Demyttenaere et al., eliminates the need for knotting, thereby reducing the risk of anastomosis disruption by knotting. This design facilitates the suturing operation under laparoscopic or robotic assisted suturing, enhancing the ease and efficiency of the procedure [5, 16].

Natural materials

While synthetic materials dominate modern surgical sutures, natural materials continue to hold clinical value in specific contexts. Silk, composed of silk fibroin, a protein with high tensile strength offers durability but are associated with a significant tissue reaction. Additionally, its rapid water absorption nature can lead to swelling, limiting its use in contemporary intestinal anastomosis. Catgut (Gut), made from animal tendon collagen, is absorbable; however, its short absorption time and propensity to elicit tissue reactions have reduced their frequency of use in modern practice. Recent innovations have introduced multifunctional sutures. For instance, antimicrobial-coated sutures, coated with substances like triclosan, can significantly reduce the risk of wound infection, making them suitable for surgeries with a high risk of contamination. Smart sutures, which integrates nanotechnology and shape memory materials, enable real-time monitoring of wound conditions and can release medications on demand, promoting targeted and accelerated healing.

Intestinal mechanical anastomosis

Metal nail stapler

Metal nail staplers are designed to apply pressure to deploy staples that reconnect tissues through staple deformation, achieving tissue anastomosis. Different structural types, including linear and circular staplers, are developed to match the physiological characteristics of specific anatomical sites.

Linear staplers

The conventional manual suturing techniques are often time-consuming, with a higher risk of intraoperative bleeding. In recent years, gastrointestinal staplers, particularly linear staplers, have become increasingly popular for lateral anastomosis or when tissue resection and anastomosis are required. Common applications include: gastrointestinal bypass procedures (e.g., gastrojejunal anastomosis) to create a wide anastomosis; partial intestine resection with posterior anastomosis to prevent intestinal lumen narrowing; and rectal stump closure during low anterior rectal resection. The mechanism of action of linear staplers involves inserting two rows of interlaced staples into the intestinal wall, facilitating efficient and neat anastomosis. They are simple to operate, enabling quick anastomosis and producing a clean anastomotic line. The selection of stapler depends on the intestinal diameter and specific surgical requirements. For instance, in colon surgery, a linear stapler with a longer staple chamber and wider stich spacing may be more suitable to accommodate the larger diameter of the colon.

Circular staplers

Circular staplers are frequently used for the end-to-end anastomosis of the intestine, offering distinct advantages in specific surgical scenarios, including esophagogastric anastomosis, colorectal anastomosis (especially in cases of narrow pelvic space), and ileal pouch-anal anastomosis to maintain mucosal alignment integrity. The mechanism of action involves a nail seat and a nail bin, where the broken ends of the intestine are secured. Upon firing, a circular stapler anastomosis is achieved in a single step. The primary benefit of circular staplers is their ability to create a round anastomotic connection that closely matches physiological structures, thereby reducing the risk of anastomotic stenosis.

However, it is important to note that circular staplers are not without limitations. For instance, there is a potential for for incomplete anastomosis or leakage if not properly aligned. Besides, the cost of circular staplers is relatively high, which increases the overall cost of surgery.

Anstomosis Material

Traditional non-degradable anastomoses

Titanium and titanium alloys are widely used in traditional non-degradable anastomoses, offering several advantages for gastrointestinal anastomosis. Titanium, with a density of approximately 4.5 g/cm^3 at room temperature, provides the ideal balance of strength and lightness, allowing anastomosis nails to remain in the body long-term without adding undue stress. The non-magnetic nature of titanium alloys renders them well-suited for gastrointestinal anastomoses, especially in scenarios involving magnetic resonance imaging environments. The low elastic modulus of titanium alloys enables the material to deform under external forces, which is critical for forming anastomotic pinching and reducing the risk of postoperative leakage. Titanium alloys exhibit excellent resistance to erosin by biological fluids, including intestinal fluid, which ensures long-term durability. Furthermore, high mechanical strength and toughness can maintain the structural stability and functionality of anastomosis nails in complex human environments. Titanium alloys such as Ti-3Al-2.5V and Ti-6Al-4V exibit enhanced mechanical properties while retaining the excellent biocompatibility and corrosion resistance of pure titanium by adding aluminium and vanadium. In the domain of general surgery gastrointestinal reconstruction, titanium alloys are extensively utilised in the fabrication of anastomosis nails, aiding in reliable tissue fixation and effective reduction of postoperative complications. However, the permanent presence of titanium in the human body is associated with certain drawbacks, such as imaging artifacts in CT, which could potentially lead to misdiagnosis, and postoperative complications like congestion, inflammation, and the risk of developing hepatic granulomas [9, 17, 18].

Biodegradable anastomoses

Magnesium alloys have a long history of biomedical exploration, with the earliest documented use dating back to 1907. Zheng et al. implanted tubular magnesium connectors in the stomach and intestines of dogs, demonstrating the preliminary feasibility of magnesium-based implants in the gastrointestinal tract [19]. Nevertheless, the support duration and degradation rate of these implants were highly dependent on their anatomical position and size. Consequently, the utilisation of magnesium alloy in clinical settings necessitates careful consideration of the clinical titanium

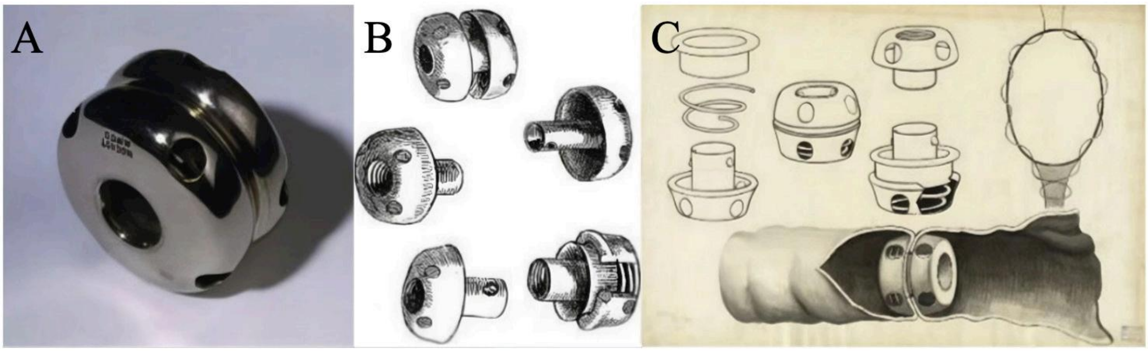

Figure 1. Murphy Button and its operational functionality. (A) Murphy Button in general; (B) Exploded view of the Murphy Button; (C) Schematic diagram of the Murphy Button at work. This figure is adapted from [31].

staple diameter of 0.3 mm, balancing the challenge between effective tissue engagement and optimal device degradation time. Modern advancements in magnesium alloys processing have revitalized interest in their clinical applications, particularly in gastrointestinal anastomosis. Research has focused on enhancing the mechanical strength and biodegradability of high-purity (HP) Mg and its alloys. In 2016, Wu et al. developed a novel HP Mg anastomostomosis device [7]. Qu et al. evaluated the biocompatibility and degradation behaviour of HP Mg staples in small intestinal anastomosis, showing reduced inflammatory responses [20]. Xu et al. reported that adjusting local Mg^{2+} ion concentrations could potentially support anti-tumor therapy [21]. These reports highlight an innovative application of biodegradable magnesium-based materials with numerous benefits.

Recent studies suggest that there is no difference in the complication rate between metal nail anastomosis and manual suturing in gastrointestinal anastomosis, small intestine anastomosis, and colonic anastomosis [6, 22-25]. However, the complication rate of esophagogastric anastomosis and ileocolic anastomosis is lower with metal nail anastomosis than that with manual suturing, which may be related to the improvement of stapler manufacturing processes [26, 27].

Pressurized anastomosis

Regardless of whether manual suturing or mechanical stapling is used, both methods introduce foreign materials to close the intestinal tube, leading to the presence of a foreign body at the anastomosis [28]. In contrast, compression anastomosis; the third generation of anastomosis techniques, offers a method that potentially reduces foreign body residues. This technique is particularly advantageous in intestinal stricture or complex anatomical structures, where avoiding foreign body presence is crucial. Common applications include low recto-anal anastomosis, duodenal, and jejunal anastomosis.

The origins of compression anastomosis date back to the early 20th century, with early experiments involving compression rings for intestinal anastomosis. In 1826, Lambert et al. pioneered the use of compression anastomosis rings, demonstrating the feasibility of this approach [29]. Denan subsequently achieved a seamless intestinal anastomosis using a compression ring in late 19th century. In 1892, Murphy invented the “Murphy Button,” a metal anastomosis ring that applied pressure to the anastomotic wall, causing tissue atrophy and necrosis, and allowing the compression ring to eventually detach and enter the intestinal lumen [30]. While effective, the high cost and complexity of the procedure limited its widespread adoption (**Figure 1**) [31]. In the 1980s, research shifted towards magnetic compression anastomosis rings for intestinal anastomosis [32]. The feasibility and effectiveness of this technique were demonstrated in studies [33]. In 1984, the “AKA-2” compression anastomosis ring was developed by Kanshin et al. and gained clinical acceptance [34]. Material science advancements in the 1990s led to the creation of the Valtrac BAR, a biodegradable compression anastomosis ring (**Figure 2A**) [31]. Its anastomosis principle is similar to that of the “Murphy button”, but with notable improvements: reduced tissue ischemia and necrosis as well as low incidence of anastomotic stenosis. However, the Valtrac BAR technique is technically demanding. Surgeons must accurately select the size of the anastomosis ring based on intestinal tube diameter and intestinal wall thickness. The gap between the rings must be adjusted manually, relying heavily on the surgeon’s experience.

The development of memory alloy pressurized

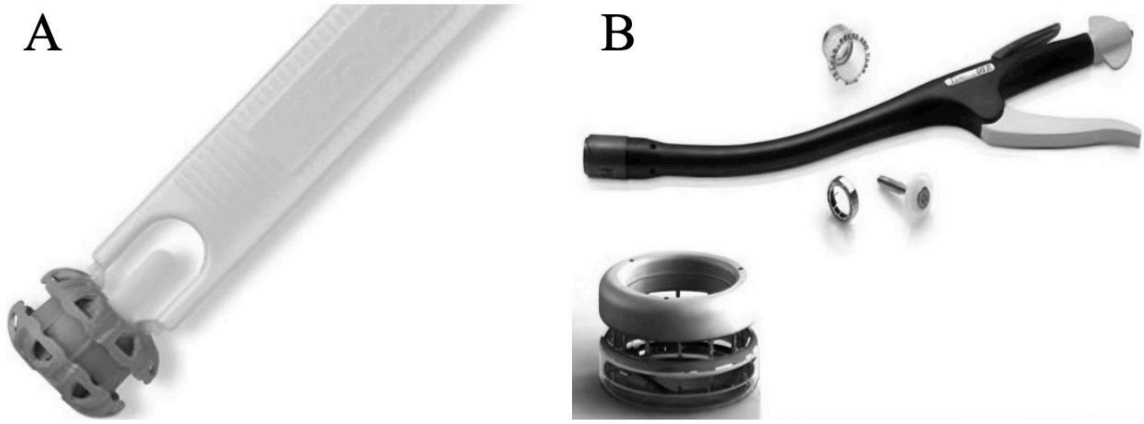

Figure 2. Several typical pressurized anastomosis devices. (A) Valtrac BAR; (B) Ni-Ti memory alloy pressurized anastomosis ring. This figure is adapted from [31].

anastomosis rings represents a significant advancement in compression anastomosis technology. The Nitinol memory alloy pressurized anastomosis ring (**Figure 2B**) was authorised by the China Food and Drug Administration for clinical application [31]. Fudan University Cancer Hospital successfully completed the first clinical anastomosis in Asia using this technology. The Nitinol ring remained in the body for 12-18 days, effectively reducing the risk of anastomotic inflammation [35].

Despite its advantages, the pressurized stapler technique presents several technical challenges, particularly related to the precise alignment of magnets. The dynamic peristalsis of the intestines poses a significant obstacle to the accurate placement of magnets within the internal environment. One potential solution is to employ advanced imaging techniques, such as intraoperative real-time ultrasound imaging, to enhance the visualization of magnet positioning, promoting more accurate alignment during anastomosis procedures. Additionally, the variability in intestinal anatomy, such as curvature and thickness, affect the effective alignment of the magnetic field. To address this, developing magnet systems capable of adjusting magnetic strength and field direction could accommodate anatomical variations among patients, thereby improving the success rate of pressurized stapler anastomosis.

Intestinal adhesion method

Medical adhesives used in intestinal anastomosis can be broadly categorized into two main types: chemical glue (primarily α-cyanoacrylate adhesives; e.g., OB and EC glues) and biological glue (e.g., fibrin sealants).

Cyanoacrylate adhesives

The binding mechanism of cyanoacrylate adhesives involves interaction with proteins present in all cellular structures. Organic amines act as catalysts in the polymerisation of cyanoacrylate monomers, allowing for rapid curing at room temperature. The natural moisture in the body further accelerates the curing process. Conversely, due to its nature as an ester compound, cyanoacrylate demonstrates reduced bonding strength in wet conditions, limiting its use in organs with secretory functions, such as the digestive tract. Currently, α-cyanoacrylate is used solely as an adjunct to manual suturing or instrumental anastomosis, serving primarily to reinforce anastomosis and reduce the risk of anastomotic leakage [10, 36].

Fibrin gule

Fibrin glue is primarily composed of fibrinogen and thrombin, which work together to form a fibrin network upon application to intestinal tissues. When thrombin activates fibrinogen, this network traps surrounding cells and tissues, forming a stable adhesive structure that bonds effectively with the intestinal tissue. The fibrin glue offers several advantages, such as reducing operation time and complexity and minimising tissue damage. However, it is important to note that fibrin glue does have certain drawbacks. Firstly, the adhesive strength of fibrin glue is low compared to traditional suture methods, making it unsuitable for high-tension applications. Secondly, it is more expensive and requires special storage and handling conditions. Currently, fibrin glue is primarily used as an adjuvant in intestinal anastomosis. Subsequent to manual suturing or instrumental anastomosis, it reinforces the anastomosis and helps reduce the risk of anastomotic leakage. In recent years, there have also been reports of "seamless" intestinal anastomosis using fibrin glue-coated collagen patches or fleece [11, 37].

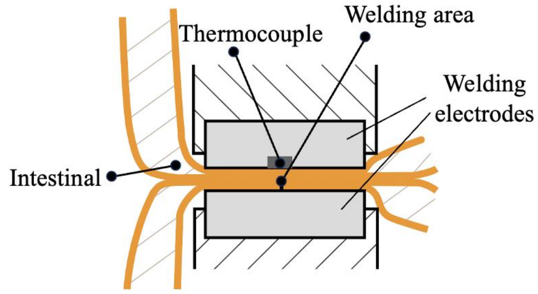

Figure 3. Radiofrequency energy tissue welding.

Energy tissue welding

Energy tissue welding anastomosis involves applying heat energy to tissues using light, electricity, and other energy forms. This process alters the molecular structure of tissue proteins, enabling tissue connection. Two primary methods in this domain are laser welding and RF energy tissue welding.

Laser welding

Laser energy was among the first energy-based methods explored for tissue welding. Compared to conventional manual sutures and mechanical anastomosis, laser welding produces a smoother intestinal wall surface and eliminates foreign body residues, reducing the likelihood of postoperative complications [38]. In the 1960s, Yahr proposed the concept of laser tissue welding [39]. Subsequent research by Cochrane demonstrated that laser anastomosis in rat colons achieved anastomotic strength comparable to manual sutures within 7 days post-surgery [40]. Yamada conducted intestinal closure tests on sick cats and dogs using various laser types, and optimal results were observed at laser power settings of 6-10 W [41]. To boost anastomotic strength, researchers developed techniques to apply biological coatings to the anastomosis site during laser welding. These coatings, such as proteins, help regulate laser energy release by providing feedback signals [42]. Huang et al. used elastin as a binding agent to laser weld the ruptured porcine small intestine, and the experimental results showed that the use of elastin significantly improved the tensile strength and burst pressure of the welded intestinal tissue [43].

Ultrasound energy

Ultrasound energy involves sound waves with frequencies above 20 kHz, which transmit energy through mechanical vibrations. When ultrasound is applied to biological tissues, it produces mechanical, thermal, and physicochemical effects, contributing to tissue cutting and anastomosis. The mechanisms of action include the following asepects. Oscillatory movement: ultrasound induces vibrations that lead to the vaporization of water molecules in tissues; the protein structure is disrupted, acilitating tissue cutting and mechanical separation. Thermal effect: Tissues absorb ultrasonic energy, leading to a temperature increase, which causes denaturation and recoagulation of extracellular matrix proteins, promoting tissue bonding. Physicochemical effect: this enhances protein synthesis, blood vessel formation, and injury repair and healing; the physicochemical changes contribute to stable tissue adhesion, aiding the anastomosis process.

However, the uneven transmission of ultrasonic energy during tissue welding presents a significant challenge in achieving precise control over the welding depth and width, affecting the stability of the anastomosis site. Current ultrasound-anastomosed tissues do not meet the biomechanical demands of normal physiological functions, limiting clinical applicability. In future research, the research direction should focus on developing technologies to ensure uniform distribution of ultrasonic energy, enhancing control over welding precision. Concurrently, new materials that improve the effectiveness of tissue welding and enhance biomechanical strength are also a promising research focus.

RF energy tissue welding

RF energy tissue welding employs electric current to heat biological tissues, a mechanism similar to laser welding. When tissues are heated to a specific temperature range, protein denaturation occurs. By maintaining a uniform and stable temperature, protein reaggregation is prevented, promoting the formation of stable protein linkages and enabling tissue incision anastomosis (**Figure 3**).

In RF tissue welding, the frequency of the RF current is typically 450-500 kHz [44, 45]. Radiofrequency tissue welding, employed in devices like LigaSure (Medtronic), was first used for vascular anastomosis [46, 47]. Building on the success of radiofrequency energy in the domain of vascular anastomosis, researchers have explored its application in intestinal anastomosis. Tu et al. investigated the impact of various control parameters (power, time interval, terminal impedance) on intestinal anastomosis using radiofrequency energy, and employed two indicators, burst pressure and thermal injury, to assess the quality of intestinal anastomosis [48]. The findings revealed that when the power was set at 100 W, the time interval was 2000 ms, and the terminal impedance was 50 Ω, the maximum burst pressure could reach approximately 8.46 kPa following intestinal anastomosis. Pan et al. conducted intestinal closure experiments on 18 pigs using radiofrequency energy (LigaSure, Valleylab), with traditional manual suturing and mechanical anastomosis serving as control groups [49]. Histological examination showed collagen fibers filling the muscular layer gaps in the RF-welded anastomosis, in comparison to the control groups, indicating superior tissue fusion. Wang et al. used custom RF platform with adjustable voltage, action time, and applied pressure, to assess the effect of RF energy-based anastomosis in the small intestine [44]. The anastomosis quality was evaluated based on burst pressure and microstructure observations. The results demonstrated that maintaining impedance between 61.0 and 86.2 Ω yielded satisfactory anastomosis quality. Lacitignola et al. used RF-based laparoscopic vascular occlusion devices to test small intestine closure in pigs, and demonstrated that the burst pressure of the RF-closed small intestine reached approximately 40 mmHg, demonstrating robust anastomotic strength [50].

RF energy tissue welding technology facilitates rapid and seamless anastomosis of tissues and organs, exhibiting notable advantages, including the absence of foreign body intervention, high initial tensile strength, expedited postoperative healing with minimal complications. This technique holds considerable clinical research value and surpasses alternative anastomosis techniques.

Intestinal anastomosis by the support method

Intestinal anastomosis by the support method is a novel concept involving the placement of a supportive material within the intestinal wall to reinforce anastomosis during traditional anastomotic procedures [29]. This approach is categorized into composite support anastomosis and simple support anastomosis.

Composite support method

The healing process of intestinal anastomosis involves restoring intestinal wall continuity, balancing intraluminal pressure and intestinal wall pressure. From a biomechanical perspective, maintaining this pressure balance is crucial to prevent anastomotic leakage. The principle underpinning this method is that as long as the intestinal wall force at the anastomosis site exceeds the intraluminal pressure, the risk of anastomotic leakage remains low. Traditional techniques such as manual suturing, stapling, bonding, and welding anastomosis all aim to restore this balance by reconstructing the intestinal wall's structural integrity. While not providing strong compressive force, compression anastomosis effectively resists intraluminal pressure, contributing to pressure equilibrium between the intestinal lumen and intestinal wall The composite support method enhances the original anastomosis technique by adding a layer of supportive material. While this reduces the intestinal pressure at the anastomosis to a certain extent, it concomitantly increases the intestinal wall pressure.

Simple support method

The simple support method of intestinal anastomosis represents a significant innovation in traditional anastomotic techniques. This method uses two binding lines (or alternative methodologies) to secure the intestinal wall and support material, thereby establishing a “zero pressure zone” within the intestinal healing region between the two binding lines. This pressure-neutral environment is conducive to optimal tissue healing. A similar bundle anastomosis was first documented in the late 19th century. In 1894, Abbe tied grooved glass tubes to the severed vessel ends and achieved “seamless” end-to-end anastomosis of the blood vessels [51]. In 1980, Payr refined the “Abbe method” using a magnesium ring equipped with a grooved end [52]. This innovation involved initially placing the magnesium ring on the adventitia of the blood vessel during anastomosis, followed by exteriorizing the severed vessel end to expose the intima. The procedure was completed by inserting the contralateral intima of the blood vessel into the exposed intima, thereby achieving a secure and seamless binding.

In China, Peng et al. advanced this concept through the development of the “degradable internal stent gastrointestinal anastomosis”, building upon their prior work with bundled line pancreatic anastomosis and bundled pancreatic-gastric anastomosis [53-55]. Prior animal experiment has demonstrated the safety and feasibility of this method, demonstrating its capacity to complete gastrointestinal, small intestine, and colonic anastomosis in a normal abdominal environment, but also to repair anastomotic leakage or colonic perforation in phase I of infectious environments [56, 57].

III Conclusion

The development of intestinal anastomosis technology is crucial for advancing intestinal surgery. This paper systematically reviewed and analyzed various intestinal anastomosis techniques, demonstrating that each method has unique advantages and limitations. Selecting the appropriate technique requires careful consideration of clinical factors to optimize surgical outcomes.

(1) Traditional manual suturing constitutes the fundamental method of intestinal anastomosis. Intermittent suture offers high flexibility but is time-consuming and prone to infection. Continuous sutures reduce the operation time and the risk of infection. The selection of suture material is of paramount importance, with absorbable sutures offering distinct advantages in the context of intestinal suturing, thereby mitigating the risk of foreign body reactions. The advent of novel multifunctional sutures expands the possibilities for intestinal anastomosis. However, the technical complexity of manual suturing demands high surgical expertise, potentially limiting its effectiveness in complex surgeries.

(2) Intestinal mechanical anastomosis is a widely applied technique, and the advent of metal nail staplers has significantly improved surgical efficiency. Linear stapler is simple to operate, and the circular stapler anastomosis aligns well with physiological structure. However, there are also limitations, such as incomplete anastomosis, anastomotic leakage, and high cost. The continuous improvement of staple materials, such as the emergence of biodegradable staplers, provides a new solution to the problem of long-term retention of traditional non-degradable stasmosis staples. Nevertheless, the mechanical properties of biodegradable staples still need to be further improved.

(3) Magnetic pressure anastomosis is a novel technique that utilizes magnetic attraction to facilitate intestinal anastomosis, effectively eliminating the risk for foreign body residues at the anastomosis. This technology demonstrates significant potential in specific clinical scenarios. Nevertheless, this technology may still have certain limitations in terms of operation accuracy and scope of application, necessitating further research and clinical trials to refine the technique and expand its applicability.

The adhesion method employs medical adhesives as intestinal anastomosis adjuvants, contributing to reinforced anastomosis and a reduced risk of anastomotic leakage. However, challenges such as inadequate adhesive strength and high cost persist. Energy tissue welding technology, particularly RF energy tissue welding, offers a promising alternative. RF energy welding provides strong initial tensile strength, and no foreign body intervention, making it a viable choice for intestinal anastomosis. However, laser welding is hindered by problems such as thermal damage, which limits its application.

The the support method in intestinal anastomosis is a novel concept, offering innovative approaches through the composite support method and simple support method. For instance, the "biodegradable internal stent gastrointestinal anastomosis" has demonstrated favourable outcomes in animal experiments; however, further clinical studies are required to substantiate its safety and efficacy.

In conclusion, the field of intestinal anastomosis techniques is undergoing continuous evolution, driven by innovative research and technological advancement. The emergence of safer, more effective, and user-friendly methods is expected. These advancements will likely contribute to improved quality of care, reduced complication rates, and better surgical outcome.

Author Contributions: Lin Mao, Chengli Song and Yilong Chen conceived this project. Yilong Chen and Zijie Zhou collected and organized the literature. Lin Mao helped to revise the logic of the article, polish the language and modify the formatting. All authors contributed to the writing of the manuscript.

References

[1] Nandakumar G, Stein SL, Michelassi F. Anastomoses of the lower gastrointestinal tract. Nat Rev Gastroenterol Hepatol 2009;6(12):709-716.
[2] Meshikhes AW. Controversy of hand-assisted laparoscopic colorectal surgery. World J Gastroenterol 2010;16(45):5662-5668.
[3] Tavakoli A, Bakhtiari J, Khalaj AR, et al. Single-layer versus double-layer laparoscopic intracorporeally sutured gastrointestinal anastomoses in the canine model. JSLS 2010;14(4):509-515.
[4] Sert G, Aksoyler D, Kara M, et al. Comparison of total anastomosis time between four different combinations of suturing and knot tying techniques in microsurgical anastomosis. J Plast Surg Hand Surg 2023;57(1-6):240-246.
[5] Demyttenaere SV, Nau P, Henn M, et al. Barbed suture for gastrointestinal closure: a randomized control trial. Surg Innov 2009;16(3):237-242.

[6] Zhang Y, Cao J, Lu M, et al. A biodegradable magnesium surgical staple for colonic anastomosis: In vitro and in vivo evaluation. Bioact Mater 2023;22:225-238.
[7] Wu H, Zhao C, Ni J, et al. Research of a novel biodegradable surgical staple made of high purity magnesium. Bioact Mater 2016;1(2):122-126.
[8] Guo H, Hu J, Shen Z, et al. In vitro and in vivo studies of biodegradable Zn-Li-Mn alloy staples designed for gastrointestinal anastomosis. Acta Biomater 2021;121:713-723.
[9] Zhang H, Gao M, Tian X, et al. Study on Mechanical Properties and Degradation Behavior of Magnesium Alloy Vascular Clip. J Funct Biomater 2023;14(10):501.
[10] Paral J, Subrt Z, Lochman P, et al. Suture-free anastomosis of the colon experimental comparison of two cyanoacrylate adhesives. J Gastrointest Surg 2011;15(3):451-459.
[11] Stumpf M, Junge K, Rosch R, et al. Suture-free small bowel anastomoses using collagen fleece covered with fibrin glue in pigs. J Invest Surg 2009;22(2):138-147.
[12] Hardy KJ. A view of the development of intestinal suture. Part II. Principles and techniques. Aust N Z J Surg 1990;60(5):377-384.
[13] Pillai CKS, Sharma CP. Review Paper: Absorbable Polymeric Surgical Sutures: Chemistry, Production, Properties, Biodegradability, and Performance. J Biomater Appl 2010;25(4):291-366.
[14] Zhao YP. The development history, status quo and prospects of sutures in general surgery. Chin J Pract Surg 2008;28(10):789-792.
[15] Pascual I, de Miguel GF, Gómez-Pinedo U, et al. Adipose-derived mesenchymal stem cells in biosutures do not improve healing of experimental colonic anastomoses. Br J Surg 2008;95(9):1180-1184.
[16] Omotosho P, Yurcisin B, Ceppa E, et al. In vivo assessment of an absorbable and nonabsorbable knotless barbed suture for laparoscopic single-layer enterotomy closure: a clinical and biomechanical comparison against nonbarbed suture. J Laparoendosc Adv Surg Tech A 2011;21(10):893-897.
[17] Hu Y, Duan J, Yang X, et al. Wettability and biological responses of titanium surface's biomimetic hexagonal microstructure. J Biomater Appl 2023;37(6):1112-1123.
[18] Wang X, Zhang L, Zhang X, et al. Mg–6Zn alloys promote the healing of intestinal anastomosis via TGF-β/Smad signaling pathway in regulation of collagen metabolism as compared with titanium alloys. J Biomater Appl 2022;36(9):1540-1549.
[19] Zheng YF, Gu XN, Witte F. Biodegradable metals. Mater Sci Eng: R: Rep 2014;77:1-34.
[20] Qu S, Xia J, Yan J, et al. In vivo and in vitro assessment of the biocompatibility and degradation of high-purity Mg anastomotic staples. J Biomater Appl 2017;31(8):1203-1214.
[21] Xu B, Song Y, Yang K, et al. Magnesium metal and its corrosion products: Promising materials for tumor interventional therapy. J Magnesium Alloys 2023;11(3):763-775.
[22] Gao Y, Wang L, Li L, et al. Effect of stress on corrosion of high-purity magnesium in vitro and in vivo. Acta Biomater 2019;83:477-486.
[23] Guo H, Hu J, Shen Z, et al. In vitro and in vivo studies of biodegradable Zn-Li-Mn alloy staples designed for gastrointestinal anastomosis. Acta Biomater 2021;121:713-723.
[24] Anikeev SG, Kaftaranova MI, Hodorenko VN, et al. TiNi-based material with shape-memory effect for surgical treatment of diseases of small intestine in newborn and young children. J Funct Biomater 2023;14(3):155.
[25] Neutzling CB, Lustosa SA, Proenca IM, et al. Stapled versus handsewn methods for colorectal anastomosis surgery. Cochrane Database Syst Rev 2012;(2):CD003144.
[26] Xu QR, Wang KN, Wang WP, et al. Linear stapled esophagogastrostomy is more effective than hand-sewn or circular stapler in prevention of anastomotic stricture: a comparative clinical study. J Gastrointest Surg 2011;15(6):915-921.
[27] Choy PYG, Bissett IP, Docherty JG, et al. Stapled versus handsewn methods for ileocolic anastomoses. Cochrane Database Syst Rev 2011;(9):CD004320.
[28] Ore AS, Althoff A, Kull DR, et al. Comparative early histologic healing quality of magnetic versus stapled small bowel anastomosis. Surgery 2023;173(4):1060-1065.
[29] Ho YH, Ashour MA. Techniques for colorectal anastomosis. World J Gastroenterol 2010;16(13):1610-1621.
[30] Murphy J. An analysis of the cases operated upon with the Murphy Button up to date. Lancet 1895;145:1040-1047.
[31] Wang JL, Xu JK, Hopkins C, et al. Biodegradable Magnesium-Based Implants in Orthopedics-A General Review and Perspectives. Adv Sci (Weinh) 2020;7(8):1902443.
[32] Jansen A, Brummelkamp W, Davies G, et al. Clinical applications of magnetic rings in colorectal anastomosis. Surg Gynecol Obstet 1981;153(4):537-545.
[33] Jamshidi R, Stephenson JT, Clay JG, et al. Magnamosis: magnetic compression anastomosis with comparison to suture and staple techniques. J Pediatr Surg

2009;44(1):222-228.
[34] Kanshin N, Lytkin M, Knysh V, et al. First experience with application of compression anastomoses with the apparatus AKA-2 in operations on the large intestine. Vestn Khir Im I I Grek 1984;132(1):52-57.
[35] Li XX, Cai SJ, Gao J, et al. A prospective study of the application of nickel-titanium memory alloy compression anastomosis ring to intestinal reconstruction after colorectal surgery. Chin J Gastrointest Surg 2011;14(5):330-332.
[36] Bae KB, Kim SH, Jung SJ, et al. Cyanoacrylate for colonic anastomosis; is it safe? Int J Colorectal Dis 2010;25(5):601-606.
[37] Nordentoft T, Rømer J, Sørensen M. Sealing of gastrointestinal anastomoses with a fibrin glue-coated collagen patch: a safety study. J Invest Surg 2007;20(6):363-369.
[38] Alam Z, Mohan M, Pal K, et al. Albumin-PEG-based biomaterial for laser-tissue soldering and its real-time monitoring with swept-source optical coherence tomography. Lasers Surg Med 2021;53(6):815-829.
[39] YAHR WZ, STRULLY KJ, HURWITT ES. Non-occlusive small arterial anastomosis with a neodymium laser. Surg Forum 1964;15:224-226.
[40] Cochrane J, Beacon J, Creasey G, et al. Wound healing after laser surgery: an experimental study. Br J Surg 1980;67(10):740-743.
[41] Yamada E, Sumiyoshi H, Yamaga Y, et al. Bowel welding technique in dogs and cats using a diode laser: an experimental study. J Vet Med Sci 2006;68(7):669-674.
[42] Simhon D, Halpern M, Brosh T, et al. Immediate tight sealing of skin incisions using an innovative temperature-controlled laser soldering device: in vivo study in porcine skin. Ann Surg 2007;245(2):206-213.
[43] Huang H-C, Walker CR, Nanda A, et al. Laser welding of ruptured intestinal tissue using plasmonic polypeptide nanocomposite solders. ACS Nano 2013;7(4):2988-2998.
[44] Wang Y, Liu K, Xiang X, et al. The impedance analysis of small intestine fusion by pulse source. Open Life Sci 2020;15(1):808-818.
[45] Zhao L, Zhou Y, Song C, et al. Predicting burst pressure of radiofrequency-induced colorectal anastomosis by bio-impedance measurement. Physiol Meas 2017;38(3):489-500.
[46] Gentile M, Cestaro G, Velotti N, et al. Lateral internal sphincterotomy (LIS) for chronic anal fissure by LigaSure™ Small Jaws: a comparison with traditional technique. Chirurgia 2022;35(4):213-217.
[47] Dunay MP, Lipcsey Z, Arany-Tóth A, et al. Experimental assessment of three electrosurgical tissue-sealing devices in a porcine model. Acta Vet Hung 2020;68(3):318-322.
[48] Tu L, Zhou Y, Song C, et al. Preliminary study of a control algorithm for radio-frequency-induced intestinal tissue fusion. Int J Hyperthermia 2019;36(1):1296-1305.
[49] Pan H, Leung KK, Ng EKW. Tissue fusion technology versus suture and staple in porcine bowel anastomosis: An in vivo study. Braz J Med Biol Res 2020;53(5):e9305.
[50] Lacitignola L, Imperante A, Trisciuzzi R, et al. Swine small intestine sealing performed by different vessel sealing devices: Ex-vivo test. Vet Sci 2021;8(2):34.
[51] Abbe R. Sarcoma of the kidney; its operative treatment. Ann Surg 1894;19:57-69.
[52] Lee S, Wong L, Orloff MJ, et al. A review of vascular anastomosis with mechanical aids and nonsuture techniques. HNS 1980;3:58-65.
[53] Peng SY, Wang JW, Hong DF, et al. Binding pancreaticoenteric anastomosis: from binding pancreaticojejunostomy to binding pancreaticogastrostomy. Updates Surg 2011;63(2):69-74.
[54] Peng SY, Wang JW, Lau WY, et al. Conventional Versus Binding Pancreaticojejunostomy After Pancreaticoduodenectomy. Ann Surg 2007;245(5):692-698.
[55] Peng S. Binding pancreaticojejunostomy: 150 consecutive cases without leakage. J Gastrointest Surg 2003;7(7):898-900.
[56] Wang Y, Cai X, Jin R, et al. Experimental Study of Primary Repair of Colonic Leakage with a Degradable Stent in a Porcine Model. J Gastrointest Surg 2011;15(11):1995-2000.
[57] Wang Y, Cai X, Cai H, et al. Experimental study of colonic anastomosis with a degradable stent in a porcine model. Am J Surg 2010;199(6):833-839.